Université de Lille, Unité de Mécanique de Lille-J. Boussinesq (UML)EA 7512 , F-59000 Lille France

PHD THESIS

Defended by

Himani Garg

Particle laden inhomogeneous elastic turbulence

A thesis submitted in fulfillment of the requirements

for the degree of **Doctor of Philosophy**

in Mechanical Engineering

University of Lille

Defended on Friday, February 15, 2019

Jury :

Reviewers :	Sergio CHIBBARO	University Pierre and Marie Curie
	Teodor BURGHELEA	University of Nantes, LTN
Examinators:	Alexandre DELACHE	University of Jean Monnet Saint-Etienne
	Angela Ourivio NIECKELE	Pontifical Catholic University of Rio de Janeiro
President of the Jury:	Thomas GOMEZ	University of Lille, LMFL
Director :	Gilmar MOMPEAN	University of Lille, UML
Co-advisor :	Enrico CALZAVARINI	University of Lille, UML
	Stefano BERTI	University of Lille, UML

Declaration of Authorship

I, Himani GARG, declare that this thesis titled, "Particle laden inhomogeneous elastic turbulence" and the work presented in it are my own. I confirm that:

- This work was done wholly or mainly while in candidature for a research degree at this University.
- Where any part of this thesis has previously been submitted for a degree or any other qualification at this University or any other institution, this has been clearly stated.
- Where I have consulted the published work of others, this is always clearly attributed.
- Where I have quoted from the work of others, the source is always given. With the exception of such quotations, this thesis is entirely my own work.
- I have acknowledged all main sources of help.
- Where the thesis is based on work done by myself jointly with others, I have made clear exactly what was done by others and what I have contributed myself.

Signed:

Date:

Abstract

The turbulent state of a flow is commonly associated with a dynamical condition where the viscous forces have a negligible role compared to the nonlinear inertial forces that are at work on the system (large Reynolds numbers). However, due to the concurrent effect of elastic forces, dilute suspension of polymers can exhibit erratic fluctuations of their flow even in the case where the viscous forces dominate the inertial ones (i.e. vanishing Reynolds number). Such a flow state, first detected in a series of experiments by Groisman and Steinberg around 2000, has been called, by analogy, elastic turbulence. Elastic turbulence can be generated in small-scale laboratory settings and has appeared from the very beginning as being relevant to enhancing the mixing efficiency in microfluidic devices.

Turbulent-like fluctuations have indeed the effect of increasing the diffusivity, e.g. of a dye or a of chemical substance, from its molecular value to an effective value that can be several orders of magnitude larger. However, when the mixing components are much larger than the molecular scale, they are not simply passively transported (advected) by the flow, and a quantification of the quality of the mixing process is a daunting task. This applies in particular to the situation where the suspension also contains impurities with non-zero size, such as dust, or other solid impurities, or in general any micro-particle whose inertia can not be considered as negligible. Due to their non-vanishing inertia, such particles have a tendency to unmix even when advected by a vigorously fluctuating and unpredictable flow. Furthermore, particles in such a condition are not suitably modelled in terms of fields, and one can not avoid adopting an individual or Lagrangian point of view.

The Lagrangian studies of the dynamics of so-called inertial particles, such as dust, drops and bubbles transported by flows, has undergone major developments in recent years. By means of experimental, numerical and theoretical research, it has been possible to characterize and model the phenomenon of particle accumulations, or segregation if different types of particles are considered. This has been performed particularly in turbulent flows at high Reynolds numbers. However, the dynamics of particles in elastic turbulent flows is still relatively unexplored. The present thesis aims at filling this gap by investigating the aggregation properties of material particles that are heavier than the carrying fluid, in visco-elastic fluids in elastic turbulence conditions.

With this aim we carry out extensive direct numerical simulations of a di-

lute polymer solution, described by the Oldroyd-B rheological model, in a two-dimensional Kolmogorov flow setting seeded with point-like inertial particles. Our analysis focusses both on the small- and large-scale features of the resulting inhomogeneous particle distribution and on its connections with the underlying flow structures.
The analysis reveals that particles cluster preferentially in regions of instantaneously maximally stretched polymers and highly strained flow field. The intensity of such a phenomenon depends on the interplay between the inertia of the particles and the typical time scale associated with the elastic turbulent flow, which is parametrized by the Stokes number, and is maximal for intermediate values of the inertia of the particles. In particular, it is shown that the preferential concentration of inertial particle suspensions in such turbulent-like flows follow from the dissipative nature of their dynamics. We provide a quantitative characterization of the dimensionality of thin filamentary particle clusters by using fractal dimension indicators.
The non-homogeneity of the turbulent flow along the direction orthogonal to the direction of the forcing has a marked effect on the average particle distribution. Particles appear to experience the so-called turbophoretic forcing, an overall migration from regions of large turbulent fluctuations to regions of small turbulent fluctuations. Indeed, we show that the mean particle concentration profiles are peaked in the regions of the lowest turbulent eddy diffusivity. This large-scale inhomogeneity of the particle distribution profiles can be interpreted in the framework of a mean-field model derived in the limit of small, but non-zero, particle inertia. The main characteristics of different observables, notably the root-mean-squared deviation of the particle distribution relative to the uniform one, are, to a good extent, independent of the flow elasticity.

Keywords: Direct numerical simulations, Elastic turbulence, Inertial particles, Lagrangian dynamics

Résumé

Les expériences de laboratoire montrent que, même dans des solutions très diluées, l'interaction des polymères avec des écoulements fluides peut modifier considérablement les propriétés des écoulements turbulents ou, si l'écoulement est laminaire, peut déclencher un nouveau type de mouvement irrégulier appelé "turbulence élastique". Les écoulements dans un tel régime dynamique sont prometteurs pour améliorer l'efficacité du mélange dans les applications microfluidiques, qui impliquent souvent la présence d'impuretés de taille finie en suspension, telles que des particules solides petites et lourdes. La compréhension de la dispersion des particules dans les écoulements à grand nombre de Reynolds des fluides newtoniens et non newtoniens a déjà été abordée dans des études antérieures, qui ont mis en évidence des effets à la fois à grande et à petite échelle et est un sujet d'intérêt è la fois fondamental et pour des applications environnementales ou industrielles par exemple. Cependant, la dynamique des particules dans les écoulements élastiques et turbulents reste encore peu explorée.
L'étude ici vise à étudier les propriétés d'agrégation de particules matérielles ponctuelles (plus lourdes que le fluide porteur) dans les fluides viscoélastiques dans des conditions de turbulence élastique (c'est-à-dire dans le cas de faible inertie du fluide et de grande élasticité). Nous effectuons des simulations numériques directes bi-dimensionelles d'écoulements périodiques avec cisaillement moyen de Kolmogorov avec des solutions de polymères dilués décrites par le modèle Oldroyd-B. Les caractéristiques à petite et grande échelle de la distribution résultante inhomogène de particules sont examinées, en se concentrant sur leur connexion avec la structure sous-jacente de l'écoulement . Notre analyse révèle que les particules sont préférentiellement regroupées dans des régions où les polymères sont instantanément maximalement étirés. L'intensité d'un tel phénomène dépend de l'interaction paramétrée par le nombre de Stokes, entre l'inertie des particules et l'échelle de temps typique associée à l'écoulement de turbulence élastique, et est la plus grande pour des valeurs intermédiaires d'inertie de particules.

En particulier, il est montré que la concentration préférentielle de suspensions de particules inertielles dans de tels écoulements ressemblant à la turbulence découle de la nature dissipative de leurs dynamiques. Nous établissons une caractérisation quantitative de ce phénomène (utilisant la corrélation et la dimension de Kaplan-Yorke) qui permet de le relier á l'accumulation de particules dans des régions de l'écoulement

filamenteuses fortement déformées produisant des grappes de dimension fractale faiblement supérieure à 1.

Á plus grande échelle, les particules subissent une ségrégation de type turbophorétique dans la direction non-homogéne de l'écoulement. En effet, nos résultats indiquent que la distribution des particules est fortement liée aux structures moyennes de l'écoulement de type turbulent. En raison de la turbophorèse, les profils de densité moyenne atteignent leur maximum dans les régions où la diffusivité turbulente est la plus faible. L'inhomogénéité á grande échelle de la distribution des particules est interprétée dans le cadre d'un modèle dérivé dans la limite d'inertie des particules, petite mais finie. Les caractéristiques qualitatives de différents observables (telles que L'écart quadratique moyen de la distribution des particules par rapport à la distribution uniforme) sont, dans une large mesure, indépendantes de l'élasticité du l'écoulement. Quand celle-ci est augmentée, on constate cependant que cette dernière diminue légèrement le degré global moyen de mélange turbophorétique.

Mots clés: Simulations numériques directes, Turbulence élastique, Particules inertielles, Dynamique lagrangienne

Acknowledgements

Undertaking this PhD has been a truly life-changing experience for me and it would not have been possible to do without the support and guidance that I received from many people.

Firstly, I would like to express my sincere gratitude to my advisor *Stefano Berti* for his continuous support, patience, motivation, constant encouragement, expert suggestions and immense knowledge during my Ph.D. His guidance helped me in all the time of research and writing of this thesis. Stefano has been supportive and has given me the freedom to pursue various projects without objection. I could not have imagined having a better advisor and mentor for my Ph.D study.

I wish to express my sincere thanks to *Enrico Calzavarini* for supervising me and his kind support in all the moments. His deep insight has been invaluable to me and my work. This PhD study would not have been possible without his cooperation, support, and patience during the numerous group discussions. At many stages in the course of this research project, I benefited from his advice, particularly so when exploring new ideas. His positive outlook and confidence in my research inspired me and gave me confidence. Enrico is someone you will instantly love and never forget once you meet him. He's the funniest advisor and one of the smartest people I know. I hope that I could be lively, enthusiastic, and energetic as Enrico and to someday I am able to command the audience, as he does.

I also thank my director *Gilmar Mompean* for his helpful career advice and suggestions in general.

Besides my advisor, I would like to thank the reviewers of my thesis Prof. Teodor Burghelea and Prof. Sergio Chibbaro for their insightful comments and encouragements.

I thank my fellow lab mates *Dario Oliveira Canossi, Babak Rabbanipour, Kalyan Shrestha* and *Hamidreza Ardeshiri* for the stimulating discussions, for the sleepless nights we worked together before deadlines, and for all the fun we have had in the last three years. In particular, I am grateful to *Babak Rabbanipour* for all the support, encouragement and constant feedback he gave me during the months I spent undertaking my research work.

Also, I thank to my friends *Tonny, Raj Krishna Paul, Inderjeet Singh, Ismail Bensekrane*. I'll never forget the wonderful lunches, coffee breaks, fun activities and travels, we have done together.

It's my fortune to gratefully acknowledge the support of some special individuals. Words fail me to express my appreciation to *Pankaj Chopra,*

Vivek Sharma, Gopal Krishna Dila, Alice, Blaze, Abhilash Saini, Sreyashee Jena, and *Abhijeet Das* for their support, generous care and the homely feeling during my rough times.

I am much indebted to *Pankaj Chopra* and *Vivek Sharma*, both of them were always beside me during the happy and hard moments to push me and motivate me. I can see the good shape of my thesis as well as of my carrier because of their help and suggestions. A journey is easier when you travel together. Interdependence is certainly more valuable than independence. Thanks doesn't seem sufficient but it is said with appreciation and respect to them for their support, encouragement, care, understanding and precious friendship.

I would also like to say a heartfelt thank you to my *Maa* and *Papaji* for always believing in me and encouraging me to follow my dreams. And for helping in whatever way they could during this challenging period. And finally to my brother *Arpan*, who has been by my side throughout this PhD, living every single minute of it, and without whom, I would not have had the courage to embark on this journey in the first place. I was continually amazed by the patience of my mother, father and brother who experienced all of the ups and downs of my research. I am indebted to them for their unconditional love, sacrifice and moral support.

I dedicate this thesis to my parents and my brother for their constant support and unconditional love. I love you all dearly.

Contents

A guide to this thesis

Mixing processes aim at generating homogeneous solutions of multiple material components in natural and engineering flows [1–4]. Such processes are widely applied in microfluidic devices for heat and mass transfer [5–8], mixing in a porous medium [9, 10], and numerous relevant research areas. Efficient mixing is often desired in lab-on-a-chip platforms for complex chemical reactions, and mixing and transfers of small volumes at pore scales [11].

Chaotic and turbulent flow instabilities are recognized to be effective mechanisms for mixing and have been well studied for Newtonian fluids [12, 13]. However, due to the small scales, such flows are difficult to achieve in microfluidic systems. The realization of turbulent flow in microchannels is a lot more complicated and challenging than in large ducts, wherein the driving pressure critically limits the flow rate. Flows of a Newtonian fluid in microchannels are consequently limited to the laminar flow regime and difficult to mix [14, 15]. At low flow rates, where flows are often in a laminar, low Reynolds number regime, mixing must rely on molecular diffusion between the different fluid layers, the thicknesses of which are much larger than the characteristic diffusion length. As well, chaotic advection needs external actuators and complex channel structures [16]. Both ideas lead to complex and costly fabrication processes. The lack of mixing is then often a key obstacle to achieving good performance in microfluidic applications. Thus, instead of relying on inertial effects, other strategies to induce mixing, such as introducing an elastic effect into a micro-scale laminar flow, may enhance the mixing effect [17, 18].

Over the last few decades, it has been recognized that a solution with a minute amount of deformable polymers, i.e. a viscoelastic fluid, can result in elastic flow instability [18–24]. Viscoelastic fluids are known to be characterized by non-Newtonian behaviour under appropriate conditions. In particular, dilute polymer solutions may display non-negligible elastic forces when the suspended polymeric chains are sufficiently stretched by fluid velocity gradients. Interestingly, a polymer with a sufficiently long relaxation time or a high Weissenberg number can give rise to an irregular flow state with velocity fluctuations spanning a broad range of spatial and temporal scales even at low Reynolds numbers (absence of fluid inertia). This irregular flow state at high Wi and low Re is known as elastic turbulence [21] and is caused by an instability due to the polymer stresses. Elastic

turbulence has been experimentally observed in different flow configurations [21, 22, 25–28]. On the basis of its similarity with turbulent fluid motion, elastic turbulence has been proposed as an efficient system to enhance mixing in low Reynolds number flows [22]. Moreover, it has been shown that it can increase heat transfer [6, 7] and promote emulsification [29]. Recently, the potential use of elastic turbulence in the oil industry has emerged as a very promising application. Dilute polymer solutions are indeed used to recover the oil that remains trapped inside the pores of reservoir rocks after an initial water flooding, and elastic turbulence has been proposed as a mechanism to explain the unexpectedly high efficiency of this oil recovery method [30].

Understanding transport phenomena at small scales is of importance and wide interest principally for two reasons: first, the particle dynamics relevant for the biological and chemical processes that take place at these scales; second, microfluidic devices are playing a very important role in research and industrial technologies, typically together with complex fluids and flows whose dynamics still lack a detailed description. Transport and mixing processes in fluids, however, often involve the presence of suspended impurities, such as small and heavy solid particles. To achieve a fundamental understanding of the mixing and transport phenomena in elastic turbulence flows, it then seems necessary to accurately characterize how the inertia of the particles affects the concentration of the transported species. Indeed, it is known that in turbulent flows the difference between the mass density of the impurities and that of the carrier fluid typically induces unmixing effects. To be specific, it produces non-homogeneous particle distributions at small scales, as well as at large ones when turbulence spatial inhomogeneities are present (as, e.g. in a duct or in a boundary-layer flow). Although both types of inhomogeneities can be simultaneously present, they correspond to essentially different phenomena. While at small scales they give rise to complex clustered distributions due to the combined effect of small-scale turbulence and particle inertia [31], at large scales they manifest themselves in the accumulation of particles in regions of minimal turbulent intensity, whose locations are closely related to the structure of the mean flow (turbophoresis) [32–35].

The dynamics of particles suspended in random or turbulent flows has been intensively studied for several decades. In recent years, substantial progress in understanding the dynamics of inertial particles has been achieved in turbulent flows of both Newtonian (see, e.g. [31, 36–38]) and non-Newtonian (e.g. in [39, 40]) fluids. The phenomenon of spatial cluster-

ing of independent point particles subject to Stokes drag in turbulent flows (where the fluid flow is smooth) is now well understood by means of numerical simulations as well as theoretical approaches [41, 42]. Despite the potential of elastic turbulence for mixing in microfluidics, the dynamics of particles in this regime are still quite unexplored, see [43]. The present thesis presents the results of an investigation of heavy inertial particle transport at low Reynolds numbers in a non-homogeneous flow of elastic turbulence in two dimensions.

The main subject of this thesis is to study and provide a detailed description of the statistical properties of passive inertial particles heavier than the carrying fluid in two-dimensional inhomogeneous elastic turbulent fluids by means of numerical and analytical tools, and to relate them to the behaviour of the main observables associated with the dynamics of the flow fields. This thesis is organized in 6 chapters.
The first chapter is dedicated to an introduction to viscoelastic fluids. After a brief description of polymers and their structural properties, their behaviour in a flow is considered. We introduce the models needed to describe the main features of the viscoelastic fluids starting from the dumbbell model and from this we construct hydrodynamic models such as Oldroyd-B model and the FENE-P model.
The second chapter is a review of the theoretical basis of the models used to describe the motion of inertial particles. An overview of several ways of quantifying the preferential concentration of particles, such as the correlation dimension and the Kaplan–Yorke dimension, is presented.
The third chapter deals with the phenomenon of elastic turbulence. Direct numerical simulations of the two-dimensional Oldroyd-B model are performed, at low Reynolds numbers and high Weissenberg numbers to develop elastic turbulence. The results of the numerical study of two-dimensional dilute polymer solutions are presented.
The fourth chapter presents a numerical and statistical analysis of heavy inertial particle clustering in an elastic turbulent fluid, to describe the aggregation properties of particle spatial distributions. We present the properties of the particle spatial distributions in relation with the main features of the flow fields, separately focusing on preferential concentration effects, measurements of Lyapunov exponents, small-scale fractal clustering, and segregation distance.
In the fifth chapter, a detailed numerical and theoretical investigation of tubophoresis in elastic turbulent flow is presented. We observed that large-scale inhomogeneities can be revealed in the form of regions of low particle

concentration. The differences between this mechanism, causing inhomogeneity at large scales, and the small-scale clustering are presented.
Lastly, in the sixth chapter, we will discuss the conclusions of this research and perspectives on how it can be further continued.

Chapter 1

Visco-elastic fluids and elastic turbulence

Contents

1.1 Polymer solutions

Polymers are molecules of high molecular mass, structurally composed of repeated units derived from molecules of relatively low molecular mass. There are both natural and synthetic polymers: among the naturally occurring polymers are DNA, proteins, starches, cellulose, and latex. Synthetic polymers are produced commercially on a very large scale and have a wide range of properties and applications. For example, the materials commonly called plastics are all synthetic polymers.

Polymers are formed by chemical reactions where the repeating units, called monomers, are joined sequentially, creating a chain. In many polymers, only one type of monomer is used. In others, two or three different monomers may be combined [44,45].

A large number of experiments have been performed in the past decades to exploit the accessibility of the microscopic properties of these macromolecules (including very important biomolecules such as DNA). As a

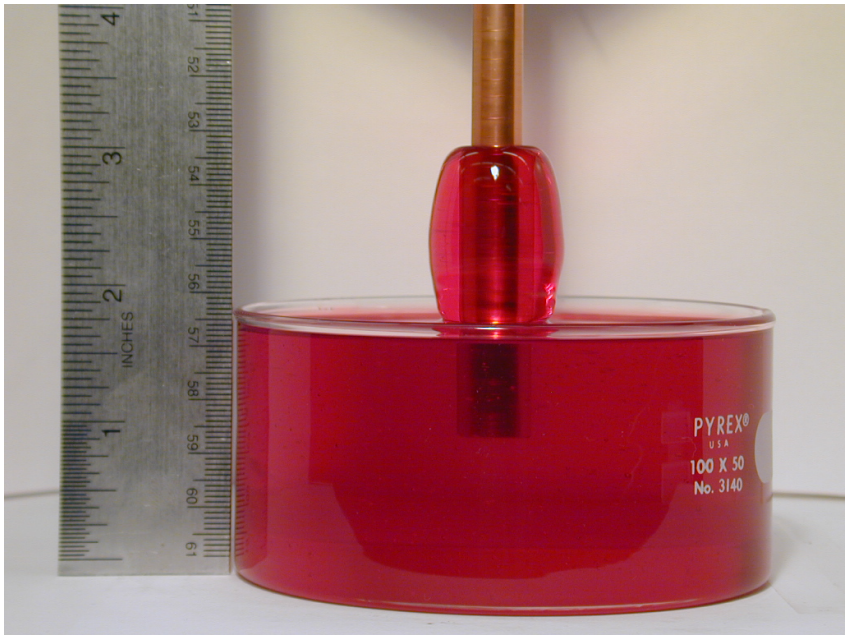

Figure 1.1: Example of the Weissenberg effect with fluid climbing the rotating rod (picture from web.mit.edu).

result, many of the theoretical polymer models proposed in the past 60 years have been verified and refined. Phenomenological models predicting the elasticity of macromolecules have been confirmed by many experiments [46]. Furthermore, much effort has been devoted to the detailed analysis of the motion of macromolecules in fluid flows [47].

Since the end of the 1940s it has been known that the addition of polymer additives to a fluid can drastically change its properties, and thus much effort has been devoted to the detailed analysis of the motion of macromolecules in fluid flows and to the rheological behaviour of the solution. Due to their molecular structure, polymers have elastic degrees of freedom which must be taken into account in the description of the mechanical response of the fluid to which they are added. Indeed, while for an ideal Newtonian fluid the stress is proportional to the deformation rate, the constant of proportionality being the viscosity, in an elastic material, the stress is proportional to the deformation itself, the constant of proportionality being the Hooke modulus. A solution of polymers in a Newtonian fluid can be thought of as a mixture of these idealized situations, because it presents characteristics of both viscous and elastic materials, and it is thus called a visco-elastic fluid.

This structural difference in the dependence of the stress on the deforma-

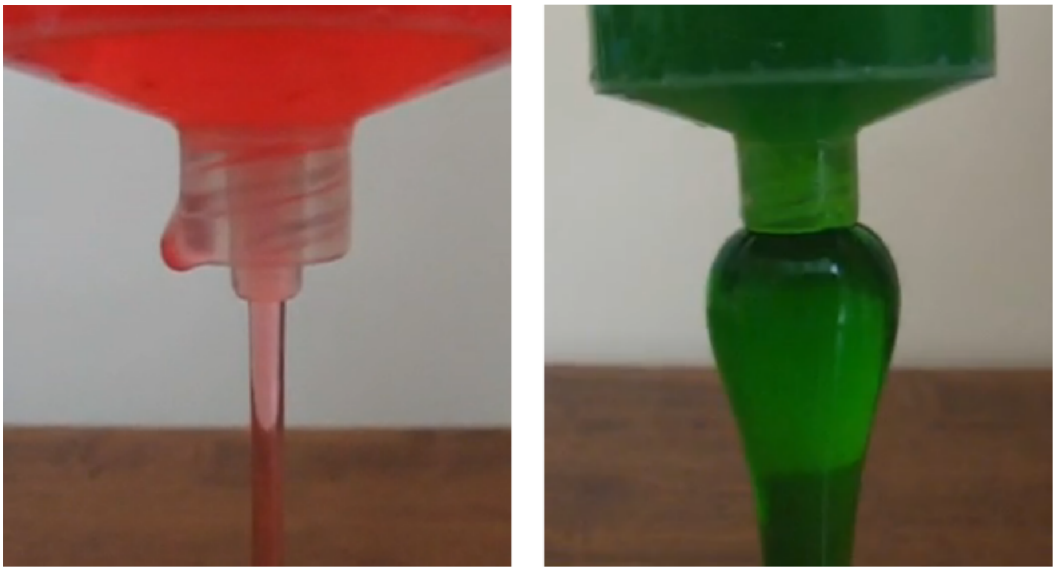

(a) (b)

Figure 1.2: (a) A Newtonian fluid is slowly extruded from a syringe. (b) The polymer solution which has been dyed green is slowly extruded from a syringe. On exiting, a noticeable swelling in the polymer solution stream several times larger than the diameter of the orifice is observed. Such a phenomenon is referred to as the Barus effect (Die swell) linked to non-zero normal stresses [48]. On the other hand, a Newtonian fluid does not exhibit the Barus effect.

tion properties is the source of the distinctive behaviour of visco-elastic and Newtonian fluids. Among the large number of notable phenomena which are known to appear when dealing with visco-elastic fluids there is the rod-climbing (or Weissenberg) effect, the very large extrudate swelling at the exit of a die (as shown in Fig. 1.2), and many others (entanglement and turbulent drag reduction).

Let us briefly consider the Weissenberg effect, also known as the rod-climbing effect [49] and the die swell effect [48].

Weissenberg effect: When a Newtonian fluid is placed in rotation, it is pushed away from the centre by the centrifugal force, and a dip appears on the free surface, which takes the shape of a paraboloid. In contrast, visco-elastic fluids tend to climb the rod [49]. Rod climbing is exhibited by liquids that show a normal stress difference (as shown in Fig. 1.1). In Newtonian liquids, the normal stresses (pressure) are isotropic even in flow, whereas

polymeric liquids, upon the application of a shear flow, begin to develop normal stress differences between the flow and flow-gradient directions.

Die swell effect: Analysing the motion of a fluid coming out from a capillary, a big difference can be observed between a Newtonian fluid and a visco-elastic fluid, as shown in Fig. 1.2. When a visco-elastic fluid flows out of a die, the diameter of the extrudate is usually greater than the size of the orifice. This is called die swell, extrudate swell, or the Barus effect [48] (as shown in Fig. 1.2). The degree of extrudate swell is generally of a difference between the diameter of the extrudate and the diameter of the die. For a fully developed flow of a visco-elastic fluid in a tube, there is tension along the streamlines. When the fluid exits the tube, it relaxes the tension along the streamlines by contracting in a longitudinal direction. For an incompressible liquid, this results in a lateral expansion, giving rise to the die-swell phenomenon.

The effects produced by adding a polymer to a Newtonian fluid cover a wide range: they can modify the transport of heat, mass and momentum, influence the formation or depletion of vortices, and can change the stability of laminar motion and the transition to turbulence. A visco-elastic fluid can show a very interesting behaviour from a practical point of view, and a number of papers have been devoted to the understanding of the behaviour of visco-elastic fluids (see the references in [50]). The addition of a small amount of long-chain polymers to a Newtonian fluid flowing in a pipe can produce a dramatic reduction of the skin friction between the walls of the pipe and the fluid [51]. Drag reduction by polymer additives has been studied for more than half a century [52–54].

In this chapter, I will introduce the basics of polymer dynamics in fluids. Starting from a microscopic description in terms of the dynamics of a single polymer, the simple hydrodynamic models which have been typically used to describe visco-elastic solutions will be constructed. Further, I will briefly review the emergence of elasticity-driven turbulent-like states at small Reynolds numbers, which has been called *elastic turbulence*.

1.2 The Weissenberg number

Since the end of the 1940s, it has been known that gradients of a velocity field can affect polymers and strongly deform them in fluid flow. A polymer in a fluid at rest typically resembles a spongy ball of size R_0, i.e. it

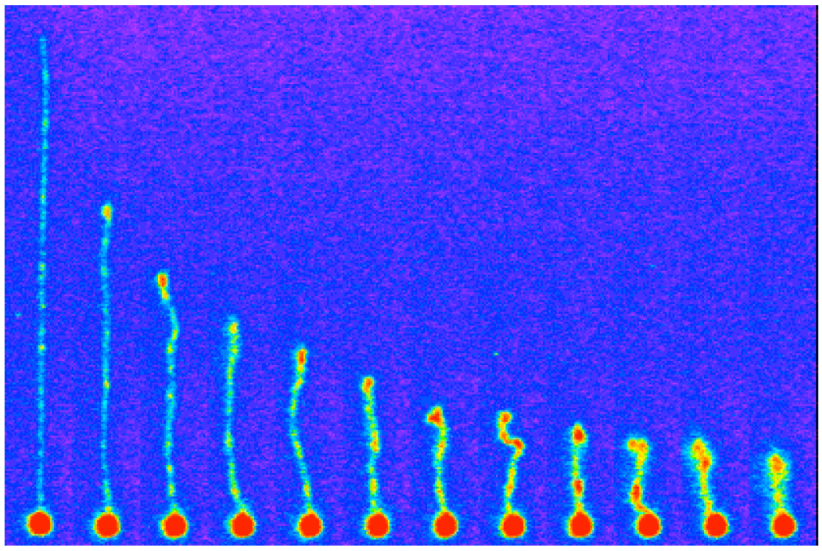

Figure 1.3: Snapshots of single DNA molecule relaxing to a coiled state. In this experiment, a latex bead is tethered to an end of the molecule. The DNA molecule, coloured with a fluorescent dye, is stretched by a uniform flow and once the DNA molecule is fully elongated, the flow is turned off and the relaxation of the molecule is measured at different times [55].

is in a coiled configuration. In principle, all the configurations are permitted (even the fully stretched one) but in probabilistic terms, highly coiled configurations are much more probable. In contrast, when strong velocity gradients are imposed across a polymer, highly stretched states occur with large probabilities.

The entropic tendency to return to a coiled state is indicated by an intrinsic parameter of the polymer, which is the time required by the molecule to reach the steady state in the absence of flow, starting from a non-coiled configuration. Polymer relaxation can be characterized by various measures of the relaxation time. Zimms's time (relaxation time) is the largest of these. It depends on the temperature and viscosity of the solvent, on the number of monomers in the molecule, and on the effective length of the bonds between the monomers. The deformation of the polymer molecule is the result of the competition between the stretching exerted by the gradients of the velocity, and the relaxation of the polymer to its equilibrium configuration. Experiments with DNA molecules [55] have shown that this relaxation is linear, provided that the elongation is small compared to the maximum extension, i.e. $R \ll R_{max}$ (see Fig. 1.3).

Clearly the stretching rate of a given velocity field must be compared to the relaxation time of the molecule. If the velocity gradients are weak, then the restoring force predominates and the polymer molecule is not stretched. In contrast, if the stretching rates are very high the polymer molecules will be stretched. One should note that at least dimensionally, velocity gradients correspond to stretching rates.

The whole concept of the relative strength of stretching with respect to relaxation can be quantified in terms of the non-dimensional *Weissenberg number*, named after the German physicist Karl Weissenberg:

$$Wi = \frac{\tau}{\tau_f} \tag{1.1}$$

where τ_f stands for the typical time scale of the flow and τ is the largest relaxation time [56]:

$$\tau = \frac{\mu R_0^3}{k_B T} \tag{1.2}$$

where k_B is Boltzmann's constant, T is the temperature, and μ is the dynamic viscosity of the solvent.

When $Wi \ll 1$, the relaxation is fast, and thus a polymer stays in its coiled configuration. But $Wi \gg 1$ corresponds to an entirely stretching-dominated dynamics, and thus the polymers are substantially elongated.

What happens for $Wi \approx 1$, i.e. when the relaxation and the stretching are competing with each other, is a natural question. Hinch and De Gennes were the first to address this question [57,58], claiming that there is a sharp transition between stretching-dominated and relaxation-dominated states in strong flows, known as the *coil stretch transition*. A typical example cited by De Gennes where the transition is expected in the time-independent elongational flow. Chu and co-workers performed one of the first experiments where single-molecule measurements of the coil–stretch transition were taken in steady shear and elongational flows [59, 60]. There is also a coil–stretch transition for random flows [47], but the transition between the coiled and stretched configurations is not as sharp as in the elongational flows, because a random flow has a fluctuating extension rate, resulting in a broader distribution of polymer elongations. Many theoretical and numerical studies have also addressed the statistical nature of the polymer dynamics in random [61–63], simple shear or laminar [64–66], and turbulent flows [67–69].

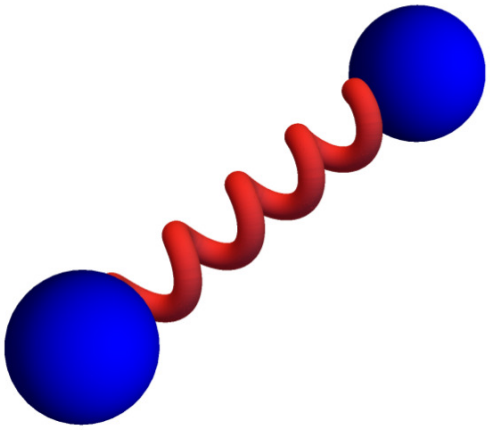

Figure 1.4: Dumbbell model

1.3 Visco-elastic models

1.3.1 The elastic dumbbell model

A simplified model to represent the polymer molecule, which is often used, is the elastic dumbbell model. The model consists of a spring with elastic constant $H = \frac{3k_BT}{2R_{max}b}$ connecting a couple of beads of length b, negligible mass, and the same radius. Here R_{max} is the maximum extension of the polymer molecule. Despite its simplicity, it can reproduce several rheological properties of dilute suspensions of polymers. The evolution of a dumbbell end-to-end separation vector $\boldsymbol{R} = \boldsymbol{x}_2 - \boldsymbol{x}_1$, where $\boldsymbol{x}_i$ is the position of the bead, is characterized by the following forces:

- the hydrodynamic drag force represents the drag experienced by the massless beads as they move through the solvent,
- the Brownian force due to thermal fluctuations,
- the elastic spring restoring force, which tends to bring the polymer molecule back to its equilibrium configuration.

Moreover, assuming that in a homogeneous flow field the velocity gradients do not change appreciably over a distance comparable to the size of a massless bead, the evolution equation for $\boldsymbol{R}$ can be written as

$$\dot{\boldsymbol{R}} = -\frac{H}{\beta}\boldsymbol{R} + B\boldsymbol{\xi} \tag{1.3}$$

where β is the friction coefficient and $\boldsymbol{\xi}$ is a zero-mean Brownian process modelling the Brownian forces with correlation $< \xi_i(t)\xi_j(t') >= \delta_{ij}\delta(t-t')$. The constant $B = \sqrt{\frac{2R_0^2}{\tau}}$ depends on the average size of a polymer molecule in its coiled state R_0 and the relaxation time of the polymer τ, where

$$\tau = \frac{\beta}{H}. \tag{1.4}$$

If we assume that the flow field is inhomogeneous, it is reasonable to expect that polymers can also be stretched because of the differing velocities of the beads. Therefore, we must add an extra term $\dot{\boldsymbol{R}} = \boldsymbol{u}(\boldsymbol{x}_2, t) - \boldsymbol{u}(\boldsymbol{x}_1, t)$ to Eq. (1.3) to take into account the stretching due to the different velocities of the two beads. Here, $\boldsymbol{u}(\boldsymbol{x}_1, t)$ and $\boldsymbol{u}(\boldsymbol{x}_2, t)$ represent the velocities of beads at position $\boldsymbol{x}_1$ and $\boldsymbol{x}_2$, respectively. Since the flow is smooth at the scale of the polymer, we can approximate this stretching term by the velocity gradient. The equation of motion of polymer can be rewritten as

$$\dot{\boldsymbol{R}} = (\boldsymbol{R}\cdot\nabla)\boldsymbol{u} - \frac{1}{\tau}\boldsymbol{R} + \sqrt{\frac{2R_0^2}{\tau}}\boldsymbol{\xi} \tag{1.5}$$

This linear description of the dumbbell model is appropriate only for small elongations in the regime $R \ll R_{max}$. The description is no longer appropriate when the elongations develop to a great extent and become of the order of R_{max}, because of the dependence of the friction coefficient β and the relaxation time τ on the elongation itself. Thus to take into account these effects, one of the possibile generalizations is to consider the Finite Extensible Non-Linear Elastic model (FENE model) [49]. This model assumes $\tau \to \tau\frac{{R_{max}}^2 - R^2}{{R_{max}}^2 - R_0^2}$. The friction coefficient β is estimated as $\beta = 6\pi\mu R_0$, which on plugging into Eq. (1.4) gives the Zimm relaxation time $\tau = \frac{\mu R_0^3}{k_B T}$ [56]. This unique characteristic time has to be seen as the largest relaxation time of the polymer dynamics. Higher oscillatory modes, with faster relaxation times, have been experimentally observed in DNA [70]. They can be only weekly excited by the gradients of the velocity in a turbulent flow. Thus in a simplified rheological model it is enough to keep only the principal mode, with the largest relaxation time.

1.3.2 Hydrodynamic models

The previous description of the polymer dynamics accounts for the behaviour of a single polymer in a fluid, but does not take into account the back reaction of the polymers on the fluid. In order to take into account this

feedback mechanism, it is necessary to move to a macroscopic hydrodynamic description. Several models have been introduced (see, e.g. [49,71]). These models describe the fluid as non-Newtonian, taking into account the back reaction of the polymers on the flow by including an extra stress term in the momentum conservation equation.

1.3.2.1 The Oldroyd-B model

A model that is often adopted, due to its simplicity, is the linear visco-elastic Oldroyd-B model, which can be derived from the elastic dumb-bell model [49]. The passage from the microscopic behaviour of a single molecule to a macroscopic description requires getting rid of the micro-scopic degrees of freedom, such as the thermal noise. The macroscopic dynamics of the polymer is conveniently described in terms of the *conformation tensor*

$$\sigma_{ij} = \frac{\langle R_i R_j \rangle}{R_0^2} \tag{1.6}$$

where the average is taken over the thermal noise or, equivalently, over a small volume containing a large number of molecules. By definition, the conformation tensor $\boldsymbol{\sigma}$ is symmetric positive definite, and its trace $tr\,(\boldsymbol{\sigma})$ is a measure of the elongation of the molecules of the polymer.

The evolution equation for the conformation tensor $\boldsymbol{\sigma}$ can be derived from Eq. (1.5) (see Bird *et al.* 1987 [49]):

$$\partial_t \boldsymbol{\sigma} + (\boldsymbol{u}\cdot\boldsymbol{\nabla})\boldsymbol{\sigma} = (\boldsymbol{\nabla}\boldsymbol{u})^T\cdot\boldsymbol{\sigma} + \boldsymbol{\sigma}\cdot(\boldsymbol{\nabla}\boldsymbol{u}) - 2\frac{\boldsymbol{\sigma}-\mathbf{1}}{\tau}. \tag{1.7}$$

where τ is the polymer relaxation time defined in Eq. (1.4). It is important to remark that the matrix of the velocity gradient tensor has entries $\boldsymbol{\nabla}\boldsymbol{u} = \partial_i u_j$. Here the conformation tensor $\boldsymbol{\sigma}$ is normalized by the equilibrium size R_0 of the molecules, so that in the absence of an external fluid flow it relaxes to the unit tensor $\mathbf{1}$.

Equation (1.7) must be supplemented by the evolution equation for the velocity field, which is derived from the momentum conservation law:

$$\frac{\mathrm{D}u_i}{\mathrm{D}t} = \frac{1}{\rho_f}\frac{\partial T_{ij}}{\partial x_j} + f_i \tag{1.8}$$

where ρ_f is the density of the fluid, $\boldsymbol{u}$ is the velocity field, $\boldsymbol{T}$ is the stress tensor of the fluid and $\boldsymbol{f}$ is the sum of the body forces per unit mass.
The symbol $\frac{\mathrm{D}}{\mathrm{D}t}$ in Eq. (1.8) is known as the *material derivative* and is expressed as follows:

$$\frac{\mathrm{D}\boldsymbol{u}}{\mathrm{D}t} = \frac{\partial \boldsymbol{u}}{\partial t} + \boldsymbol{u}\cdot\nabla\boldsymbol{u} \tag{1.9}$$

The total stress tensor of the fluid is given by

$$\boldsymbol{T} = \boldsymbol{T}^N + \boldsymbol{T}^P \tag{1.10}$$

where $\boldsymbol{T}^N$ is the viscous stress tensor and $\boldsymbol{T}^P$ is an extra elastic stress tensor.

The stress tensor in a Newtonian fluid is proportional to the rate of deformation, with constant of proportionality the viscosity of the fluid, and in the incompressible case, is usually expressed as

$$T^N_{ij} = -P\delta_{ij} + \mu\left(\partial_j u_i + \partial_i u_j\right) \tag{1.11}$$

where μ is the dynamic viscosity of the solvent and P is the pressure.

In the case of a visco-elastic solution, in the presence of polymers, the elastic stress tensor $\boldsymbol{T}^P$ takes into account the elastic forces. In the Hookean approximation for the elasticity of the single polymer, the elastic stress tensor is proportional via the Hooke modulus to the deformation tensor $\boldsymbol{T}^P = nHR_iR_j$. The elastic stress tensor per unit volume of fluid is obtained by summing the average contribution given by each polymer:

$$\boldsymbol{T}^P = nH\left\langle R_iR_j\right\rangle = nHR_0^2\boldsymbol{\sigma} \tag{1.12}$$

where n is the concentration of polymer molecules.

For an incompressible fluid of constant density ρ_f, substituting the expression for the elastic stress tensor into the momentum conservation law yields

$$\partial_t\boldsymbol{u} + (\boldsymbol{u}\cdot\boldsymbol{\nabla})\boldsymbol{u} = -\frac{\boldsymbol{\nabla}p}{\rho_f} + \nu_s\Delta\boldsymbol{u} + \frac{2\eta\nu_s}{\tau}\boldsymbol{\nabla}\cdot\boldsymbol{\sigma} + \boldsymbol{f} \tag{1.13}$$

where $\nu_s = \mu/\rho$ is the kinematic viscosity of the solvent and η is the zero-shear contribution of the polymers to the total viscosity of the solution $\nu = \nu_s(1+\eta)$:

$$\eta = \frac{nHR_0^2\tau}{2\mu}$$

Equation (1.7) together with Eq. (1.13) completely determines the dynamics of the Oldroyd-B model.

1.3.2.2 The FENE-P model

The Oldroyd-B model is based on the assumption that the molecules of the polymer can be modelled as Hookean springs, and consequently it allows for infinite extensions of the polymers. This is unphysical because the maximum length $R_{\max}$ bounds the polymer end-to-end separation R. Moreover,

the linear dumbbell model fails, and non-linearity becomes essential, when the polymer extension R approaches $R_{\max}$. A more refined, but still conceptually simple, description is that of the *Finite Extensible Nonlinear Elastic model (FENE model)*, where the elastic constant H is replaced by the function

$$H(R^2) = H\frac{R_{\max}^2 - R_0^2}{R_{\max}^2 - R^2} \tag{1.14}$$

diverging for $R \to R_{\max}$, which means that the restoring force becomes infinite when the polymer is extremely stretched.

Nevertheless, the introduction of non-linearities yields a non-linear evolution equation for the conformation tensor $\langle R_i R_j \rangle$, which is not closed. A commonly accepted closure is the Peterlin approximation [72], consisting in a pre-averaging in the non-linear function:

$$H(R^2) = H\frac{R_{\max}^2 - R_0^2}{R_{\max}^2 - \langle R^2 \rangle} \tag{1.15}$$

This approximation leads to the following coupled equations for the velocity field $\boldsymbol{u}$ and the conformation tensor $\boldsymbol{\sigma}$, in the FENE-P model:

$$\partial_t \boldsymbol{u} + (\boldsymbol{u}\cdot\boldsymbol{\nabla})\boldsymbol{u} = -\frac{\boldsymbol{\nabla} p}{\rho_f} + \nu_s \Delta \boldsymbol{u} + \frac{2\eta\nu_s}{\tau} H(tr(\boldsymbol{\sigma}))\boldsymbol{\nabla}\cdot\boldsymbol{\sigma} + \boldsymbol{f} \tag{1.16}$$

$$\partial_t \boldsymbol{\sigma} + (\boldsymbol{u}\cdot\boldsymbol{\nabla})\boldsymbol{\sigma} = (\boldsymbol{\nabla}\boldsymbol{u})^T\cdot\boldsymbol{\sigma} + \boldsymbol{\sigma}\cdot(\boldsymbol{\nabla}\boldsymbol{u}) - 2\frac{H(tr(\boldsymbol{\sigma}))\boldsymbol{\sigma} - \mathbf{1}}{\tau}. \tag{1.17}$$

where the non-linear factor $H(tr(\boldsymbol{\sigma}))$ is

$$H(tr(\boldsymbol{\sigma})) = \frac{tr_{\max} - tr(\mathbf{1})}{tr_{\max} - tr(\boldsymbol{\sigma})} \tag{1.18}$$

with $tr_{\max} = R_{max}^2/R_0^2$.

The FENE-P model is more accurate than the Oldroyd-B model in reproducing some of the features of polymer solutions, such as shear thinning, which are not included in the Oldroyd-B model. This model generally reproduces a more accurate scaling behaviour for the shear viscosity and the normal stress differences, and hence agrees well with the experimental measurements. Moreover, in numerical applications, the finite molecular extensibility reduces the onset of numerical instabilities due to the strong gradients of the conformation tensor field. For these reasons, this model is usually adopted in numerical simulations of visco-elastic channel flows [73–75].

1.4 Elastic turbulence: An overview

1.4.1 Experiments and theoretical investigations

One of the remarkable effects of polymers is that polymers with a long relaxation time τ and sufficiently high Weissenberg number Wi are capable of giving rise to an irregular flow regime with velocity fluctuations spanning a broad range of spatial and temporal scales even in the limit of vanishing Reynolds number Re. The Reynolds number accounts for inertial instabilities and is defined by

$$Re = \frac{UL}{\nu} \tag{1.19}$$

where U and L are, respectively, characteristic velocity and length scales and ν is the total viscosity of the solution.

This irregular state caused by an instability due to the polymer stresses at high Wi and in the limit of vanishing inertia, i.e. low Re, is known as *elastic turbulence*. The first quantitative experiments to demonstrate the onset of elastic turbulence were performed in a swirling visco-elastic flow of polymer solutions between two plates with a wide gap, in [21].

Steinberg and coworkers have identified a principal measure of elastic turbulence by measuring the ratio between the average shear stress and its corresponding value for a laminar flow between two rotating circular plates (see Ref. [21]). When the relative angular velocity between the two plates is increased, the average rescaled shear stress grows significantly, showing a sharp transition. The same maximum stress value is found in a corresponding flow of a Newtonian fluid for $Re \sim 10^4$, whereas the measurements were taken at $Re < 1$, showing that these effects are due to fluid elasticity.

The frequency power spectrum of the velocity fluctuations in elastic turbulence displays a power-law decay, which spans about a decade in frequencies (see Fig. 1.5). The power-law dependence indicates that there is a broad range of timescales of the motion. It resembles that of the developed turbulence of a Newtonian fluid at high Re, but the energy spectrum has a steeper slope, i.e. the velocity fluctuations in elastic turbulence are concentrated at low wave numbers [8, 18, 21, 76]. This indicates that the flow is temporally irregular and driven by a few large scales.

Qualitatively, the polymers are stretched by the shear flow, thus triggering purely elastic instabilities. These instabilities give rise to a secondary flow that acts back on the polymer molecules, stretching them further, and becomes increasingly turbulent, until a kind of saturated dynamic state is finally reached [18, 21, 23]. The fluctuating velocity field can be seen in the

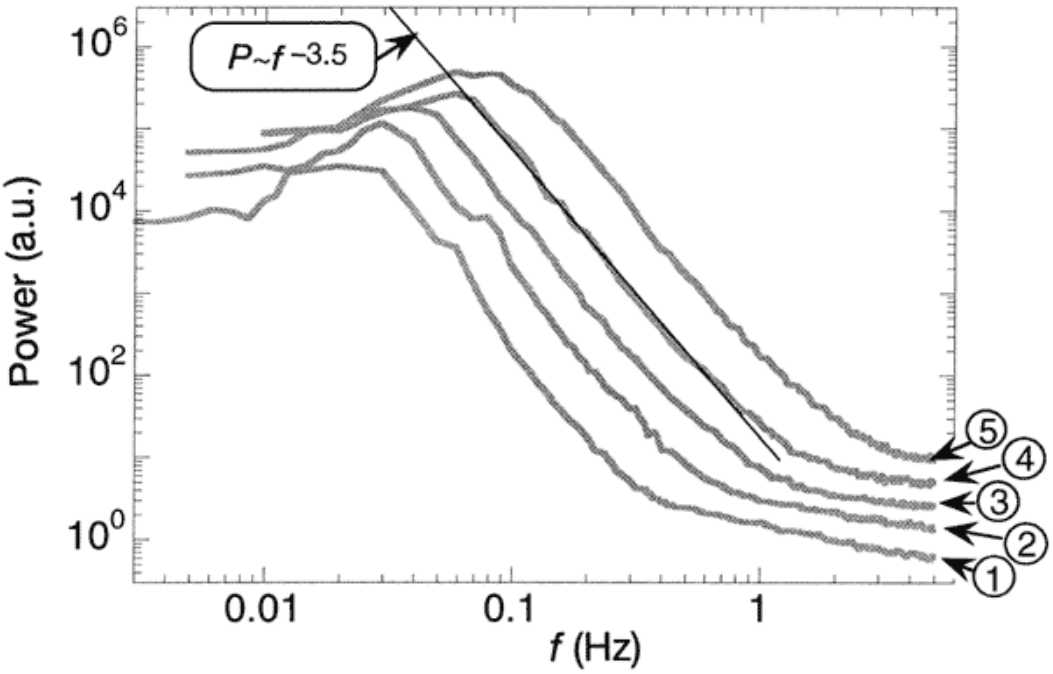

Figure 1.5: Power spectra of velocity fluctuations. The data were obtained at different shear rates $\dot{\varepsilon}$. Curves $1-5$ correspond to $\dot{\varepsilon} = 1.25, 1.85, 2.7, 4$ and $5.9s^{-1}$, respectively. The spectrum of fluctuations is fitted by a power law, $P \approx f^{-3.5}$, for $\dot{\varepsilon} = 4s^{-1}$. The figure is taken from the experiments of Groisman and Steinberg [21].

snapshots of the flow of the polymer solution above the transition, as shown in Fig. 1.6. The authors established that the onset of this new flow regime is due to a large elastic stress. Subsequently, a detailed experimental investigation was carried out by the same authors in three different systems: a shear flow between two circular plates, a Couette–Taylor flow, and a flow in a curvilinear channel (Dean flow) [25] (as shown in Fig. 1.7). The elastic turbulent flows are found to be highly correlated over space and the Eulerian temporal auto-correlation function decays rather fast with characteristic correlation times comparable to the largest polymer relaxation time [76]. Later, in 2006, a detailed experimental study of the previously unexplored transitional pathway from laminar to elastic turbulence provided a rich series of secondary flow states connecting the simple torsional shearing flow in a parallel plate device with elastic turbulence [77]. It has been found that the secondary-flow states involve axisymmetric rolls and non-axisymmetric spirals that compete at high Weissenberg number, producing oscillations,

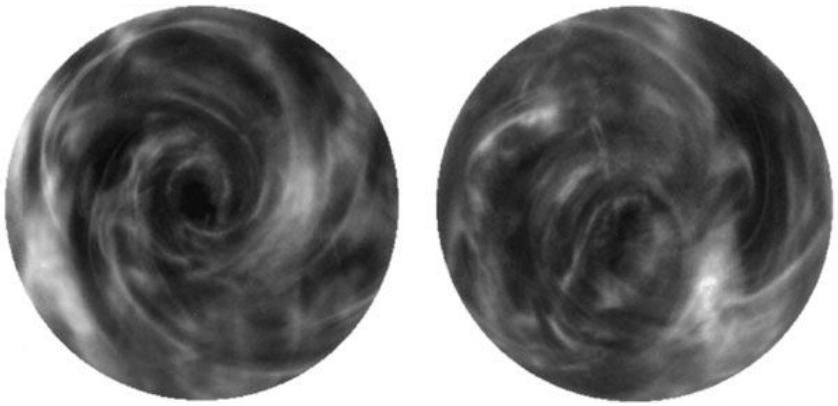

Figure 1.6: Two representative snapshots of the polymer flows at $Wi = 13$, $Re = 0.7$ taken from below. Figures are taken from the experiments of Groisman and Steinberg [21].

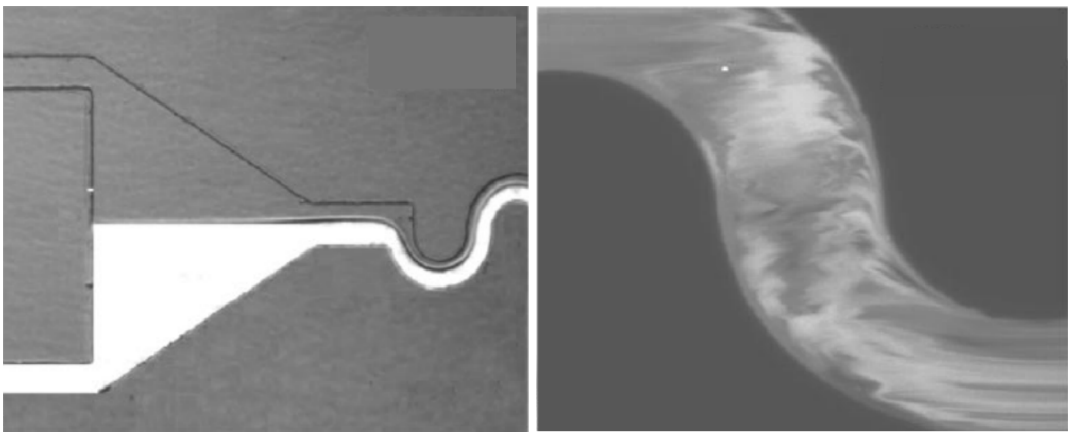

(a) (b)

Figure 1.7: (a) Epifluorescent microphotograph of the entrance area of a microchannel used in experiments on mixing. Wide triangular region in front of a curvilinear channel allows adjusting equal flow rates for polymer solutions. (b) Confocal image of mixing in chaotic flow in the microchannel. Figures are taken from the experiments in a curvilinear micro-channel of a dilute solution of a high molecular weight polymer [18].

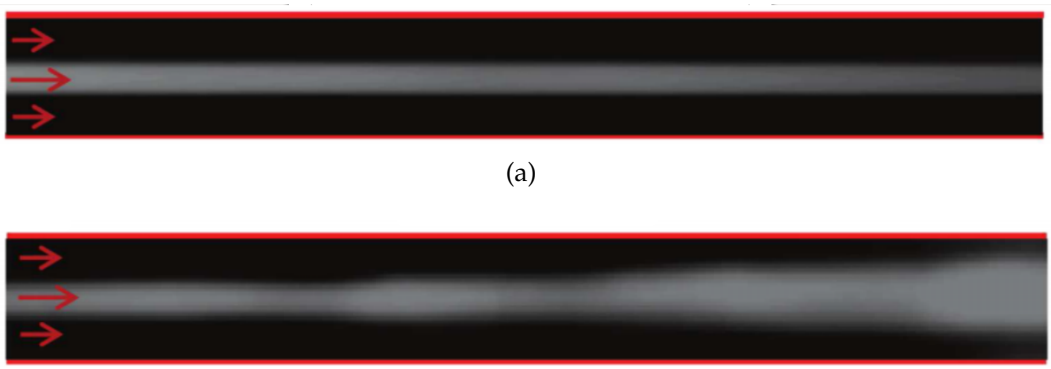

(a)

(b)

Figure 1.8: Sample snapshots of dye advection experiments in straight microchannel system at $Re < 0.01$. (a) Newtonian case, (b) polymeric case, with $Wi = 10.9$. The figure is taken from [26].

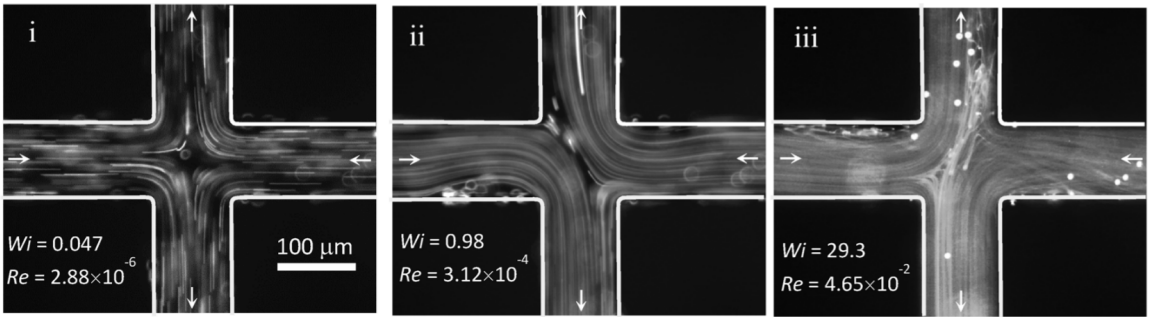

Figure 1.9: Flow patterns of visco-elastic fluid in the cross-slot geometry (i) Newtonian-like symmetric flow behaviour, (ii) steady asymmetric flow, and (iii) time-dependent flow. The figure is taken from [78].

apparent chaotic flow, and, eventually, apparent elastic turbulent flow with a broad spectrum of temporal fluctuations. The elastic turbulent flows are also characterized by divergent Lagrangian trajectories and, positive finite time Lyapunov exponents, could be measured by direct tracking of fluid particles in the flow and numerical integration of the measured flow velocity fields [23]. Systematic experiments performed in a von Karman flow between two disks by means of Laser Doppler Velocimetry and Digital Particle Image Velocimetry revealed a new characteristic space scale of the elastic turbulence, namely the width of the stress boundary layer [76]. A qualitative agreement with the theory of the elastic turbulence (discussed later) is found in terms of a saturation of the root mean square of fluctuations of the velocity gradients in the bulk of the flow [27].

Since the pioneering work by Steinberg and coworkers, various microfluidic experiments have been performed to study elastic turbulence. In recent publications [18, 22, 27, 28, 79–82], it has been shown how these features of turbulence came into view in a highly elastic polymer solution at low Re in curvilinear flows, straight streamlines (as shown in Fig. 1.8), pipe flows and a cross-slot device (as shown in Fig. 1.9) [26, 78]. The behaviour of the flow observed for visco-elastic fluids is far more complex than that found for a Newtonian fluid. It is observed that visco-elasticity can lead to the onset of different types of purely elastic instabilities, depending on the rheological properties of the fluid. Other than in polymer solutions containing the usual high-molecular weight polymers (polyacrylamide, polyethylene oxide), the turbulent-like behaviour has also been perceived in complex fluids, in particular, using worm-like micelles for the elastic particles [83, 84].
The only existing theory of elastic turbulence in dilute polymer solutions with linear elasticity and the feedback reaction on the flow was published shortly after its discovery by Fouxon, Lebedev and Balkovsky [85, 86]. The major ingredient if the theory of the elastic turbulence is to relate the dynamics if the polymer stress tensor $\boldsymbol{\sigma}$ to the dynamics of a vector field with a linear damping [85–87]. The theory of elastic turbulence is restricted to unbounded flow of a polymer solution and is based upon the major assumption that the local feedback of the stretched polymer molecules on the flow field leads to a statistically stationary state by a saturation of both the polymer contribution to the stress tensor $\boldsymbol{\sigma}$ and the rms of the fluctuations of the velocity gradients (observed experimentally). With this assumption the theory explained the experimentally observed algebraic decay of the spectra of the velocity fluctuations and revealed the existence of an elastic turbulent regime. Latter a systematic description of these elastic instabilities (subcritical) in parallel shear flows of viscoelastic fluids is presented in Ref. [88]. Very recently a theory composed of a microscopic description of the polymer statistics and a macroscopic description of the stresses in a polymer solution has been proposed to investigate the boundary layer properties of elastic turbulence. Theory shows that in contrast to high Re , where the fluctuating velocity if always of the order of the mean flow in the viscous sublayer, wall-bounded elastic turbulence possesses a non-trivial relation between the mean and the fluctuating velocity components [89].

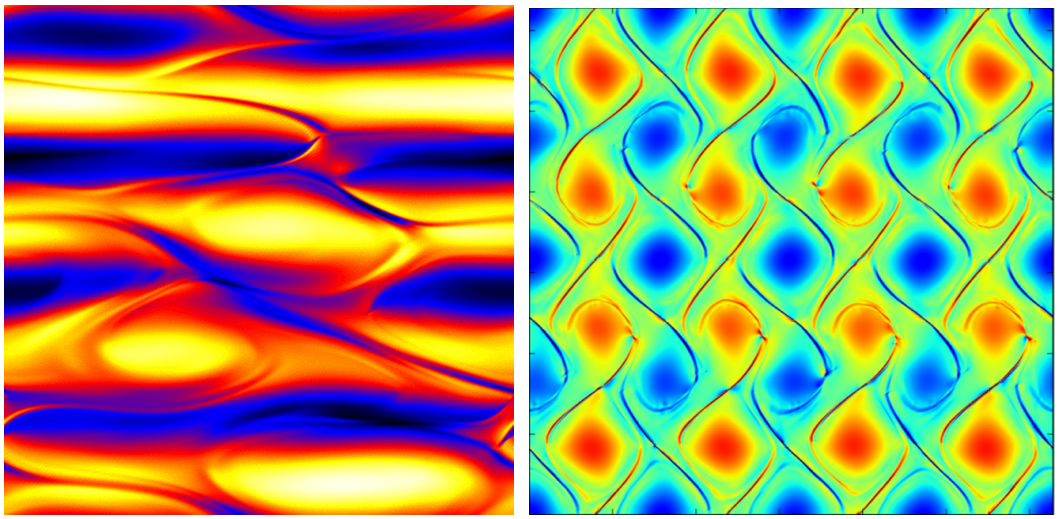

(a) (b)

Figure 1.10: Snapshot of vorticity field in numerical simulations of the two-dimensional Oldroyd-B model (a) $Re = 0.7$ and $Wi = 22.4$ and with a Kolmogorov forcing $\boldsymbol{f} = (F\cos(y/L), 0)$, with $L = 1/4$ and where $F = 64$ is the forcing amplitude. The source of the figure is [90]; (b) $Re = 1$ and $Wi = 20$ with a cellular forcing $f = -Fn\left[\cos(nx) + \cos(ny)\right]$ with $n = 4$ and $F = 0.16$ the forcing amplitude. The figure is taken from [91].

1.4.2 Numerical investigations

Elastic turbulence can also be numerically reproduced at least qualitatively in simulations using polymer solution models, for instance using the two-dimensional Oldroyd-B model, in which only the largest relaxation time of the polymer is retained and the polymer elasticity is assumed to be linear. Preliminary attempts to simulate the elastic turbulence regime have been successful, for simplified 2D flow arrangements, such as the periodic Kolmogorov shear flow ([90–93], Chapter 3). The Kolmogorov force produces a sinusoidal mean flow even in the presence of elastic polymers.

Other constitutive models have been also used to simulate elastic tur-

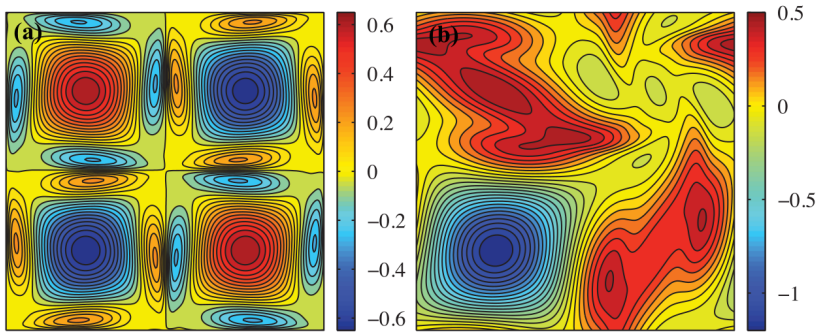

(a)

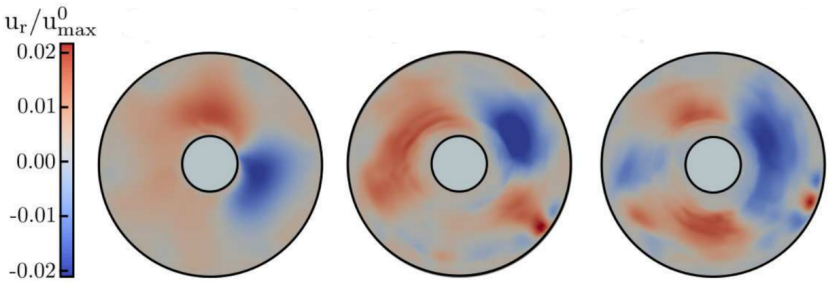

(b)

Figure 1.11: (a) Contour plot of vorticity field for $Wi = 10$ before and after the onset of a symmetry breaking transition. The study was performed by simulating the dynamics of the Oldroyd-B model, in a simple four-roll mill geometry [94]. (b) Snapshots of the normalized radial velocity component $u_r/u_{\max}$ for Weissenberg numbers of $Wi = 12.6$, $Wi = 50.3$ and $Wi = 106.8$ (from left to right) in the 2D Taylor–Couette geometry. The figure is taken from [95].

bulence, such as those with a non-linear elastic force (FENE-P model), by

taking into account the finite extensibility of polymers [96–98]. Numerical studies considering different flow geometries also display the presence of elastic instabilities [91, 94, 95] (see the snapshots of the vorticity field in Fig. 1.10(b) (cellular forcing), Fig. 1.11(a) (four-roll mill geometry) and Fig. 1.11(b) (2D Taylor-Couette geometry)). Very recently, the occurrence of elastic turbulence of a visco-elastic fluid in a 2D Taylor–Couette geometry using the Oldroyd-B model has been investigated [95]. Numerical simulations show that for increasing fluid elasticity, i.e. increasing Weissenberg number Wi, the Taylor–Couette or base flow becomes unstable. A secondary flow is created, which strongly fluctuates in time and which has a non-zero radial component. Snapshots of the normalized radial velocity component $u_r/u_{\max}$ are shown in Fig. 1.11(b).

In fact, even a low-dimensional shell model of visco-elastic fluid reproduces elastic turbulence qualitatively [99]. Consistent with experimental results, numerical simulations indicate that the polymers stretch and apply stronger elastic forces to the flow if Wi is sufficiently high. Numerically, it has been observed that the source of the turbulent stress comes from elasticity and elastic stresses play the role usually played by the Reynold stress in the usual inertial turbulence, which is the hallmark of elastic turbulence [90].

These experimental and subsequent numerical developments demonstrate that based on its similarity with turbulent fluid motion, elastic turbulence has been proposed as an efficient framework to enhance mixing in low Reynolds number flows [22].

The numerical investigation of elastic turbulence in two-dimensional Kolmogorov flows will be the subject of Chapter 3.

Chapter 2

Inertial particles in flows: Equations of motion and measurements of their concentration

Contents

2.1 Introduction

Particle-laden flows are everywhere, both in natural systems (sediments, plankton, aerosols, cloud droplets, etc.) and in human industrial activities (sprays, powders, combustion, extraction of oils, etc.). Predicting the dynamics of an ensemble of material particles transported in turbulent and non-turbulent flows remains a significant problem, which has motivated

countless studies over more than a century. Among the many situations where the transport of particles is of critical importance, a few environmental and industrial issues are worth being highlighted.

For instance, the preferential concentration of inertial particles may enhance the probability of collision (and hence of coalescence) of water droplets in clouds, and therefore play an essential role in the initiation of rain [100, 101]. Similarly, it is believed that it can promote the agglomeration of fine particles in accretion disks, hence accelerating the formation of planetesimals [102]. In industrial applications, it can play a role in the coalescence of fuel droplets in diesel engines, and therefore affect the energetic efficiency, with significant economic and environmental implications [103]. The properties of particle suspensions are affected by the particle concentration as well as the by the properties of the suspending fluid. Indeed, variations of these characteristics induce important qualitative and quantitative changes in the behaviour of the suspension.

It is intuitive that the scenario is even more complex when the suspending fluid itself has a complex rheological behaviour. Several industrial and daily-life materials fall in this category, including rubbers, detergents, paints, foods, and biological suspensions. The usual non-Newtonian properties, such as shear-thinning and the appearance of a normal stress difference, may strongly alter the micro-structure in flowing suspensions, even at low concentrations of particles. On the other hand, the peculiar particle dynamics induced by the complex rheology of the suspending fluid can be cleverly exploited to perform operations that would be difficult in Newtonian fluids. It is worthwhile to mention as an example the emerging use of non-Newtonian fluids in microfluidics to guide the suspended particles to some regions of the devices for counting, targeted drug delivery, diagnostics, the extraction of oils and gases from porous rocks, and particle separation applications [104]. Depending on the size and density of the particles relative to the fluid (eventually responsible for a non-zero response time of the particle due to its inertia), the particles will interact with the structures of the flow of the carrier at different time and spatial scales. Understanding the global dynamics of a particle suspended in Newtonian and non-Newtonian fluid flows is a topic of primary importance.

This chapter is a review of some of the theoretical basis of the model equations which are currently employed to describe the motion of inertial particles under conditions of dilute suspension. This chapter also reviews the basic phenomenology of particle transport in turbulent flows, addressing, for instance, preferential concentration, and the tools currently used for

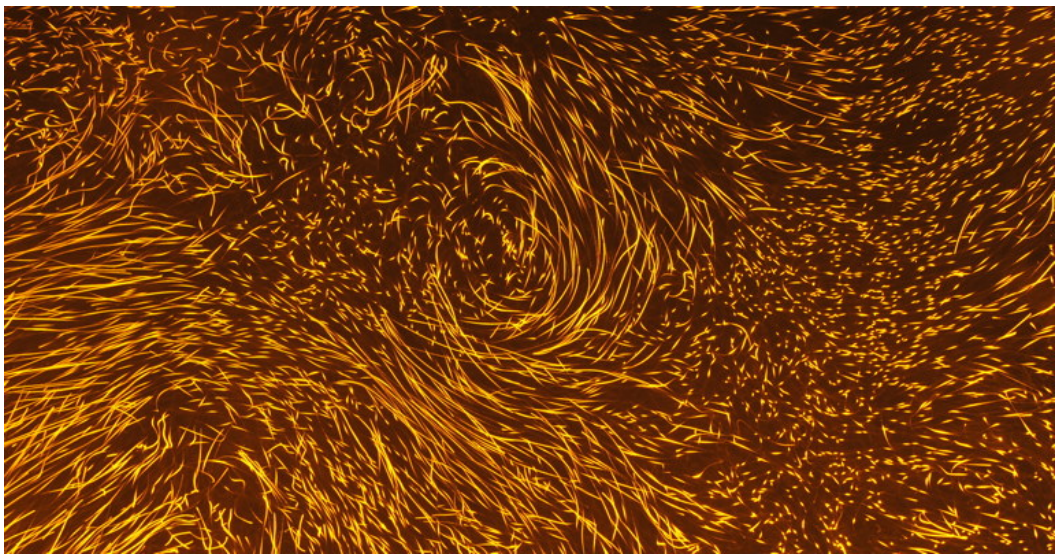

Figure 2.1: Visualization of turbulence by seeding the flow by 10 micron fluorescent polystyrene particles in a turbulent flow experiment (von Karman). The figure is taken from http://nicolas.mordant.free.fr/turbulence.html.

its quantitative characterization.

2.2 The equations of motion for material particles transported by a flow

2.2.1 Lagrangian tracer particles

Fluid tracers are ideal particles which are transported by the flow without being subjected to any hydrodynamical or external force. Such particles, also called non-inertial tracers, are carried by the flow without having any effect on the flow field itself or on other quantities transported by the flow. Consequently, tracers can be thought of as identical to the fluid elements, and with the same density as that of the fluid ($\rho_p = \rho_f$). These particles are ideally point-like and have the same velocity as the underlying fluid:

$$\frac{\mathrm{d}\boldsymbol{x}}{\mathrm{d}t} = \boldsymbol{v}(t) = \boldsymbol{u}(\boldsymbol{x}(t), t) \tag{2.1}$$

where $\boldsymbol{x}$ and $\boldsymbol{v}$ are the position and velocity of tracer, respectively, and $\boldsymbol{u}$ is the velocity field of the fluid.

2.2.2 Inertial particles

Unlike these fluid tracers, particles with a mass density that has a mismatch with that of the fluid ($\rho_p \neq \rho_f$) (either smaller, *e.g.* bubbles, or greater, *e.g.* sand grains) or with a size comparable to the characteristic scales of the flow (such as its smallest eddies) do not follow the flow exactly. Such particles are generally referred to as inertial particles. Particles with a density much greater than the density of the carrier fluid ($\rho_p \gg \rho_f$) are known as heavy inertial particles. In this thesis we only study heavy inertial particles.

The formulation of the problem can be given in the following terms: considering a rigid sphere (density ρ_p and radius a) in a viscous Newtonian flow governed by the Navier–Stokes equations, with no-slip boundary conditions on the surface of the sphere, can we formalize the instantaneous action of the flow on the sphere?

An answer to this longstanding question was formulated successively by Stokes [105] and Basset [106], and later refined by Boussinesq [107] and Oseen [108], who examined the motion of a sphere settling under gravity in a fluid at rest. Their analysis started from the unsteady situation of a sphere settling from rest in a quiescent viscous fluid, which concerns the transient acceleration until it reaches its terminal settling velocity. The difficulties encountered in this problem are independent of the dynamical regime of the fluid flow. The disturbance flow produced by the motion of the sphere was considered to have a sufficiently low Reynolds number ($Re_p \ll 1$) so that the fluid force on the sphere could be estimated from a Stokes flow (so that a second Reynolds number based on the spatial scale of shear is also small ($Re_S < 1$)). Tchen extended this work to a sphere settling under gravity in a non-uniform flow, with a view already to turbulent flows [109]. The resulting model (known as BBOT, Basset–Boussinesq–Oseen–Tchen) was revised in 1983 and proper account taken of the Faxen correction for the unsteady Stokes flow, simultaneously by Maxey and Riley [110] and Gatignol [111], leading to the following equation of motion for a particle in a flow:

$$m_p \frac{\mathrm{d}\boldsymbol{v}}{\mathrm{d}t} = 6\pi\mu a(\boldsymbol{u}-\boldsymbol{v}) + \frac{1}{2}m_f \frac{\mathrm{d}(\boldsymbol{u}-\boldsymbol{v})}{\mathrm{d}t} + m_f \frac{\mathrm{D}\boldsymbol{u}}{\mathrm{D}t} + (m_p - m_f)\boldsymbol{g} + 6a^2\sqrt{\pi\rho_f\mu}\int_{-\infty}^{t} \frac{\mathrm{d}(\boldsymbol{u}-\boldsymbol{v})}{\mathrm{d}t}\frac{\mathrm{d}t^*}{\sqrt{t-t^*}} \tag{2.2}$$

where $\boldsymbol{v}$ is the velocity of the particle, $\boldsymbol{u}$ is the velocity field of the unperturbed flow of the carrier, a is the radius of the particle, m_p is the mass of the particle, ρ_f is the density of the carrier fluid, m_f is the mass of the fluid displaced by the particle, and μ is the dynamic viscosity of the carrier fluid.

The terms on the right hand side of Eq. (2.2) are, in order of appearance,

- the Stokes drag force (due to the relative velocities of the particle and fluid), also called the steady drag term,
- the added mass force, which is purely inertial, and corresponds to the force exerted by the displaced fluid,
- a pressure gradient term, which is equivalent to the acceleration of a particle of the fluid at the position of the centre of the particle,
- the buoyancy force,
- a history term (an unsteady drag term), which takes into account the entire history of the motion of the particle in the carrier fluid up to the instant t and mainly takes into account the interaction of the particle with its own wake.

The actual range of validity of this equation is, however, limited, as it is only valid for vanishing particle Reynolds number $Re_p = 2a\,|\boldsymbol{u} - \boldsymbol{v}|\,/\nu \ll 1$, as it assumes a Stokes flow around the particle due to the relative velocity $(\boldsymbol{u}-\boldsymbol{v})$ between the fluid and particle, and that the particles are much smaller than the local non-uniformities of the flow, so that $Re_S = 2aL_s/\nu$ (with L_s the scale of the variation of the flow) is small, i.e. $\ll 1$. In spite of these severe limitations, apart from some first order corrections to take into account the effects of a non-zero Re_p and local non-uniformities of the flow around the particle, the model still remains the best analytical expression we have to describe the fluid–particle interaction.

A commonly used version of Eq. (2.2) for passively advected particles of non-zero size is

$$\begin{cases} \dot{\boldsymbol{x}} = \boldsymbol{v}(t) \\ \dot{\boldsymbol{v}} = \dfrac{\boldsymbol{u}(\boldsymbol{x},t) - \boldsymbol{v}(t)}{\tau_p} \end{cases} \tag{2.3}$$

where τ_p is the viscous relaxation time of the particle [110]. This simplified model is also referred to as a Stokesian model. The main assumption required by this model is the validity of the following approximation:

- the velocity field is well-defined at the particle scale, allowing, for instance, defining the velocity of the fluid at the position of the particle.

Note that this equation is valid for small Re_p. The dynamics of inertial particles have been studied extensively in the past either numerically [112–117]

or experimentally [116, 118–120] and the most important phenomenon observed in these studies, which is a direct result of the simplified Eq. (2.3), is that particles with a density different from the fluid density tend not to remain uniformly distributed, even in homogeneously isotropic turbulent flows.

2.3 The Stokes number

In the conditions under which Eq. (2.3) is valid, the inertia of the particle is quantified by a single dimensionless parameter, namely the Stokes number St, defined as the response time τ_p of the particle relative to some characteristic time scale of the underlying flow (for instance, the dissipative time scale in turbulence) τ_f.

$$St = \frac{\tau_p}{\tau_f} \text{ with } \tau_p = \frac{2\rho_p a^2}{9\rho_f \nu} \tag{2.4}$$

Throughout this thesis, we define $\tau_f \equiv \tau_{\dot{\gamma}}$ in terms of the strain rate exerted by the flow, so that $St = \tau_p/\tau_{\dot{\gamma}}$, with $\tau_{\dot{\gamma}} = 1/\overline{\dot{\gamma}}$ and $\overline{\dot{\gamma}}$ given by

$$\overline{\dot{\gamma}} = \frac{1}{TL_0^2}\int_0^T dt \int_0^{L_0} dy \int_0^{L_0} dx \sqrt{2[\boldsymbol{\nabla u} + (\boldsymbol{\nabla u})^T]^2}, \tag{2.5}$$

where $\overline{(...)}$ denotes taking the average over the spatial coordinates and time, L_0 being the size of the domain in each direction.

2.4 The distribution of the particles in a flow

As mentioned earlier, the collective motion of material particles whose density is different from that of the fluid is expected to behave differently than fluid tracers. In particular, drag forces make the dynamics of such impurities dissipative. Dissipative dynamics implies that the particle trajectories asymptotically evolve to a dynamical attractor in the phase space spanned by the positions and velocities of the particles. Consequently, even if the fluid flow $\boldsymbol{u}$ is incompressible, solid impurities, i.e. heavy inertial particles, can eventually become distributed very inhomogeneously. Both from a fundamental and an applied point of view, the most interesting feature that emerges is the appearance of strongly inhomogeneous particle distributions, namely clustering. The clustering mechanisms of inertial particles have been studied in the context of turbulent as well as laminar flow field

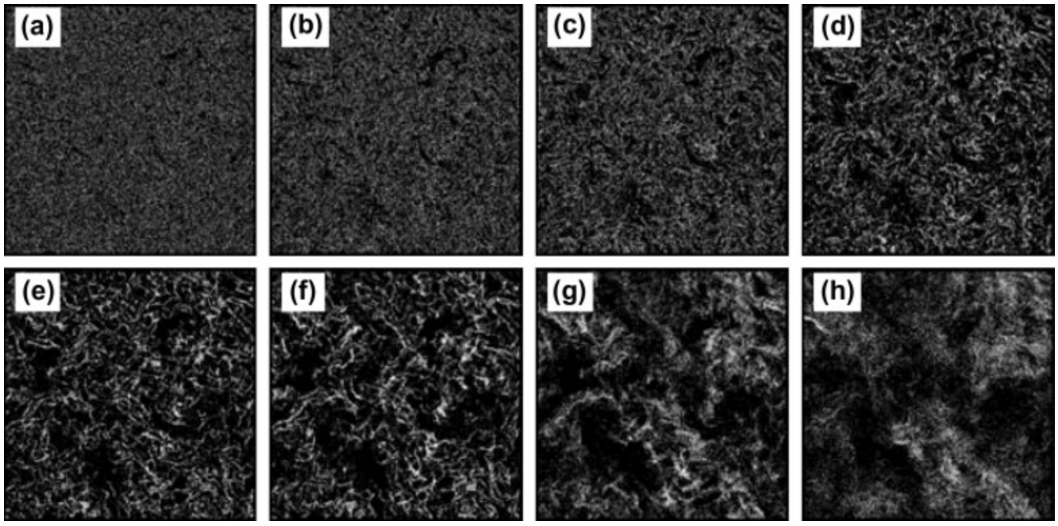

Figure 2.2: Spatial distribution of particles inside a thin layer (width $5\eta_k$) for 8 different Stokes numbers. (a) $S_n = 0.05$, (b) $S_n = 0.1$, (c) $S_n = 0.1$, (d) $S_n = 0.2$, (e) $S_n = 0.5$, (f) $S_n = 1$, (g) $S_n = 5$, (h) $S_n = 10$. Simulation results are from [122].

models [36, 121]. It is useful to briefly discuss the clustering mechanism of inertial particles.

2.4.1 The mechanism of preferential concentration

The origin of the preferential concentration of inertial particles in a carrier fluid can be understood at several levels, from very fundamental and generic considerations related to the dissipative nature of the particle dynamics, to more intuitive arguments based on the interaction between the particles and the structures of the carrier fluid. The following discussion will briefly address some of these aspects.

Inertial particle dynamics as a dissipative dynamical system: Consider a system whose state is specified by a point $\boldsymbol{q} = (q_1, q_2, ...)$ in a given state space Q. For a dynamical system, the state can evolve in time, and the evolution from one state to another follows a vectorial differential equation given by a rule g such that

$$\frac{\mathrm{d}\boldsymbol{q}}{\mathrm{d}t} = \boldsymbol{G}(\boldsymbol{q}) \tag{2.6}$$

where $\boldsymbol{q} \in Q$ and with the initial condition $\boldsymbol{q}(t=0) = \boldsymbol{q}_0$. An initial probability density of states can be defined as $P(\boldsymbol{q}, t=0)$, such that $\int_Q P(\boldsymbol{q}, t=0)\mathrm{d}\boldsymbol{q} = 1$ and $P(\boldsymbol{q}, t=0)\mathrm{d}\boldsymbol{q}$ is the probability of finding the system in an elementary volume $\mathrm{d}\boldsymbol{q}$ around the state $\boldsymbol{q}$ at time $t=0$. The evolution equation for the density of states $P(\boldsymbol{q}, t)$ at time t is

$$\frac{\mathrm{D}_{\boldsymbol{G}} P}{\mathrm{D}t} = \partial_t P + \boldsymbol{G}\cdot\boldsymbol{\nabla} P = -P\boldsymbol{\nabla}\cdot\boldsymbol{G}. \tag{2.7}$$

Equation (2.7) is nothing but a continuity equation ensuring that for all times $t > 0, P(\boldsymbol{q}, t)$ defines a probability density, i.e. $\int_Q P(\boldsymbol{q}, t)\mathrm{d}\boldsymbol{q} = 1$. Note that $\frac{\mathrm{D}_{\boldsymbol{G}} P}{\mathrm{D}t}$ can be seen as the material derivative in the flow $\boldsymbol{G}$. Depending on the value of the term $\boldsymbol{\nabla}\cdot\boldsymbol{G} = \partial_{q_i} G_i$, the dynamical system has two distinct kinds of behaviour:

- If $\boldsymbol{\nabla}\cdot\boldsymbol{G} = 0$, then Eq. (2.7) becomes $\frac{\mathrm{D}P}{\mathrm{D}t} = 0$, which implies that $P = \mathrm{const}$ for an incompressible flow. This also implies that volumes in phase space are conserved. In particular, if the initial states are uniformly distributed, then they remains uniformly distributed at all subsequent times. This result is known as Liouville's theorem. Dynamical systems such that $\boldsymbol{\nabla}\cdot\boldsymbol{g} = 0$ are conservative.

- If $\boldsymbol{\nabla}\cdot\boldsymbol{G} < 0$, then $\frac{\mathrm{D}P}{\mathrm{D}t} > 0$ and eventually the density along the fluid trajectories in the state space grows exponentially. Dynamical systems such that $\boldsymbol{\nabla}\cdot\boldsymbol{G} < 0$ are dissipative. As the integral of P over the whole state space is 1, this means that the density of states in other regions must decrease. In particular, if the initial density is uniform, this will result in the long term in there being regions with a high density of states and depleted regions. This resulting contraction is related to the existence of attractors.

This completely general mechanism can be applied to the dynamics of Lagrangian tracers and inertial particles in flows:

- for Lagrangian tracers, the dynamical system is simply defined by the state variable $\boldsymbol{q} = \boldsymbol{x}$ (where $\boldsymbol{x}$ denotes the position of a tracer) and the flow $\boldsymbol{G} = \boldsymbol{u}$ is the fluid flow itself. The evolution equation of the dynamical system (Eq. (2.6)) thus implies $\frac{\mathrm{d}\boldsymbol{x}}{\mathrm{d}t} = \boldsymbol{u}(\boldsymbol{x}, t)$. For incompressible flows $\boldsymbol{\nabla}\cdot\boldsymbol{u} = 0$, thus in the terminology of dynamical systems, the system is conservative, and an initially uniform distribution of particles remains uniform. Hence, in incompressible flows, Lagrangian tracers do not form clusters.

- In contrast, for inertial particles, the dynamical system is dissipative. To understand this, we consider the minimal Stokesian model given by Eq. (2.3), where the particle dynamics are coupled to that of the fluid by the Stokes drag τ_p. In this case, we can define a dynamical system based on the state variable $\boldsymbol{q} = (\boldsymbol{x}, \boldsymbol{v})$ in position–velocity phase space: the flow function is $\boldsymbol{G} = (\boldsymbol{v}, (\boldsymbol{u} - \boldsymbol{v})/\tau_p)$. Therefore, one has $\boldsymbol{\nabla} \cdot \boldsymbol{G} = -d/\tau_p < 0$, where d is the dimension of physical space. As a result, the system is dissipative, meaning that an initially uniform probability density will evolve to a clustered one.

In general, as will be shown, even if the fluid flow is incompressible, the velocity field $\boldsymbol{v}$ of spatially distributed particles is weakly compressible. The non-zero divergence of the particle velocity is the central origin of the well-known phenomenon of *preferential concentration*, which occurs in physical space. Mehlig and Wilinkson [123, 124], Bec [125] and many others [31, 116, 120, 126] have studied the dissipative nature of the inertial particle dynamics in turbulent flows. These studies show that the underlying attractors depend on the topology of the carrier flow $\boldsymbol{u}$ and the particle response time τ_p.

2.4.2 Correlation of preferential concentration with the fluid flow

The usual intuitive understanding of the clustering of inertial particles relies on the centrifugal expulsion of inertial particles. As the outcome, heavier particles are expected to accumulate preferentially in regions of low vorticity, whereas light particles are expected to accumulate preferentially in regions of high vorticity. This process is schematically illustrated in Fig. 2.3. Maxey [127] has formalized the observed phenomenology, in the limit of small τ_p. One can formally write a perturbative expansion for small τ_p of Eq. (2.3) [85]

$$\begin{aligned} &\text{In the limit of } \tau_p \to 0, \boldsymbol{v} \approx \boldsymbol{u} \\ \implies\ & \tau_p \dot{\boldsymbol{u}} \simeq \boldsymbol{u} - \boldsymbol{v} \\ \implies\ & \boldsymbol{v} \simeq \boldsymbol{u} - \tau_p(\partial_t \boldsymbol{u} + \boldsymbol{u} \cdot \boldsymbol{\nabla} \boldsymbol{u}) \end{aligned} \tag{2.8}$$

which correctly reproduces the tracer limit $\boldsymbol{v} = \boldsymbol{u}$ for $\tau_p = 0$, i.e. $\rho_p = \rho_f$. Within the limits of validity of this approximation, similar to that for tracers, the phase space reduces to the position space and inertia is accounted for by the particle velocity field $\boldsymbol{v}(\boldsymbol{x}, t)$, that is the same as that for the fluid $\boldsymbol{u}(\boldsymbol{x}, t)$.

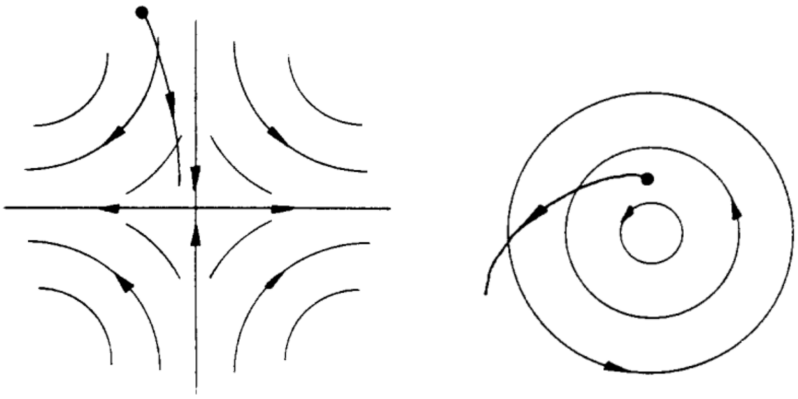

Figure 2.3: Schematic illustration, as proposed by Squires and Eaton (1994) [112] of the mechanism of the ejection of a heavy particle from a region of high vorticity (right) to one dominated by strain (left) in a two-dimensional flow. The right diagram shows streamlines around a vortex and the trajectory of a particle being ejected. The left diagram shows that this puts the particle into a region of high strain (between vortices). The source of the figure is [112].

From non-zero τ_p, the compressibility of the velocity field $\boldsymbol{v}$ can be estimated by taking the divergence in physical space of Eq. (2.8), which results in

$$\boldsymbol{\nabla} \cdot \boldsymbol{v} = -\tau_p \, tr \left[\boldsymbol{\nabla u} \cdot (\boldsymbol{\nabla u})^T \right], \tag{2.9}$$

Those regions can be identified by switching to index notation. On decomposing the fluid velocity gradient γ into its symmetric $\boldsymbol{S}$ and anti-symmetric $\boldsymbol{\Omega}$ parts, we then have

$$\boldsymbol{\nabla} \cdot \boldsymbol{v} = 2\tau_p Q, \tag{2.10}$$

where, up to redefining by employing a prefactor,

$$Q = \frac{1}{2}(\Omega_{ij}\Omega_{ij} - S_{ij}S_{ij}) \tag{2.11}$$

is the Okubo–Weiss parameter [128,129]. In the above equation, S_{ij}, respectively, Ω_{ij} indicate the elements of the rate-of-strain ($\boldsymbol{S}$) and rate-of-rotation ($\boldsymbol{\Omega}$) tensors, and summation over repeated indices is assumed. Particles concentrate due to the (weak) compressibility of their velocity, that is where $\boldsymbol{\nabla} \cdot \boldsymbol{v} < 0$. From Eq. (2.10) it is seen that this condition translates into negative values of Q, meaning that the particles are expected to preferentially accumulate in strain-dominated regions (using Eq. (2.11)).

We would like to remark that small-scale particle clustering has also been observed in laminar flows, both in steady and in time-dependent/chaotic ones [36, 130]. In these types of flows, including spatially smooth and temporally random ones like those of elastic turbulence, there are regions where $Q \neq 0$. The parameter $Q = \frac{1}{2}(\Omega_{ij}\Omega_{ij} - S_{ij}S_{ij})$ is zero only if the terms $S_{ij}S_{ij}$ and $\Omega_{ij}\Omega_{ij}$ compensate exactly, as for instance in plane shear flows.

2.4.3 Assessment of preferential concentration

In this section, we will describe the many methods used to study and characterize preferential concentration and clustering in flows (mainly in numerical studies). First, we focus on direct methods that are all more or less linked to measurements of the concentration. Then we present some indirect methods that use dynamical measurements to evidence a preferential concentration of the flow by inertial particles. It is implicitly assumed that all the methods described here try to quantify the difference between an uniform particle distribution and the considered concentration fields (actual particle density fields). Most of the usual approaches to quantify the level of clustering are based on the local concentration fields. There are several methods to characterize clustering, including *visualizations*, the *clustering index*, *box-counting*, *pair correlation*, often referred as the radial distribution function, and *Voronoi* analysis.

Visualizations: In studies based on numerical simulations, often a qualitative analysis of the preferential concentration of inertial particles is made through visualization. In two-dimensional [133, 134] and three-dimensional [37, 118, 122, 125, 135, 136] direct numerical simulations, there has been provided a qualitative analysis associated with increasing St, from the tracer limit up to values on the order of 10. In this strand of the literature, the results have been consistent even for different ways of modelling the forces acting on the particles. For the Lagrangian tracers, the particles are homogeneously distributed and as St increases, some areas start getting denser and denser while others become empty. The maximum of the concentration gradients is observed for St around unity.

Box-counting methods: In these methods, starting from n-dimensional data, whatever value of n (an integer), the n-dimensional space is divided into N boxes of equal size, defined by an arbitrarily chosen length scale r,

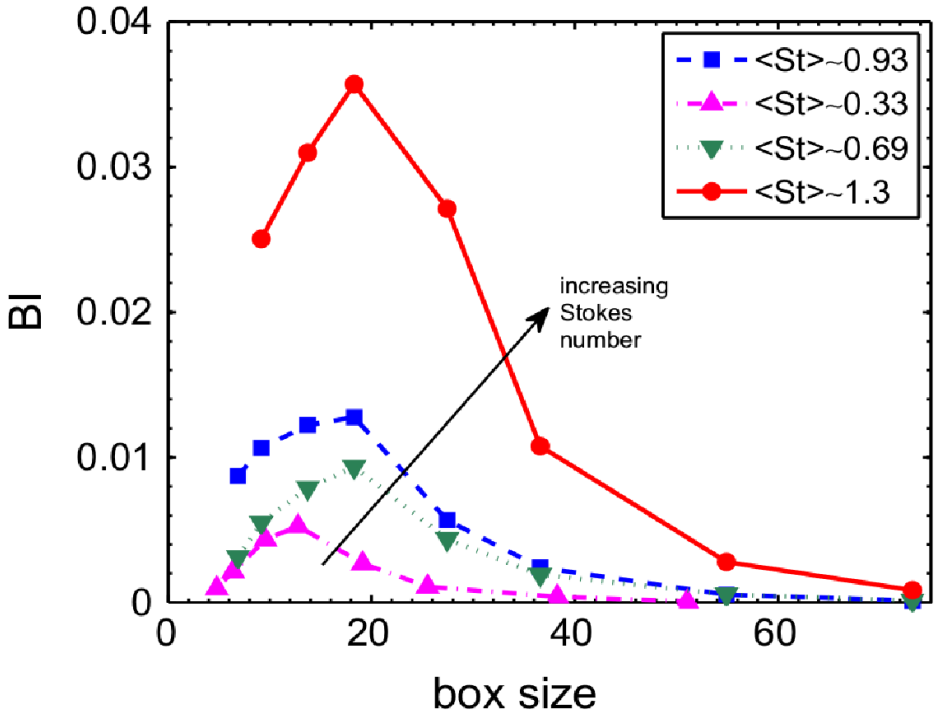

Figure 2.4: Dependence of the box index on the box size for different experiments at different Stokes numbers. The source of the figure is [131], where the results come from experiments performed in a large wind tunnel [132].

so that N boxes fill the whole space of the data. To measure the concentration and/or characterize the preferentially concentrated regions, one counts how many particles belong to each box of size r. In the case of uniformly distributed particles, the probability density function (PDF) of the number of particles per box is described by a Poisson distribution. In the presence of clustering, boxes with very high and very low numbers of particles will be much more likely to exist than in the Poisson case, and so the associated PDF will differ from the Poisson distribution. It is then possible to calculate the distance between these two PDFs using some appropriate norm to obtain a single scalar that characterizes how far the particle distribution is from an uniform one. Such a scalar is referred to as a box index BI [131,137]. The dependence of BI on the box size obtained in [131] is shown in Fig. 2.4. All the curves acquire a similar shape, regardless of the Stokes number, and one notes that the curves associated to Stokes numbers closer to 1 are shifted upward, evidencing the enhancement of the preferential concentration.

Voronoi analysis: This is a recently introduced method and has been found to be particularly well suited to investigating the preferential concentration phenomenon. A *Voronoi diagram* is the unique decomposition of n-dimensional space into cells associated to each particle. Each *Voronoi cell* is defined as the ensemble of points that are closer to a particular particle than to any other. In the Voronoi diagrams, the area A of a Voronoi cell is the inverse of the local 2D-concentration of particles; therefore the investigation of the field of Voronoi areas is strictly equivalent to that of the local concentration field. The use of Voronoi diagrams is very classical in the study of granular systems, and has also been used to identify galaxy clusters. Usually, local concentration fields are obtained through a coarse-graining procedure over a minimal length scale, which has several disadvantages over Voronoi analysis. Box-counting methods are computationally inefficient, and they require selecting an arbitrary length scale, whereas in Voronoi analysis, no length scale is chosen a priori. For more details on Voronoi analysis, see [132].

Correlation dimension: The basic idea of measuring the tendency of particles to concentrate inhomogeneously in space comes from the theory of dissipative systems [138, 139]. This quantity was introduced to the field of preferential concentration by [140] and has since been used by many others [125, 141, 142].

The Grassberger–Procaccia (GP) algorithm [138] is used to estimate the

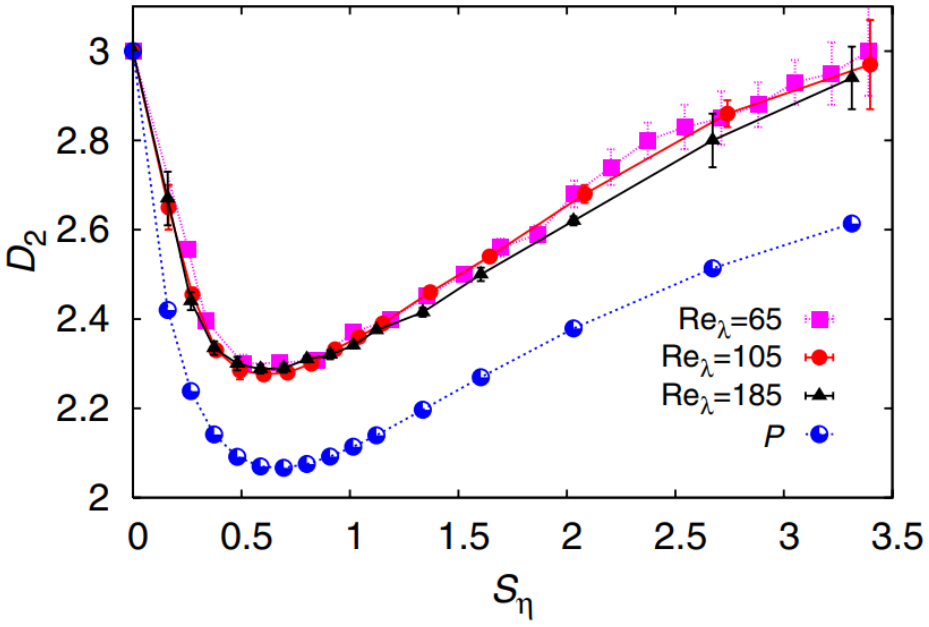

Figure 2.5: Numerical results of correlation dimension D_2 as a function of the Stokes number $S_\eta = \tau_p/\tau_\eta$, for three different Reynolds numbers Re_λ. Here, τ_η is the characteristic time of the small turbulent eddies and Re_λ is the Taylor-scale based Reynolds number. The blue dots show the probability P of finding particles in non-hyperbolic regions of the flow, for $Re_\lambda = 185$ (multiplied by an arbitrary factor for purposes of visualization). The source of the figure is [125].

correlation (fractal) dimension of a set of points. The main idea of this algorithm is to compute $C(r)$ the correlation sum:

$$C(r) = \frac{2}{N_p(N_p-1)} \sum_{i<j} \theta(r - |\boldsymbol{x}_i - \boldsymbol{x}_j|) \tag{2.12}$$

where N_p denotes the number of points $\boldsymbol{x}_1, \boldsymbol{x}_2, \ldots, \boldsymbol{x}_N$ in space, $|\boldsymbol{x}_i - \boldsymbol{x}_j|$ denotes the distance between any pair of points, and θ is the Heaviside step function. The fraction of pairs whose distance is smaller than r is then defined as $C(r)$. This sum is monotonically decreasing to zero as $r \to 0$. If $C(r)$ decreases according to a power law, $C(r) \sim r^{D_2}$, then the correlation dimension can be written in the form

$$D_2 = \lim_{r\to 0} \frac{\mathrm{d}\log C(r)}{\mathrm{d}\log r}. \tag{2.13}$$

The correlation dimension D_2 gives information about the distance from the random uniform distribution. Figure (2.5) shows the dependence of D_2 on the Stokes number in an incompressible isotropic and homogeneous 3D

turbulent flow, from numerical simulations [125]. More information on the correlation dimension can be found in [139].

The accurate calculation of D_2 is notoriously difficult because the value of the derivative $\frac{\mathrm{d}\log C(r)}{\mathrm{d}\log r}$ often converges very slowly for $r \to 0$, where the number of particle pairs is small. Also the lacunarity [143] of the fractal attractors causes $C(r)$ to oscillate. To overcome this problem, an alternative approach to studying clustering is to examine the link between the structure of the fractal attractor in phase space and the distribution of the particles in coordinate space.

Kaplan–Yorke dimension: In general, the fractal set in phase space is characterized by its fractal dimension D_F. It has been shown [144] that the fractal dimension of the projection of a set of dimension D_F onto a hyper-surface of dimension D (e.g. that of physical space) is D_F if $D_F < D$ and D if $D_F > D$. Therefore, if the fractal dimension of the attractor in $2D$ dimensional phase space is $D_F > D$, the distribution of particles in coordinate space will be space-filling. But if the fractal dimension of the attractor is smaller than D, D_F will provide us the dimension of the particle clusters.

Bec [36] has computed such a fractal dimension in numerical simulations of inertial particles in random smooth flows, which give clear indications that a consistent explanation of particle clustering can be addressed in terms of the properties of the attractors of particle dynamics. The fractal dimension of the attractor in phase space can be determined as the so-called Kaplan–Yorke dimension [145–147], defined as

$$D_{KY} = K + \frac{\sum_{i=1}^{K} \lambda_i}{|\lambda_{K+1}|} \tag{2.14}$$

where the λ_i are the Lyapunov exponents of the dynamical system Eq. (2.3). The Lyapunov exponents are ordered from the largest (most positive) to the smallest (most negative). It is a simple matter to count the maximum number K of exponents whose sum is positive, i.e. $\sum_{i=1}^{K} \lambda_i \geq 0$, and this number K is a lower bound on the dimension of the attractor. D_{KY} can be interpreted as the largest dimension of a set whose volume is left invariant by time evolution. It can be obtained by means of a linear interpolation of the sum of Lyapunov exponents between the two integer values for which neither expansion (positive sum) nor contraction (negative sum) occurs [144].

Segregation scale: When there are different types of particle (either different densities or different Stokes numbers) in the same flow (polydisper-

sity), the different types of particles exhibit different flow structures. For instance, light particles (e.g. air bubbles in water) preferentially concentrate in regions of high vorticity, whereas heavier ones (e.g. sand grains in water) are expelled by rotating regions. This leads to a segregation of the different particle types, which intuitively is characterized by some segregation length scale. Calzavarini and collaborators [37] have also provided a new indicator for the quantitative characterization of the segregation of inertial particles evolving in a turbulent flow. The indicator allows defining a segregation length scale r_{seg} between different classes of particles. The further details of this indicator are given in Section 4.5.

2.4.4 Large scale clustering: Turbophoretic aggregation

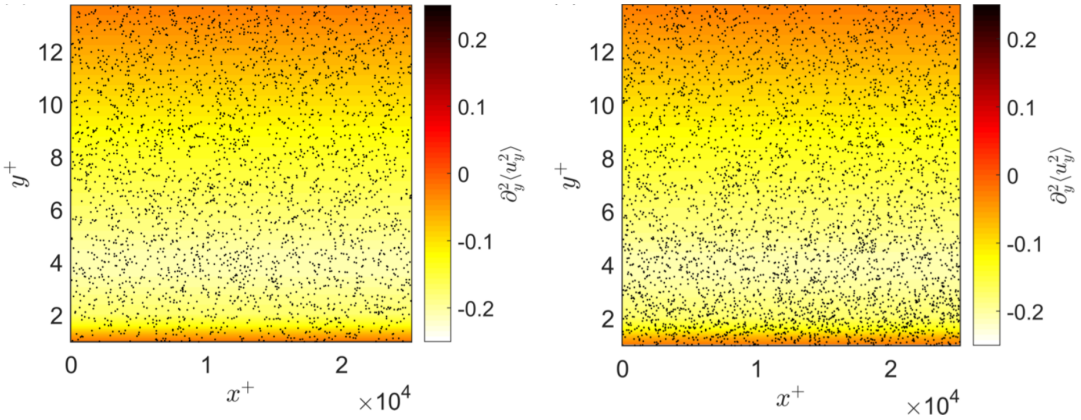

Figure 2.6: Comparison of the instantaneous particle distribution of (a) tracer particles, (b) inertial particles ($St = 0.1$) in the near-wall region. The particle distribution is plotted on top of the time-averaged $\partial_y^2\langle u_y^2\rangle$ field. The snapshots are taken from direct numerical simulations of a turbulent channel flow [148].

The computation of the correlation dimension and Lyapunov exponents to characterize preferential clustering in numerical simulations of elastic turbulent flows will be addressed in this thesis, in Chapter 4. Let us remark that these computations only provide information about the small scale properties of the particle distribution, while the large scale properties can be influenced in a nontrivial way by the structure of the flow. There are several types of large-scale particle accumulation mechanisms, which have

been studied not only in homogeneous turbulent flows but also inhomogeneous turbulent flows. Turbhophoresis is one of them, that is, the migration of particles due to fluctuations of the flow. In this section, we mainly focus on the phenomenology of turbophoresis and what is already known to us.

Small-scale clustering has also been observed in inhomogeneous flows [33], leading, together with turbophoresis, to the formation of streaky particle patterns [149]. In the one-way coupling regime [150] (i.e. when the solid phase has a negligible effect on the fluid phase) and mainly in wall-bounded flows, it has been shown that particles migrate from regions of high turbulence to regions of low turbulence [151–153]. A net flux of particles from a region of high turbulence intensity to a region of low turbulence intensity has been observed, and a quantitative description of turbophoresis was derived from the basic conservation equations of the fluid–particle system [153]. Using this approach, it is possible to show that one obtains the following expression for the turbophoretic velocity:

$$V_{p,turbo} = -\tau_p \frac{\mathrm{d}V_{py}^{'2}}{\mathrm{d}y} \tag{2.15}$$

where $V_{py}^{'2}$ is the particle mean-square velocity fluctuation. Importantly, the turbophoretic term depends on the particle mean-square velocity, which might be different from the corresponding fluid velocity if the particle inertia is large [154]. In the limit $\tau_p \to 0$ in Eq. (2.15) one has $V_{p,turbo} \to 0$. Turbophoresis is thus negligible for not very heavy particles even if there is a gradient in the fluid turbulence intensity. As τ_p increases, the turbophoretic velocity increases, thereby raising the possibility of migration in the direction opposite to the gradient of velocity fluctuations by a few orders of magnitude. However, as τ_p increases, the particles are less able to follow fluid fluctuations, and the difference between the particle and fluid root-mean-square velocities becomes progressively more significant. The turbophoretic velocity vanishes $(V_{p,turbo} = 0)$ for all particles, irrespective of their inertia, when the flow is either not turbulent or when the turbulence is homogeneous. This turbophoretic phenomenon has been shown to be stronger when the turbulent near-wall characteristic time and the particle characteristic time scale are similar [155].

In a channel flow [148], it has been observed that inertial particle migration due to turbophoresis changes the initially random distribution of the particles by driving particles toward the wall. A snapshot of the distribution of tracer and inertial particles in the $x - y$ plane near the wall shows qualitatively the increased concentration of inertial particles near the

wall (see Fig. 2.6). It is visible that the tracer particles shown in Fig. 2.6(a) are distributed randomly in space and appear uniformly distributed, while the inertial particles (Fig. 2.6(b)) accumulate near the wall. Turbophoresis has been mainly studied in wall-bounded flows, because of their relevance for industrial and environmental applications related to particle deposition [32, 148, 151, 156, 157].

Interestingly, using a three-dimensional (3D) Newtonian turbulent Kolmogorov flow, it was recently shown that turbophoretic segregation is independent of the presence of walls [34] (this was also confirmed in simulations employing a random inhomogeneous forcing [35]). Also in that case, particles accumulate in regions of minimum turbulent diffusivity, but the spatial distribution of the latter with respect to the mean flow differs from the one found in geometrically confined flows [34]. Large scale segregation in the context of elastic turbulence will be addressed in Chapter 5.

Chapter 3

Direct numerical simulations of elastic turbulence

Contents

3.1 Introduction

It is known that the presence of polymers can change the stability properties of laminar flows, due to purely elastic instabilities [158, 159]. A notable effect observed both experimentally and numerically is the onset of the so called elastic turbulence [160, 161] which, despite its name, occurs in the limit of very low Reynolds numbers, provided that the elasticity is large enough. In this regime, polymer solutions have features typical of turbulent flows (for instance, a broad range of active scales and an apparently

random character). Consequently, elastic turbulence has found important applications in microfluidics given the fact that it can create chaotic flows and strongly enhance mixing in the absence of fluid inertia (i.e. for vanishing Re) [6, 7, 18, 29, 162]. Despite its broad technological interest, elastic turbulence is still quite poorly understood from a theoretical point of view; there are some predictions based on simplified dynamical equations and constitutive laws for visco-elastic fluids [86, 88, 163].

In this chapter, I will present numerical results on the direct numerical simulation of a visco-elastic Kolmogorov flow in two dimensions at low Reynolds numbers. As will be seen, the basic phenomenology observed in laboratory experiments is reproduced using the simple geometrical setup and adopting the Oldroyd-B model to account for visco-elasticity.

3.2 Problem formulation and numerical method

3.2.1 Governing equations

We consider the dynamics of a dilute polymer solution as described by the visco-elastic Oldroyd-B model (Eq. (1.7) and Eq. (1.13), recalled below):

$$\partial_t \boldsymbol{u} + (\boldsymbol{u}\cdot\boldsymbol{\nabla})\boldsymbol{u} = -\frac{\boldsymbol{\nabla} p}{\rho_f} + \nu_s \Delta \boldsymbol{u} + \frac{2\eta\nu_s}{\tau}\boldsymbol{\nabla}\cdot\boldsymbol{\sigma} + \boldsymbol{f}, \tag{3.1}$$

$$\partial_t \boldsymbol{\sigma} + (\boldsymbol{u}\cdot\boldsymbol{\nabla})\boldsymbol{\sigma} = (\boldsymbol{\nabla}\boldsymbol{u})^T\cdot\boldsymbol{\sigma} + \boldsymbol{\sigma}\cdot(\boldsymbol{\nabla}\boldsymbol{u}) - 2\frac{\boldsymbol{\sigma}-\mathbf{1}}{\tau}. \tag{3.2}$$

In the above equations, $\boldsymbol{u}$ is the incompressible velocity field, the symmetric positive definite matrix $\boldsymbol{\sigma}$ represents the normalized conformation tensor of the polymer molecules, and $\mathbf{1}$ is the unit tensor corresponding to the equilibrium configuration of the polymers attained in the absence of flow ($\boldsymbol{u}=0$). The trace $tr\,(\boldsymbol{\sigma})$ gives the local polymer (square) elongation and τ is the largest polymer relaxation time. The fluid density is denoted by ρ_f and the total viscosity of the solution is $\nu = \nu_s(1+\eta)$, with ν_s the kinematic viscosity of the solvent and η the zero-shear contribution of the polymer (which is proportional to the concentration of the polymer). The extra stress term $\frac{2\eta\nu_s}{\tau}\boldsymbol{\nabla}\cdot\boldsymbol{\sigma}$ takes into accounts elastic forces providing a feedback mechanism on the flow, which can lead to flow destabilization even in the limit $Re \to 0$.

3.2.2 Kolmogorov flow

As we are interested to study the bulk properties of the flow, we limit the present study to the configuration of periodic Kolmogorov flow [164]. Such

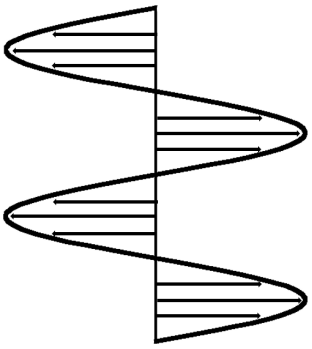

Figure 3.1: The Kolmogorov flow profile.

a complications are not only numerical in character but also concern the modeling aspect of the proper expression to be adopted for the conformation tensor on solid walls. The Kolmogorov flow, introduced by Kolmogorov around the 1960's [164], is a parallel flow with sinusoidal profile (Fig. 3.1) as a model to study the transition to turbulence in Newtonian fluids. This flow can be realized physically under laboratory conditions by means of magneto-hydrodynamic drive [165]. An advantage of using Kolmogorov flow to investigate elastic turbulence is that its stability properties are known for both the Newtonian [166] and the visco-elastic case [161]. The Kolmogorov flow is obtained by imposing a forcing in the x direction (the horizontal one), sinusoidally in the y direction (a transversal one) which results in a sinusoidal velocity profile (see Fig. 3.1).

The two-dimensional (2D) Oldroyd-B model with Kolmogorov forcing has been previously shown [90–92] to provide an effective theoretical framework to reproduce the basic phenomenology of elastic turbulence. Using the Kolmogorov forcing $\boldsymbol{f} = (F\cos(y/L), 0)$ in Eq. (3.1), there is a laminar fixed point, i.e. a stationary solution, corresponding to the velocity field and the conformation tensor components respectively:

$$\boldsymbol{u}^{(0)} = (U_0\cos(y/L), 0) \tag{3.3}$$

$$\sigma_{11}^{(0)} = 1 + \frac{\tau^2 U_0^2}{2L^2}\sin^2(y/L) \tag{3.4}$$

$$\sigma_{12}^{(0)} = \sigma_{21}^{(0)} = -\frac{\tau U_0}{2L}\sin(y/L) \tag{3.5}$$

$$\sigma_{22}^{(0)} = 1 \tag{3.6}$$

with $F = \nu U_0/L^2$ [161]. From these expressions, characteristic length and velocity scales L and U_0, respectively, can be identified. In the elastic tur-

bulence regime, the mean velocity and conformation tensor fields maintain similar trigonometric functional forms but with different amplitudes ([90, 92], see also Section 3.4.2). Writing U for the mean velocity amplitude in such states, we define the Reynolds number as $Re = UL/\nu$ and the Weissenberg number as $Wi = U\tau/L$. As previously documented, the laminar flow becomes unstable [161] for sufficiently high values of the elasticity, even in the absence of fluid inertia, and eventually has features typical of turbulent flows [90–92].

3.2.2.1 Elastic instabilities

Let us briefly recall here the main results about the linear stability of the Oldroyd-B Kolmogorov flow (for more details see [161]). The considered flow is unstable to large-scale perturbations, i.e. with wavelengths much larger than L. In the Newtonian case, the instability arises at $Re_c = \sqrt{2}$ [166]. For the visco-elastic (Oldroyd-B) case, analytical and numerical investigations have found the complete stability diagram in the $Re - Wi$ plane [161] (see Fig. 3.2). For $Wi = 0$, the Newtonian value $Re_c = \sqrt{2}$ above which the flow is linearly unstable is recovered and the curve of the diagram starting at $Re = \sqrt{2}$ in the region $Wi \sim 0$ defines the region of inertial instabilities. A significant difference is observed in that the critical value above which the flow is unstable is increased, i.e. for a given small Wi the critical Re_c is larger than $\sqrt{2}$. However, in the right-hand side of Fig. 3.2 the instabilities are generated for $Re < \sqrt{2}$ and for large Wi and are known as elastic instabilities. Further, the analytical calculations are validated with numerical results (black triangles in Fig. 3.2).

As can be seen from Fig. 3.2, for sufficiently large elasticity (i.e. large values of Wi), the Kolmogorov flow can be unstable even at vanishing Reynolds numbers. The existence of such purely elastic instabilities suggests the possibility of exciting some turbulent-like flow resembling elastic turbulence, provided Re is small enough and Wi is larger than a threshold value of order $1 - 10$.

3.2.3 Numerical method

The numerical integration of visco-elastic models is a challenging task since it is necessary to solve at the same time the Navier–Stokes equation with an extra stress term and the equation for the components of the conformation tensor. Moreover, the linear visco-elastic Oldroyd-B model allows for in-

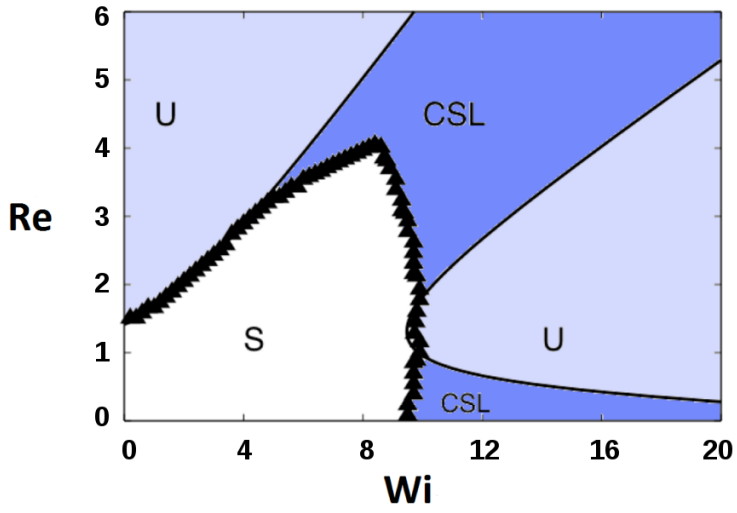

Figure 3.2: Linear stability diagram of the visco-elastic Kolmogorov flow, as predicted by multi-scale analysis (solid lines) and computed by the numerical solution of the exact linearized equations (triangles) in the plane $Re-Wi$. Different regions are observed: at small Weissenberg number $Wi = \frac{U\tau}{L}$ the critical Reynolds number Re_c increases for increasing Wi, *i.e.* polymers have a stabilizing effect; at large enough Wi, Re_c decreases, *i.e.* instabilities are driven by the polymer-flow interaction (elastic turbulence). In the region denoted by U the flow is unstable, in that denoted by S it is stable. Inside the area denoted by CSL the flow is stable with respect to large-scale perturbations, but unstable with respect to generic perturbations. The figure is adapted from Ref. [161].

finite polymer elongation, and consequently, the stretching exerted by the velocity gradients can generate singularities in the conformation tensor. Indeed, the eigenvectors of the conformation tensor tend to align in the directions of the Lyapunov vectors, and the eigenvalues can experience exponential growth, leading to the formation of sharp fronts of polymer quantities with diverging gradients which are involved in the feedback on the velocity field. The consequence is a sudden occurrence of numerical instabilities, also known as Hadamard instabilities [167], in the simulations, which can blow up after a short time.

These instabilities are associated with the loss of positive definiteness of the conformation tensor and become particularly important at high elasticity, thus limiting the possibility of investigating the elastic turbulent regime by direct implementation of Eq. (3.1) and Eq. (3.2). To overcome this prob-

lem, we use an algorithm based on a Cholesky decomposition of the conformation matrix that ensures the symmetry and positive definiteness of $\boldsymbol{\sigma}$, implemented earlier in [90, 168]. This consists in writing $\boldsymbol{\sigma}$ as the product of a lower triangular matrix with its transpose:

$$\boldsymbol{\sigma} = \boldsymbol{L}\boldsymbol{L}^T \tag{3.7}$$

where $\boldsymbol{L} = \begin{bmatrix} l_{11} & 0 \\ l_{21} & l_{22} \end{bmatrix}$, and in deriving a transport equation for the tensor $\boldsymbol{L}$. In the equations of motion for the three non-zero elements of $\boldsymbol{L}$ can be derived from those for the elements of $\boldsymbol{\sigma}$ sequentially, starting with $l_{11} = \sqrt{\sigma_{11}}$ and then proceeding to $l_{21} = \sigma_{12}/\sqrt{\sigma_{11}}$ and $l_{22} = \sqrt{\sigma_{22} - \sigma_{12}^2/\sigma_{11}}$ [168]:

$$\dot{l}_{11} = \gamma_{11} l_{11} + \gamma_{21} l_{21} - \frac{1}{\tau}\left(l_{11} - \frac{1}{l_{11}}\right) \tag{3.8}$$

$$\dot{l}_{21} = \gamma_{12} l_{11} + \gamma_{22} l_{21} + \gamma_{21}\frac{l_{22}^2}{l_{11}} - \frac{1}{\tau}\left(l_{21} + \frac{l_{21}}{l_{11}^2}\right) \tag{3.9}$$

$$\dot{l}_{22} = \gamma_{22} l_{22} - \gamma_{21}\frac{l_{21} l_{22}}{l_{11}} - \frac{1}{\tau}\left(l_{22} - \frac{1}{l_{22}} - \frac{l_{21}^2}{l_{11}^2 l_{22}}\right) \tag{3.10}$$

where γ_{ij} are the elements of the velocity gradient tensor. The matrix $\boldsymbol{\sigma}$ will remain positive definite as long as the diagonal components of $\boldsymbol{L}$ are greater than zero. A way to satisfy this constraint is to implement a logarithmic transformation of the diagonal elements:

$$\tilde{l}_{11} = \log\left(l_{11}\right) \quad \rightarrow l_{11} = e^{\tilde{l}_{11}} \tag{3.11}$$

$$\tilde{l}_{21} = l_{21} \quad \rightarrow l_{21} = \tilde{l}_{21} \tag{3.12}$$

$$\tilde{l}_{22} = \log\left(l_{22}\right) \quad \rightarrow l_{22} = e^{\tilde{l}_{22}}. \tag{3.13}$$

Exponentiation, after numerical integration of $\tilde{l}_{ij}$, ensures positive diagonal elements. The equations for $\tilde{l}_{11}$, $\tilde{l}_{12}$ and $\tilde{l}_{22}$ are found by the chain rule for derivatives. The resulting equations for $\tilde{l}_{ij}$ are

$$\dot{\tilde{l}}_{11} = \gamma_{11} + \gamma_{21}\tilde{l}_{21}e^{-\tilde{l}_{11}} + \frac{1}{\tau}\left(-1 + e^{-2\tilde{l}_{11}}\right) \tag{3.14}$$

$$\dot{\tilde{l}}_{21} = \gamma_{12}e^{\tilde{l}_{11}} + \gamma_{22}\tilde{l}_{21} + \gamma_{21}e^{2\tilde{l}_{22}-\tilde{l}_{11}} - \frac{1}{\tau}\tilde{l}_{21}\left(1 + e^{-2\tilde{l}_{11}}\right) \tag{3.15}$$

$$\dot{\tilde{l}}_{22} = \gamma_{22} - \gamma_{21}\tilde{l}_{21}e^{-\tilde{l}_{11}} + \frac{1}{\tau}\left(-1 + e^{-2\tilde{l}_{22}} + \tilde{l}_{21}^2 e^{-2\left(\tilde{l}_{11}+\tilde{l}_{22}\right)}\right) \tag{3.16}$$

3.2.3.1 Artificial polymer diffusivity: The Schmidt number

Equations (3.14), (3.15) and (3.16) preserve the symmetric positive definite (SPD) nature of the conformation tensor $\boldsymbol{\sigma}$: its eigenvalues remain positive by construction. Another critical aspect is the fact that since the smallest eigenvalue can become arbitrarily close to zero, infinitesimal errors arising from the integration scheme can bring it below zero, producing a new source of numerical instabilities.

As a cure to the problem of these instabilities, Beris *et al.* [167, 169, 170] introduced an artificial polymer diffusivity, i.e. a Laplacian term $D_p\Delta\boldsymbol{\sigma}$ into the equation of motion for $\boldsymbol{\sigma}$, where D_p is a space-independent coefficient, that can be chosen so that it stabilizes the numerics and to have a negligible influence on the results. The importance of such a diffusive term for viscous dissipation is quantified by the non-dimensional parameter known as the Schmidt number:

$$Sc = \frac{\nu_s}{D_p}. \tag{3.17}$$

For computational reasons, we decided to add diffusivity to the equations for the l_{ij} fields. In terms of the $\tilde{l}_{ij}$ fields, i.e. those that are actually updated by the numerical method, this choice implies the appearance of square gradient terms in the equations for the diagonal elements, due to the exponential transformation. The resulting extra terms that then need to be added are summarized by the following relations:

$$\begin{aligned} D\Delta l_{11} &= D\left(\partial_x^2 + \partial_y^2\right) e^{\tilde{l}_{11}} \\ \implies De^{\tilde{l}_{11}}&\left[\left(\partial_x^2\tilde{l}_{11}\right) + \left(\partial_x\tilde{l}_{11}\right)^2 + \left(\partial_y^2\tilde{l}_{11}\right) + \left(\partial_y\tilde{l}_{11}\right)^2\right] \\ D\Delta l_{11} &= De^{\tilde{l}_{11}}\left(\left|\nabla\tilde{l}_{11}\right|^2 + \Delta\tilde{l}_{11}\right) \end{aligned} \tag{3.18}$$

$$D\Delta l_{12} = D\Delta\tilde{l}_{12} \tag{3.19}$$

$$D\Delta l_{22} = De^{\tilde{l}_{22}}\left(\left|\nabla\tilde{l}_{22}\right|^2 + \Delta\tilde{l}_{22}\right). \tag{3.20}$$

On substituting the above relations into Eqs (3.14), (3.15) and (3.16), the evolution equations for $\tilde{l}_{ij}$ become

$$\dot{\tilde{l}}_{11} = \gamma_{11} + \gamma_{21}\tilde{l}_{21}e^{-\tilde{l}_{11}} + \frac{1}{\tau}\left(-1 + e^{-2\tilde{l}_{11}}\right) + D\left|\nabla\tilde{l}_{11}\right|^2 + D\Delta\tilde{l}_{11} \tag{3.21}$$

$$\dot{\tilde{l}}_{21} = \gamma_{12}e^{\tilde{l}_{11}} + \gamma_{22}\tilde{l}_{21} + \gamma_{21}e^{2\tilde{l}_{22}-\tilde{l}_{11}} - \frac{1}{\tau}\tilde{l}_{21}\left(1 + e^{-2\tilde{l}_{11}}\right) + D\Delta\tilde{l}_{21} \tag{3.22}$$

$$\dot{\tilde{l}}_{22} = \gamma_{22} - \gamma_{21}\tilde{l}_{21}e^{-\tilde{l}_{11}} + \frac{1}{\tau}\left(-1 + e^{-2\tilde{l}_{22}} + \tilde{l}_{21}^2 e^{-2\left(\tilde{l}_{11}+\tilde{l}_{22}\right)}\right) + D\left|\nabla\tilde{l}_{22}\right|^2 + D\Delta\tilde{l}_{22}. \tag{3.23}$$

We numerically verified that the value of the diffusion coefficient appearing in Eqs (3.21–3.23) and the actual polymer diffusivity involved in the $D_p\Delta\boldsymbol{\sigma}$ term do not differ considerably. Indeed, using the value $D = 10^{-3}\nu_s$ in Eqs (3.21—3.23) we obtain an effective Schmidt number, as defined in Eq. (3.17), $\nu_s/D_p = O(10^3)$. The details of the numerical computation of the effective polymer diffusivity acting on the σ_{ij} fields and the related estimation of the Schmidt number can be found in Section 3.3.2.1.

3.2.4 Control parameters

Here we recall the definitions of the Reynolds and Weissenberg numbers in terms of the flow variables:

$$Re = \frac{UL}{\nu_s(1+\eta)}, \tag{3.24}$$

$$Wi = \frac{\tau U}{L}. \tag{3.25}$$

We have numerically integrated the evolution equations for the vorticity ζ, which can be derived by taking the curl of Eq. (3.1) and for the conformation tensor $\boldsymbol{\sigma}$, Eq. (3.2) in a square domain of size $L_0 = 2\pi$ with doubly periodic boundary conditions, by means of a pseudo-spectral method, with second-order Runge–Kutta scheme with time step δt at different resolutions, ranging from 128^2 to 1024^2 spatial discretization points. The vorticity field in two dimensions has only one nonzero component, normal to the plane of velocity, which is related to the stream function $\zeta = -\Delta\psi$. We fix $Re_0 = 1$ (using the value of U_0 to obtain an *a priori* estimate of it), which is smaller than the critical value $\sqrt{2}$ of the Newtonian case, and we vary Wi in a range of values larger than a critical one $Wi_c \approx 10$ corresponding to the onset of purely elastic instabilities [171]. In all simulations, the other parameters of the visco-elastic dynamics are $U_0 = 4$, $L = 1/4$, $\nu_s = 0.769$, $\eta = 0.3$. The initial condition is obtained by adding a uniform random perturbation to the fixed point solution $\boldsymbol{u}^{(0)}$ (Eq. (3.3)), $\boldsymbol{\sigma}^{(0)}$ (Eqs (3.4—3.6)) and the system is evolved in time until a statistically steady state is reached.

3.3 Numerical validation tests

3.3.1 Spatial resolution

To resolve the sharp gradients that form in the polymer-stress tensor field, a high spatial resolution is needed. We have tested explicitly that the statistical properties we measure are more or less independent of the resolution (N) for ($N \geq 512$) we use for our DNS. Some initial qualitative indications are shown in Fig. 3.3 (a snapshot of the vorticity field) and Fig. 3.4 (a snapshot of the trace of the conformation tensor). The presence of numerical noise is noticeable for the snapshots of the vorticity field and the trace of the conformation tensor field for spatial resolutions $N \leq 256$. This granularity of the images is associated with scales that are not well resolved. To learn better the effect of the spatial resolution on the statistical quantities, we measured the spectrum of kinetic energy (KE) and of the trace of the conformation tensor at different resolutions N for a fixed value of Wi. The spectrum in Fig. 3.5 is calculated by averaging over several times in the statistically stationary state of the velocity field (Fig. 3.5(a)) and of the trace of the conformation tensor field (Fig. 3.5(b)). For small N, an accumulation of energy at large wavenumbers due to errors associated with unresolved small scales can be seen. As N increases, the spectrum smoothly decreases over a broader and broader range of wavenumbers. For a large enough resolution N ($N \geq 512$) it does not considerably depend on the spatial resolution. The choice of $N = 512$ for our simulations then represents a compromise between the need to resolve small spatial scales and the computational cost (increasing roughly as N^2).

3.3.2 Effects of artificial polymer diffusivity

The addition of an artificial diffusivity can have a substantial impact on the qualitative spatial and temporal properties of the flow. In a recent numerical study adopting a forcing that gives rise to a cellular flow structure [172], it was found that in the absence of artificial polymer diffusivity, the polymer stress is mainly located in the straining regions, whereas in the presence of diffusivity it spreads outside the strain regions. This may yield misleading results even with relatively high values of the Schmidt number. Therefore it is important to understand how artificial polymer diffusivity affects the numerical results. For this purpose, numerical computations have been carried out at fixed $Re = 0.702$, $Wi = 22.5$ at resolution $N = 512$ and vary-

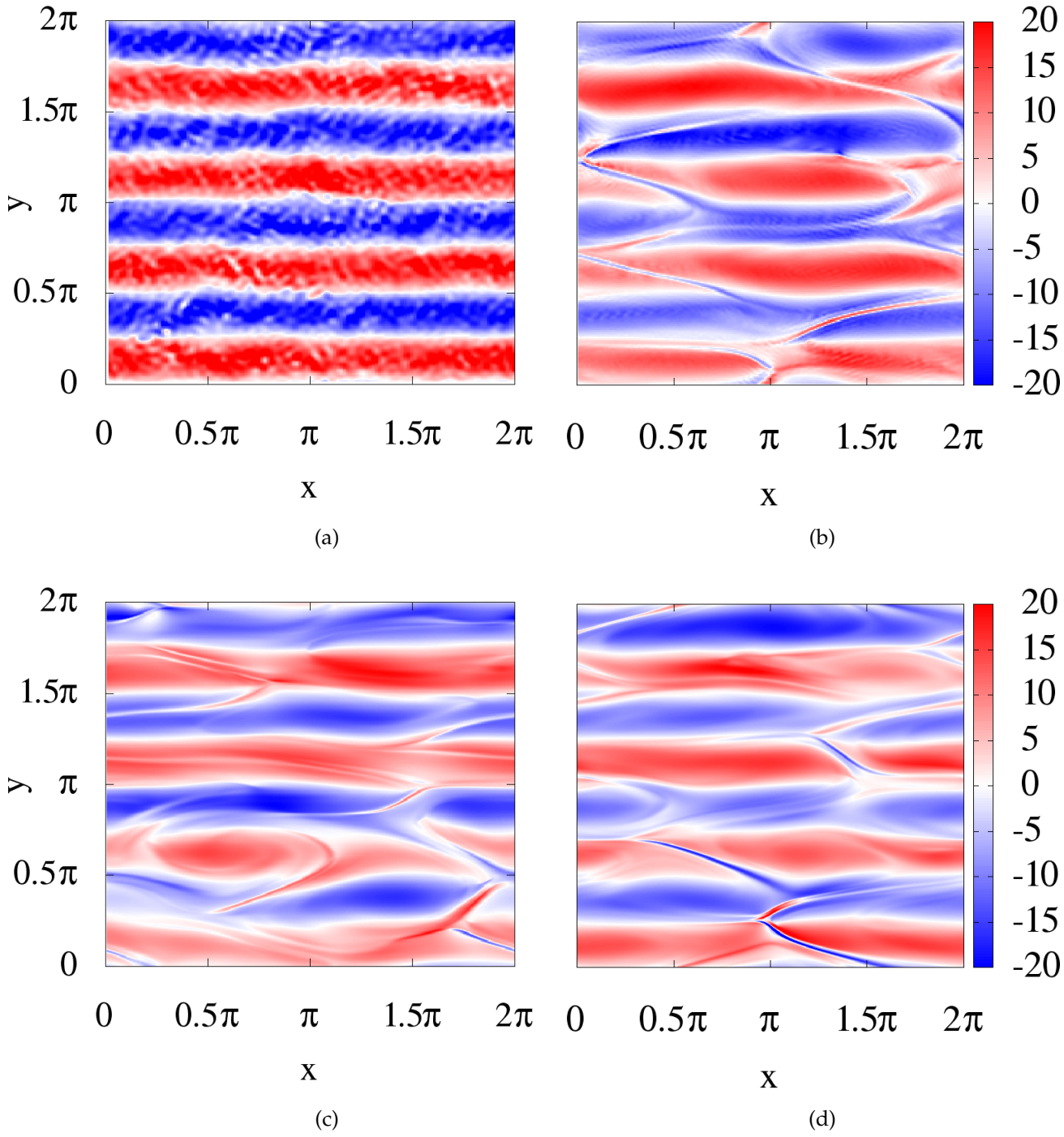

Figure 3.3: Snapshots of vorticity field at (a) $N = 128$; (b) $N = 256$; (c) $N = 512$; (d) $N = 1024$ for $Re = 0.702$ and $Wi = 22.5$.

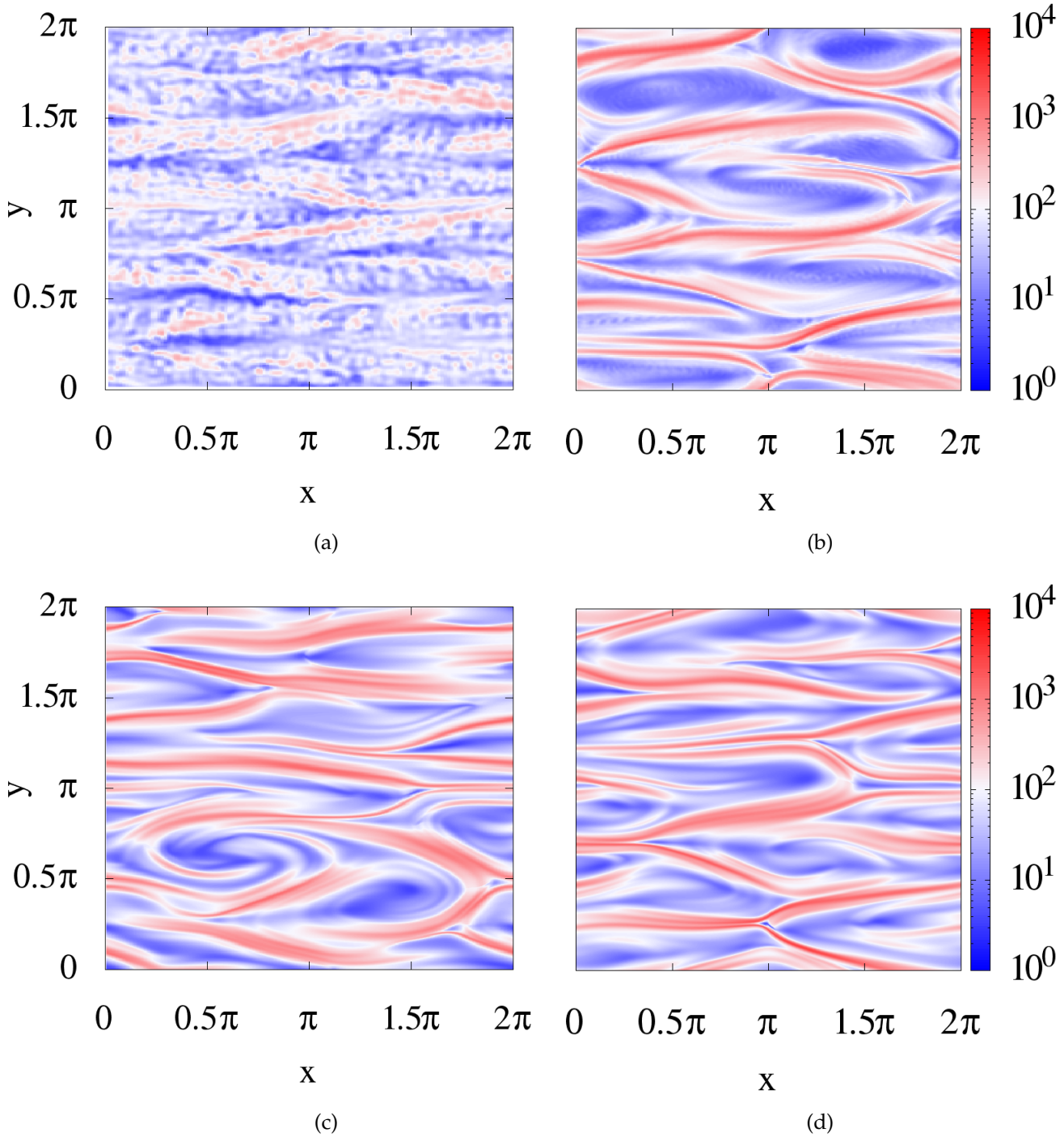

Figure 3.4: Snapshots of trace of the conformation tensor $tr(\boldsymbol{\sigma}) = \sigma_{11} + \sigma_{22}$ at (a) $N = 128$; (b) $N = 256$; (c) $N = 512$; (d) $N = 1024$ for $Re = 0.702$ and $Wi = 22.5$.

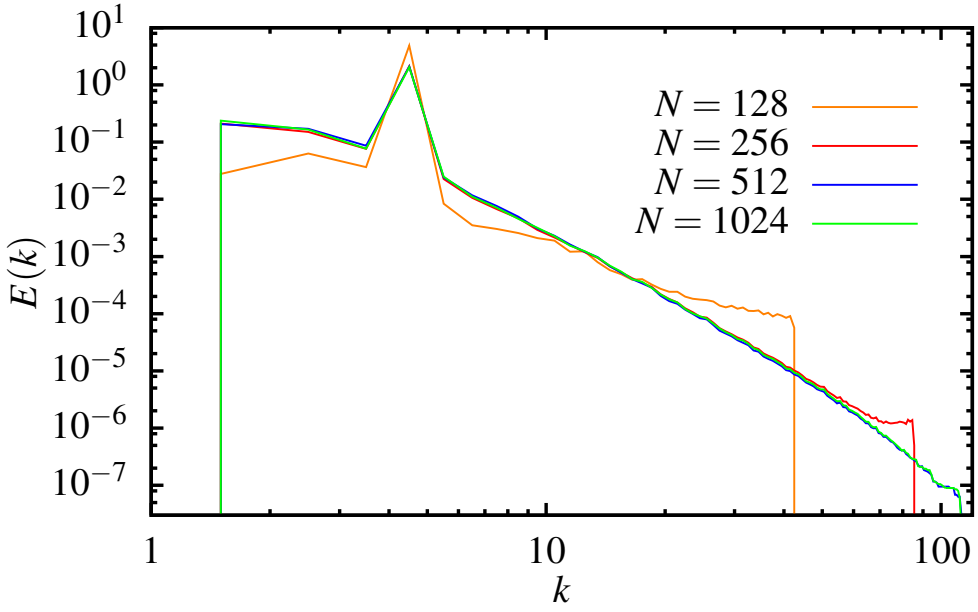

(a)

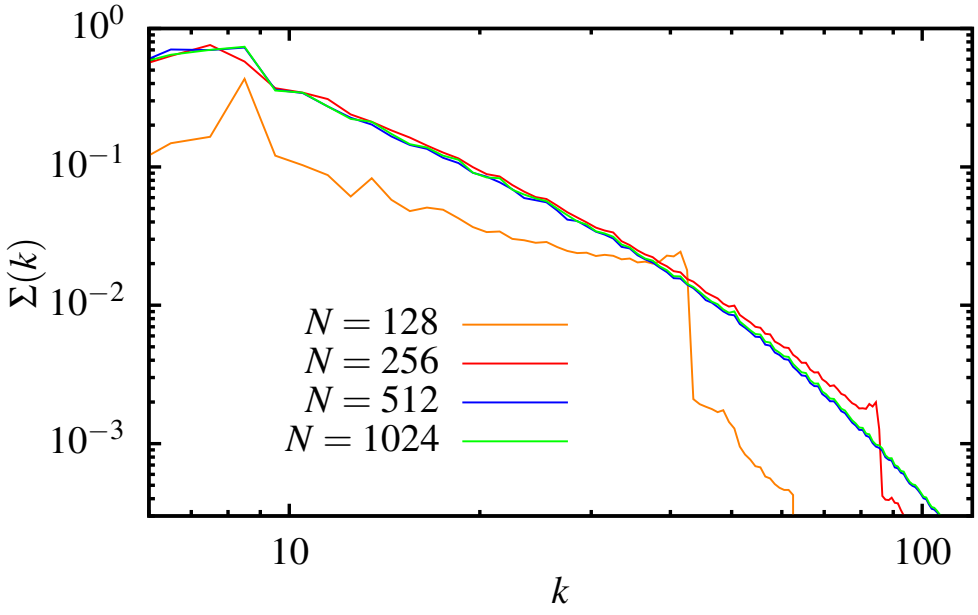

(b)

Figure 3.5: Comparison of spectra (a) of the velocity fluctuations $E(k)$ and (b) of the trace of the conformation tensor $\Sigma(k)$ from direct numerical simulation of elastic turbulence for $Re = 0.702$, $Wi = 22.5$ at resolutions $N = 128$; $N = 256$; $N = 512$ and $N = 1024$.

ing the 'polymeric' diffusivity such that the Schmidt number based on it is: $Sc = 10^3$, $Sc = 1250$, $Sc = 1667$, $Sc = 2500$, $Sc = 5000$ and $Sc = 10^4$. The smallest value of the Schmidt number is chosen to be $Sc = 10^3$, to compare with previous results [90].

To see the effect of artificial diffusivity, it is enough to observe the qualitative properties of the flow. Figure 3.6 compares the instantaneous snapshots of the vorticity field from the numerical results obtained using different Schmidt numbers. When Sc is increased, small intense gradients progressively appear in both the flow (see Fig. 3.6 for vorticity) and the polymer (see Fig. 3.7 for the trace of the polymer conformation tensor) fields. The latter fields then appear to be more noisy and numerical instabilities become less well controlled. This is particularly evident for $Sc = 10^4$ (but also visible for $Sc = 5000$, though to a lesser extent), while for $Sc = O(10^3)$) the fields appear smoother and more comparable with each other. We can also notice, however, that the filamentary structures associated with large polymer elongations tend to become thicker when Sc is decreased from 10^4 to 10^3.

The temporal behaviour of the kinetic energy for the different considered cases is shown in Fig. 3.8(a). It is here evident that it attains a definitely larger value when $Sc = 10^4$, a feature probably associated with the presence of numerous small spurious scales. The kinetic energy spectrum, shown in Fig. 3.8(b), allows accessing the scale-by-scale energy content. Its measure reveals that when $Sc \geq 5000$, energy piles up at the smallest scales, again in association with the presence of small unresolved scales. For smaller values of Sc, small differences between the different curves are still present at the highest wavenumbers but the spectra progressively tend to converge. This means simulations require even higher resolutions to resolve the small scales. From the present analysis we can conclude that for $Sc \leq 2500$ the numerical instabilities are reasonably well controlled, and the effect of artificial diffusivity is less dramatic than for higher values of Sc. Let us remark that this conclusion is flow-dependent and the effects on simulations forced in a different way, as in the case of cellular flows [172], may be different. This detailed study as a function of Sc motivates our choice of $Sc \approx 10^3$ as the numerical results appear to correspond to well resolved and physically sound simulations.

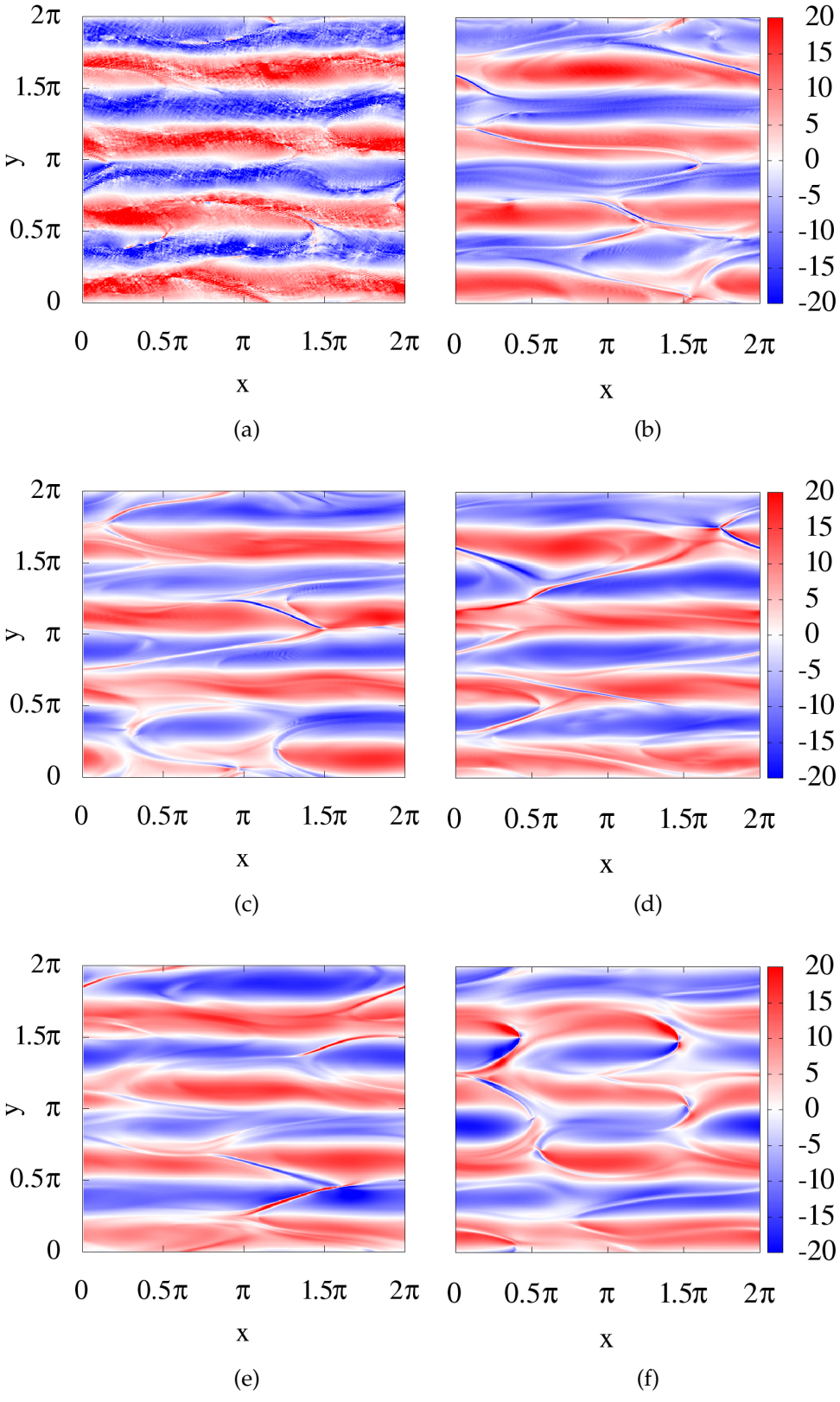

Figure 3.6: Snapshots of vorticity field at a resolution 512^2 (a) $Sc = 10000$; (b) $Sc = 5000$; (c) $Sc = 2500$; (d) $Sc = 1667$; (e) $Sc = 1250$; (f) $Sc = 1000$ for $Re = 0.702$ and $Wi = 22.5$.

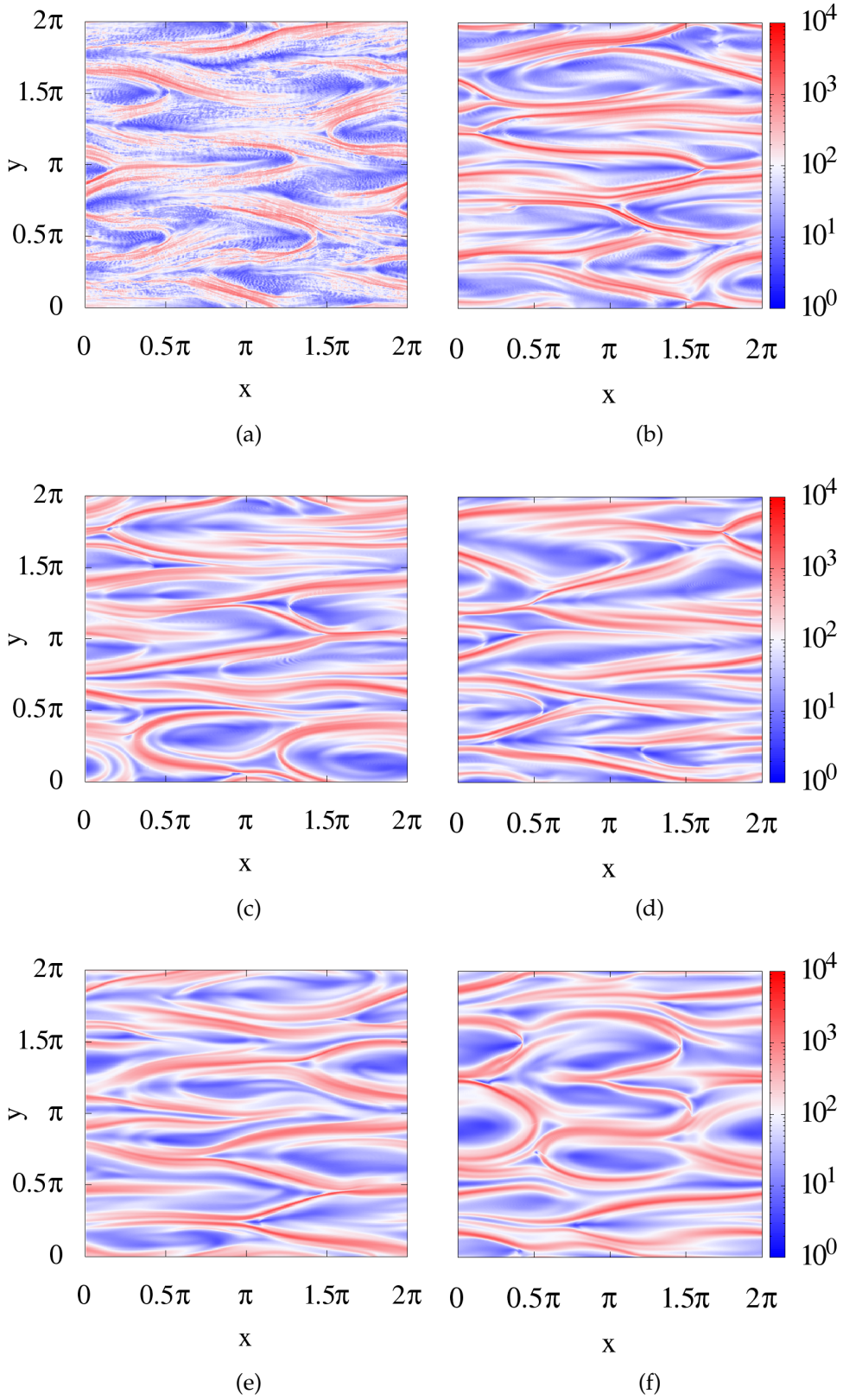

Figure 3.7: Snapshots of trace of the conformation tensor $tr(\boldsymbol{\sigma})$ at a resolution 512^2 (a) $Sc = 10000$; (b) $Sc = 5000$; (c) $Sc = 2500$; (d) $Sc = 1667$; (e) $Sc = 1250$; (f) $Sc = 1000$ for $Re = 0.702$ and $Wi = 22.5$.

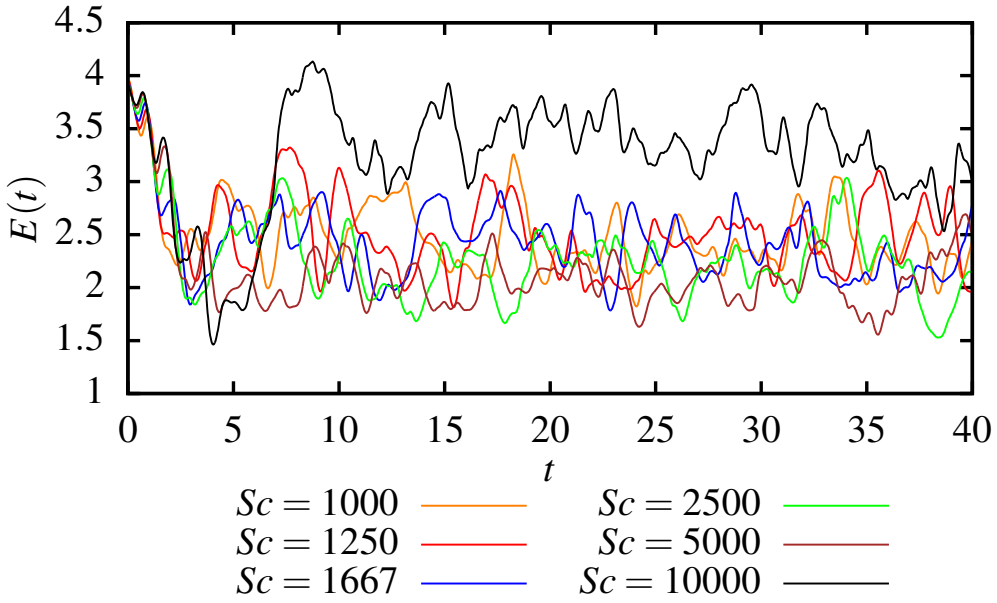

(a)

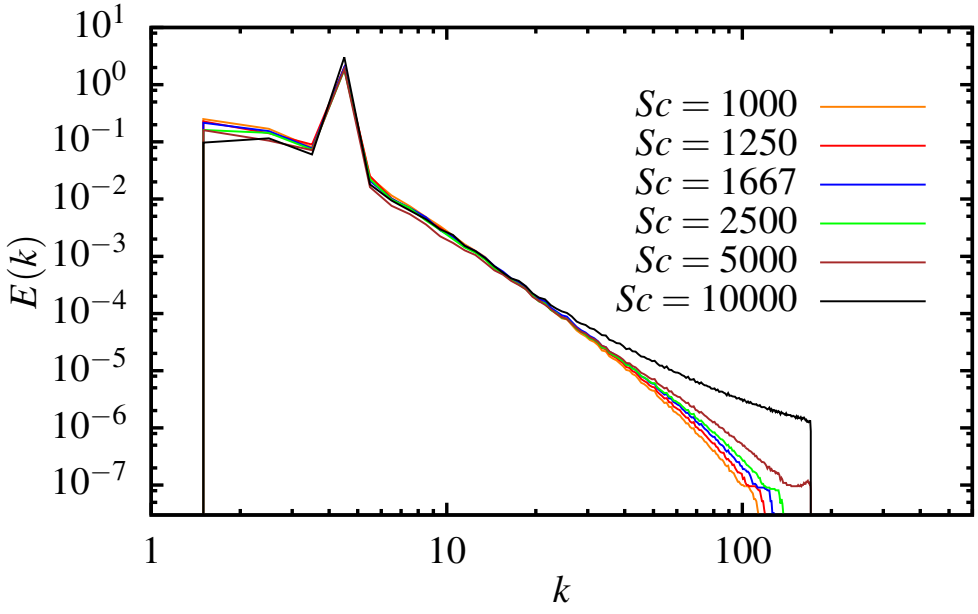

(b)

Figure 3.8: (a) Temporal behaviour of kinetic energy $E(t)$ and (b) kinetic energy spectrum $E(k)$ from direct numerical simulations at $Re = 0.702$, $Wi = 22.5$, $N = 512$ and different values of the artificial diffusivity D_{p^*} such that $Sc \equiv \nu_s/D_{p^*}$ varies between 10^3 and 10^4.

3.3.2.1 Numerical measurement of effective polymer diffusivity

As already discussed earlier, for numerical purposes we add an artificial diffusivity term $D_p\Delta\boldsymbol{\sigma}$ to the polymers. The implementation in the code of the polymer diffusion term is not directly related to $\boldsymbol{\sigma}$, but is in fact directly related to the $\tilde{l}_{ij}$ fields.

Therefore we expect that there will be an effective polymer diffusivity ($D_{p_{eff}}$) on $\boldsymbol{\sigma}$ resulting from the addition of a diffusivity to the l_{ij} fields, which might be different from D_p or of the same order ($D_{p_{eff}} \sim O(D_p)$).

Therefore it is interesting to study how does the effective polymer diffusion $D_{p_{eff}}$ differ from D_p. To achieve this we integrate the equations for σ_{ij} in the absence of forcing and feedback, starting from an initial condition corresponding to zero flow and sinusoidal conformation tensor components, as shown in the equations below,

$$\zeta^0 = 0 \tag{3.26}$$

$$\sigma^0_{11} = 1 + A_0 \sin(\frac{x}{L}) \tag{3.27}$$

$$\sigma^0_{12} = A_0 \sin(\frac{x}{L}) \tag{3.28}$$

$$\sigma^0_{22} = 1 + A_0 \sin(\frac{x}{L}) \tag{3.29}$$

where A_0 is the initial amplitude of the sinusoidal profile. For this case the value of D is kept fixed $\nu_s \times 10^{-3}$ in the code, which gives $Sc = 10^3$ (notice that this is not the one we defined, initially, as Sc in Eq. (3.17)).

In the absence of the flow, and no coupling between the flow and the polymers Eq. (3.2) reduces to the simplified equation:

$$\partial_t\boldsymbol{\sigma} = -2\frac{\boldsymbol{\sigma} - \mathbf{1}}{\tau} + D_{p_{eff}}\Delta\boldsymbol{\sigma} \tag{3.30}$$

On integrating Eq. (3.30), we obtain the following analytical solution for the components of $\boldsymbol{\sigma}$:

$$\sigma'_{11}(t) = \sigma_{11}(t) - 1 = A_0 \sin(\frac{x}{L}) e^{-\left(\frac{2}{\tau} + \frac{D_{p_{eff}}}{L^2}\right)t} \tag{3.31}$$

$$\sigma_{12}(t) = A_0 \sin(\frac{x}{L}) e^{-\left(\frac{2}{\tau} + \frac{D_{p_{eff}}}{L^2}\right)t} \tag{3.32}$$

$$\sigma'_{22}(t) = \sigma_{22}(t) - 1 = A_0 \sin(\frac{x}{L}) e^{-\left(\frac{2}{\tau} + \frac{D_{p_{eff}}}{L^2}\right)t} \tag{3.33}$$

By comparing the analytical solution Eqs (3.31—3.33) with the obtained numerical results for $\sigma'_{11}, \sigma_{12}, \sigma'_{22}$, we have extracted the value of amplitude

Wi	$D_{p_{eff}}(\sigma'_{11})$	$D_{p_{eff}}(\sigma_{12})$	$D_{p_{eff}}(\sigma'_{22})$	$Sc(\sigma'_{11})$	$Sc(\sigma_{12})$	$Sc(\sigma'_{22})$
19.1	0.000726	0.000741	0.000446	1058.76	1038.25	1723.31
22.5	0.000721	0.000737	0.000403	1066.39	1043.14	1906.25
23.9	0.000719	0.000736	0.000385	1069.58	1045.17	1996.42
24.9	0.000717	0.000734	0.000369	1996.41	1046.97	2086.02

Table 3.1: Measurement of effective polymer diffusivity $D_{p_{eff}}$ for all the components of $\boldsymbol{\sigma}$ and for different Wi and $Sc = \nu_s/D_{p_{eff}}$ is the estimated effective Schmidt number. Here the wavenumber is $k = 4$. The measurement clearly shows that the effective polymer diffusion $D_{p_{eff}} \sim O(D_p)$.

$A(t) = A_0 e^{-\left(\frac{2}{\tau}+\frac{D_{p_{eff}}}{L^2}\right)t}$ of the $\sin(x/L)$ profiles, shown in (Fig. 3.9) (red line). The amplitude $A(t)$ of the $\boldsymbol{\sigma}$ fields decays exponentially with given initial amplitude A_0 and polymer diffusion fitting constant $D_{p_{eff}}$. Further, the diffusion constant $D_{p_{eff}}$ is obtained by making a fit of $A(t)$ for $\sigma'_{11}, \sigma_{12}, \sigma'_{22}$ with their analogous analytical solutions, shown in (Fig. 3.9) (black dashed line). The estimated values of $D_{p_{eff}}$ for the different components of $\boldsymbol{\sigma}$ are summarized in Table 3.1.

3.4 Numerical results for two-dimensional elastic turbulence

3.4.1 Eulerian characterization of a 2D elastic turbulent Kolmogorov flow

The transition from laminar states to elastic turbulence of the system specified by Eqs (3.1) and (3.2) was previously studied in detail in [92]. Note that in the elastic turbulence regime the mean flow amplitude turns out to be decreased $(U < U_0)$ (this will be shown in one of the following sections), and in the following Re and Wi will be defined using the *a posteriori* measured value U. Here, we are interested in working in the regime corresponding to Weissenberg numbers well above the threshold value Wi_c. We recall that numerically it is found to be close to 10 ([90, 92]) not far from the value predicted by the linear stability analysis (Section 3.2.2.1)); the highest Wi that we can 'safely reach' considering the previous discussions about numerical issues in the present conditions is $Wi \approx 25$. For such values of Wi the flow develops temporally and spatially irregular fluctuations associated

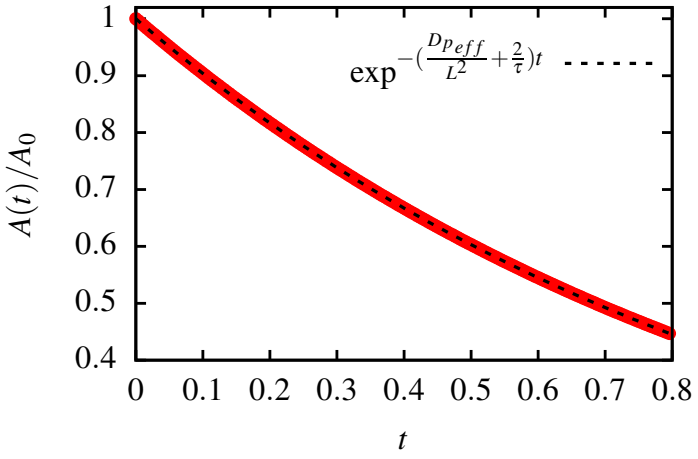

(a)

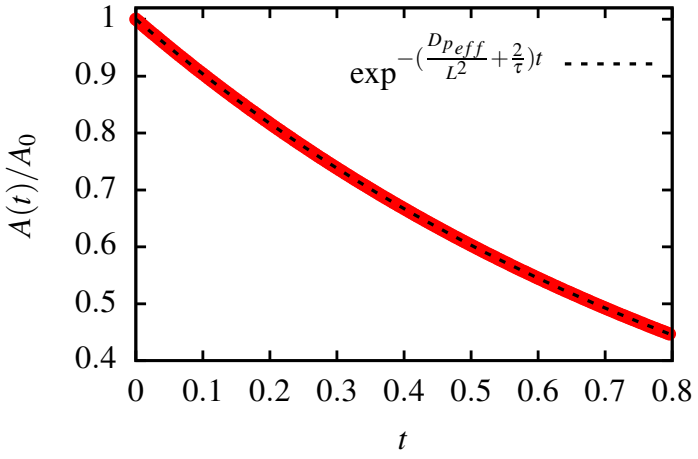

(b)

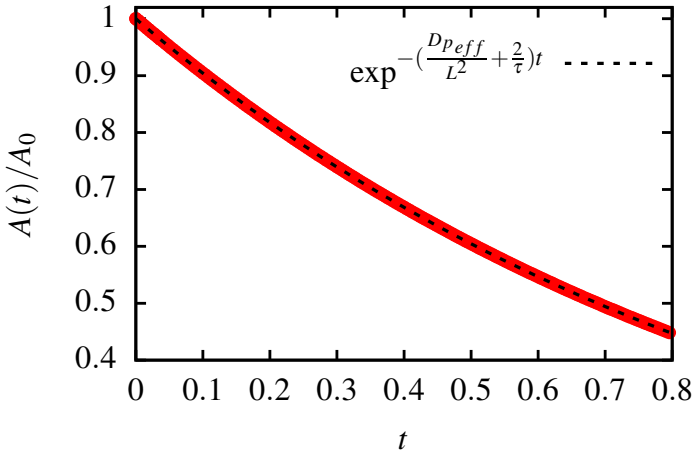

(c)

Figure 3.9: Estimation of $D_{p_{eff}}$ from the exponential decay of $A(t)/A_0$ as a function of time by making a fit with an exponentially decaying function, $D_{p_{eff}}$ is a fitting parameter (a) σ'_{11}; (b) σ_{12} (a) σ'_{22} components. Here $Wi = 22.5$.

with the chaotic and mixing dynamics reminiscent of turbulence. In order to get more insight into the elastic turbulent flow, in Fig. 3.11 we present two snapshots of the two-dimensional flow vorticity field at two different Weissenberg numbers Wi.

The first simulation at $Wi = 19.1$ is above the elastic instability threshold. The flow in this regime is unstable but still not very turbulent. A striking feature is that there are highly elastic filaments, propagating along the direction of the mean flow (see Fig. 3.10), associated with the stretching of the polymers by the largest gradients of the mean velocity field [92]. Similar wavy patterns also characterize the vorticity field $\zeta(x, y) = \partial_x u_y - \partial_y u_x$ (see Fig. 3.11), due to the coupling between the polymer dynamics and the velocity dynamics. At higher values of the elasticity, these vorticity patterns become progressively more erratic, carrying out a chaotic motion. At $Wi = 24.9$ we observe a considerably more irregular vorticity field. This is the regime of elastic turbulence, in which the flow develops active modes over a broad range of scales.

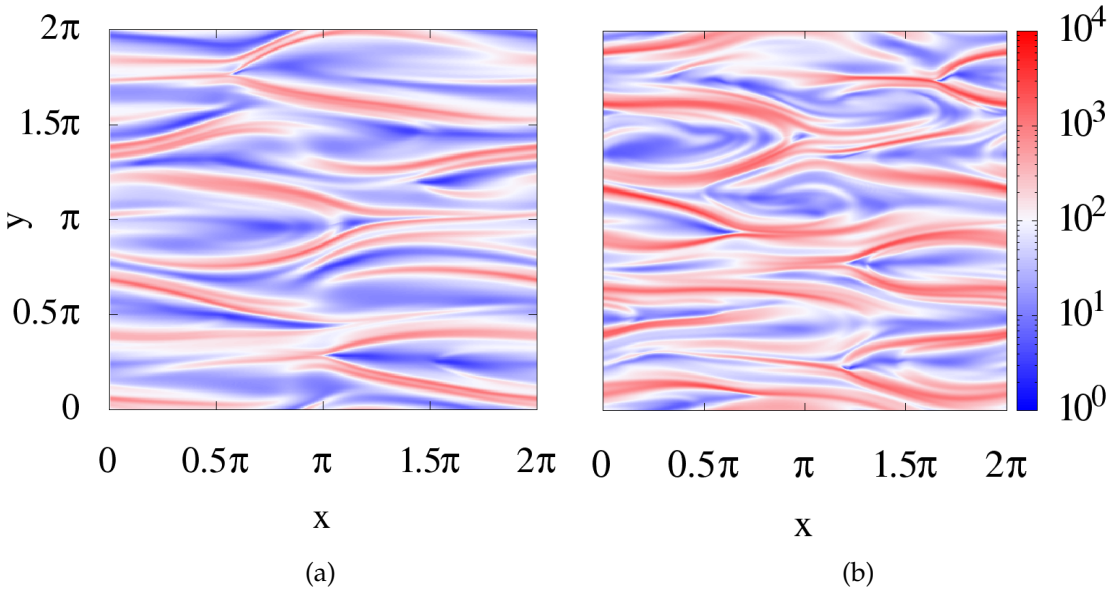

Figure 3.10: Snapshots of trace of the conformation tensor $tr(\boldsymbol{\sigma})$ at $Wi = 19.1$ (left) and $Wi = 24.9$ (right).

From a statistical point of view, these turbulent-like features are described by the spectrum of kinetic energy $E(k)$ and the specturm of the polymer elongation, which is proportional to that of elastic energy and is given by the trace of the conformation tensor $\Sigma(k)$ at wavenumber k. For

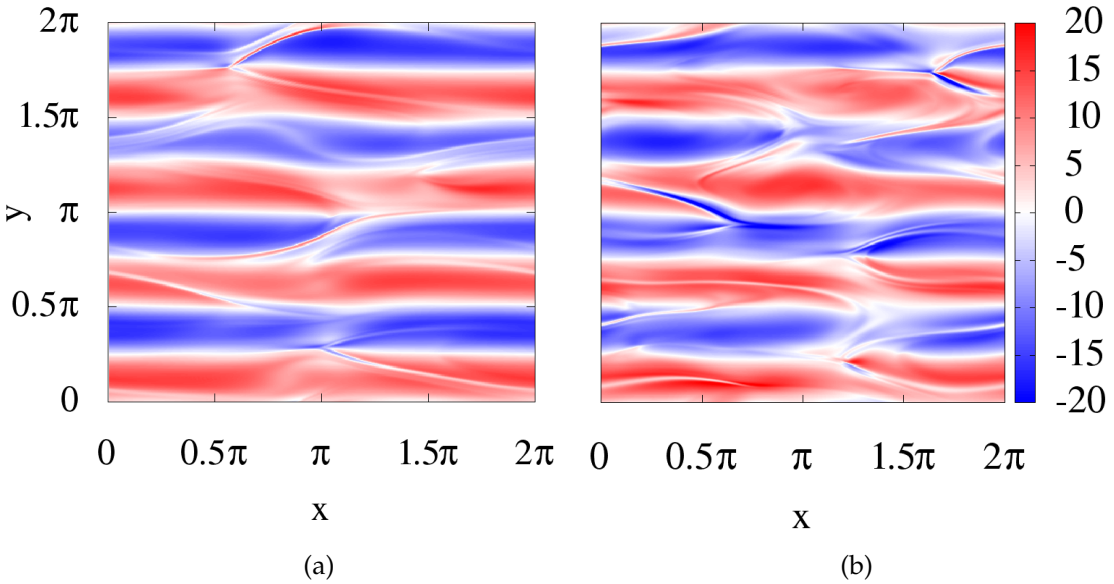

Figure 3.11: Snapshots of vorticity field at $Wi = 19.1$ (left) and $Wi = 24.9$ (right).

both quantities we find power-law behaviour as $E(k) \sim k^{-\gamma}$ (Fig. 3.12(a)) and $\Sigma(k) \sim k^{-\delta}$ (Fig. 3.12(b)), indicating a whole range of active scales. The kinetic energy spectrum is characterized by an exponent $3.5 < \gamma < 3.6$ larger than 3, pointing to a smooth flow, and in reasonable agreement with the value measured in (three-dimensional) experiments (see, e.g. [21]) and with theoretical predictions [173] based on an uniaxial model corresponding to the large polymer elongation limit of the Oldroyd-B model. The spectral exponent of $\Sigma(k)$ is found to be $\delta \approx 2$, similar to what is observed in numerical simulations of visco-elastic turbulence at higher Re (and with finite extensibility models of the polymer dynamics) [174, 175], and roughly in agreement with experimental results [176].

In the insets of Fig. 3.12, we show the behaviour of global quantities, namely the (temporally and spatially averaged) kinetic energy $E = \overline{|\boldsymbol{u}|^2}/2$ and the (temporally and spatially averaged) trace of the conformation tensor $\Sigma = \overline{tr(\boldsymbol{\sigma})}$, normalized by their laminar values $E_{LAM} = U_0^2/4$ and $\Sigma_{LAM} = 2 + Wi^2/4$, as functions of the Weissenberg number. Here, $\overline{(...)}$ represents an average over spatial coordinates and time:

$$\overline{(...)} = \frac{1}{TL_0^2} \int_0^T dt \int_0^{L_0} dy \int_0^{L_0} dx (...). \tag{3.34}$$

In agreement with previous observations [90, 92], we find that while the ki-

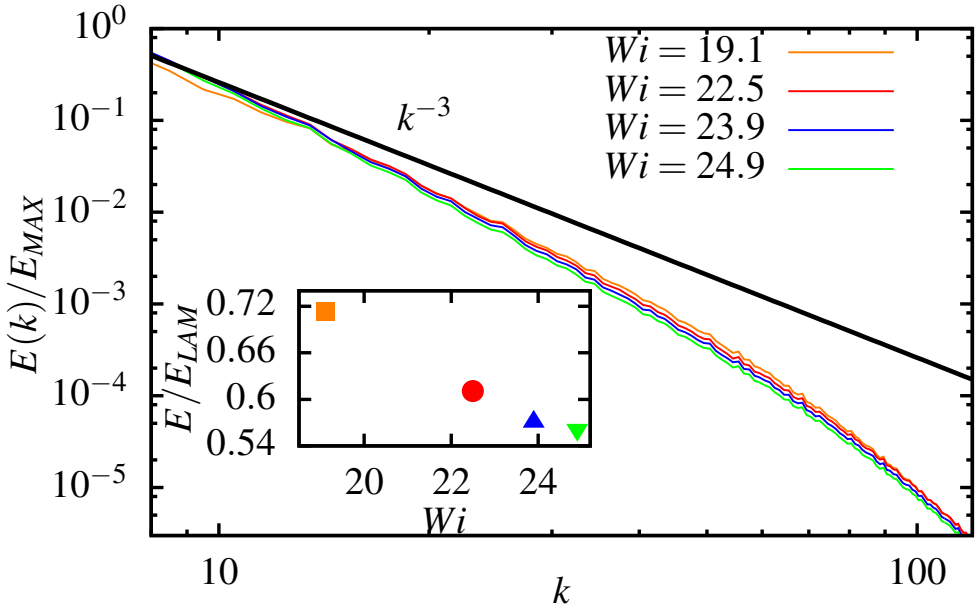

(a)

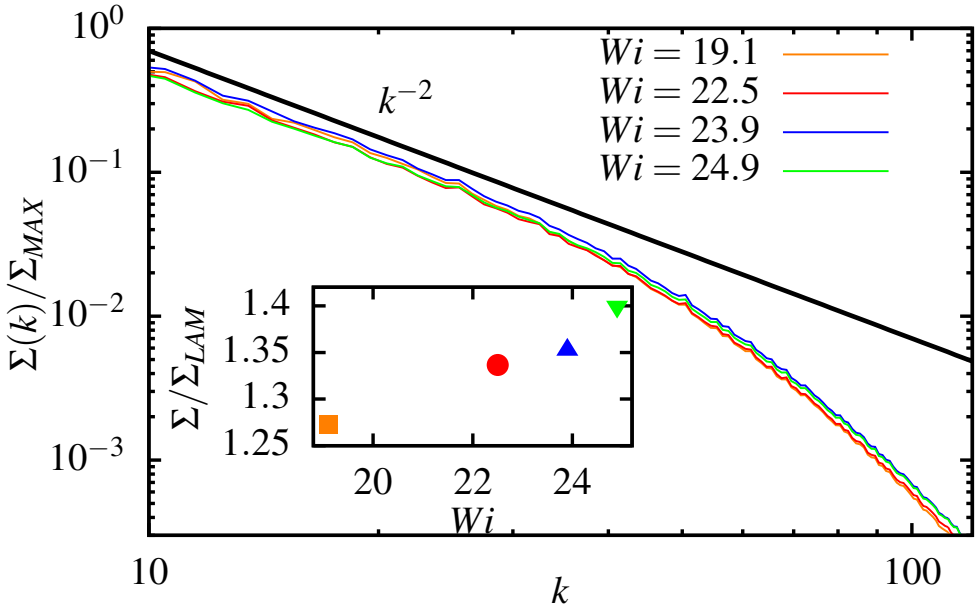

(b)

Figure 3.12: Time averaged spectra of kinetic energy $E(k)$ (a) and trace of the conformation tensor $\Sigma(k)$ at wavenumber k (b), normalized by their maximum values, for different values of Wi in the elastic turbulence regime. Inset of panel (a): temporally averaged kinetic energy $E = \overline{|\boldsymbol{u}|^2}/2$ normalized by its laminar value $E_{LAM} = U_0^2/4$. Inset of panel (b): temporally and spatially averaged square polymer elongation $\Sigma = \overline{tr(\boldsymbol{\sigma})}$ normalized by its laminar value $\Sigma_{LAM} = 2 + \frac{Wi^2}{4}$.

netic energy decreases with Wi, the square polymer elongation grows and this occurs faster than in laminar conditions. This suggests that the polymers elongate by draining energy from the mean flow and, once sufficiently stretched, they are capable of modifying the carrier flow through the term $\frac{2\eta\nu_s}{\tau}\boldsymbol{\nabla}\cdot\boldsymbol{\sigma}$ in Eq. (3.1). The faster than laminar growth means that such elastic coupling is very efficient in sustaining the stretching of the polymers.

3.4.2 Flow structure and velocity profiles

In the present case, due to the inhomogeneity induced by the Kolmogorov forcing, it is also important to know the mean flow in some detail, for instance, measurements of the velocity field ($\boldsymbol{u}(x,y)$) at different instants of time, where x is the direction of the mean flow and y the transverse direction over which its intensity varies. We indicate profiles with $\langle(...)\rangle$. Note that this type of average is related to the global one introduced before by

$$\overline{(...)} = \frac{1}{L_0}\int_0^{L_0}\langle(...)\rangle dy.$$

The mean profiles of the flow in the y direction averaged along the x direction and time and the profiles of the velocity fluctuations, $\langle u_y^{'2}\rangle(y)$ at different values of the Weissenberg number are shown in Fig. 3.13. To accelerate the convergence, indeed quite slow, of the velocity profiles, the results are obtained by further averaging over an ensemble of 7 independent data sets, each of which was obtained from slightly different random initial conditions. The mean flow profile $\langle u_x\rangle(y)$ at $Wi \leq 10$ is virtually indistinguishable from the laminar fixed point solution $U_0\cos(y/L)$, with $U_0 = 4$ and $L = 1/4$ (solid black line in Fig. 3.13(a)). The elastically-driven turbulent flow has a similar cosine shape but with reduced amplitude, $U < U_0$. While U gradually decreases as the Weissenberg number is increased, the average intensity of the transversal velocity fluctuations simultaneously grows. Due to the very slow convergence of the profiles of the fluctuations, it is not easy to assess their functional dependence on y. To overcome this problem, we further averaged the profiles over one forcing wavelength $\ell = L_0/4 = 2\pi$. As is clear from Fig. 3.14(b), this approach allows us to put in evidence that also the profile $\langle u_y^{'2}\rangle(y)$ can be reasonably well described by a trigonometric function, but with a periodicity that is twice that of $\langle u_x\rangle(y)$. It is worth remarking that an analogous behaviour has been found for the turbulent velocity fluctuations of the Newtonian Kolmogorov flow [34]. These results shows the need to provide a priori estimates of the non-dimensional pa-

rameters, we will refer to them as Re_0 and Wi_0, which can be different from the one in the presence of velocity fluctuations superimposed on a non-zero mean flow U (i.e. the a posteriori estimates of Re and Wi), once the average velocity U has been computed. In Table 3.2 we provide the a priori and a posteriori measures of the Reynolds and Weissenberg numbers used in this thesis to capture the phenomenology of elastic turbulence.

τ	U	Re_0	Wi_0	Re	Wi
1.125	3.483885	1	18	0.871	15.7
1.25	3.30861	1	20	0.827	16.5
1.375	3.20632	1	22	0.801	17.6
1.5	3.17946	1	24	0.795	19.1
2	2.80765	1	32	0.702	22.5
2.25	2.65692	1	36	0.664	23.9
2.5	2.4769	1	40	0.619	24.9

Table 3.2: DNS parameters: resolution 512^2, τ polymer relaxation time, U are a posteriori estimates of mean flow intensity, Re_0, Wi_0 are a priori estimates of the Reynolds number and Weissenberg number, Re, Wi are a posteriori estimates of the Reynolds number and Weissenberg number.

Further interesting information can be extracted from the behaviour of the ratio of the root-mean-square velocity fluctuation to the amplitude of the mean flow, $\sqrt{\overline{u_y'^2}}/U$ as a function of the Weissenberg number. This quantity is shown in Fig. 3.15, where a change in behaviour is clearly visible for $Wi \approx 20$. Such a transition is associated with an increase in the relative weight of the typical velocity fluctuation with respect to the mean flow. Also, recalling that, as observed from previous visualizations, at $Wi = 19$ the flow still presents intense coherent structures, the value $Wi \approx 20$ may be interpreted as the one beyond which a developed turbulent state sets in, where the statistical features of the flow attain a somewhat universal behaviour essentially independent of Wi (e.g. the spectra in Fig. 3.12, and see also [82, 176]). We remark that the lines in Fig. 3.15 are only for guidance; here we do not claim to explain the corresponding scaling exponents and we think that this technical point deserves more research.

We have further measured the probability distribution function (PDF) of the square polymer elongation, i.e. the trace of the polymer conformation tensor $\boldsymbol{\sigma}$ shown in Fig. 3.16. We observe a broad distribution of the extension of polymer molecules in Fig. 3.16 (a)), which results in the turbulent-

like structures in the flow even at low Re. The results of the PDF upon rescaling are also shown in Fig. 3.16(b). The results shows that even this statistical quantity shows a behaviour that is independent of Wi for $Wi > 20$, in accordance with Fig. 3.15.

3.4.3 The Lyapunov exponent for elastic turbulence

Laboratory experiments in curvilinear channels have demonstrated that very viscous polymer solutions in the elastic turbulence regime allow efficient mixing [22]. The mixing efficiency of polymer solutions has been studied in other setups, including microchannel flows [18] and two-dimensional, magnetically driven flows [177]. In a smooth flow, as is the case of elastic turbulence given that the kinetic energy spectrum $E(k) \sim k^{-\gamma}$ decays faster than k^{-3} with the wavenumber, the dispersion properties are essentially governed by the largest scales and, dimensionally, only one time scale can be constructed. The typical time over which mixing takes place can then be identified with the inverse of the rate of spreading, due to their chaotic dynamics in a Lagrangian sense, of initially close fluid elements. The quantitative understanding of the degree of chaoticity (from a Lagrangian point of view) in a fluid flow is the maximal Lagrangian Lyapunov exponent (LLE), which defines the average rate of exponential separation of two initially neighbouring trajectories followed by Lagrangian tracer particles:

$$\lambda = \lim_{t\to\infty} \lim_{\delta(0)\to 0} \frac{1}{t} \log\left[\frac{\delta(t)}{\delta(0)}\right] \tag{3.35}$$

where $\delta(t) = \| \boldsymbol{x}_2(t) - \boldsymbol{x}_1(t) \|$ is the Euclidean distance between the two trajectories at time t and $\delta(0)$ its value at the initial time. In experimental and numerical simulations, the infinite time limit required by Eq. (3.35) is unattainable. A way to overcome these difficulties is to use the finite-time Lyapunov exponent (FTLE). This is defined by removing the $t \to \infty$ limit in Eq. (3.35).

$$\lambda^* = \lim_{\delta(0)\to 0} \frac{1}{t} \left[\frac{\delta(t)}{\delta(0)}\right] \tag{3.36}$$

For sufficiently small initial separations $\delta(0)$ between the particles, at large times the FTLE becomes a rather good estimate of the LLE [178, 179].

Figure 3.17 shows the behaviour of the Lyapunov exponent rescaled by the polymer relaxation time τ as a function of Wi at fixed $Re = 1$. Numerical Lagrangian fluid trajectories were obtained by integrating over time $\frac{\mathrm{d}\boldsymbol{x}}{\mathrm{d}t} = \boldsymbol{u}(\boldsymbol{x}, t)$, using a second-order Runge–Kutta method. The instantaneous

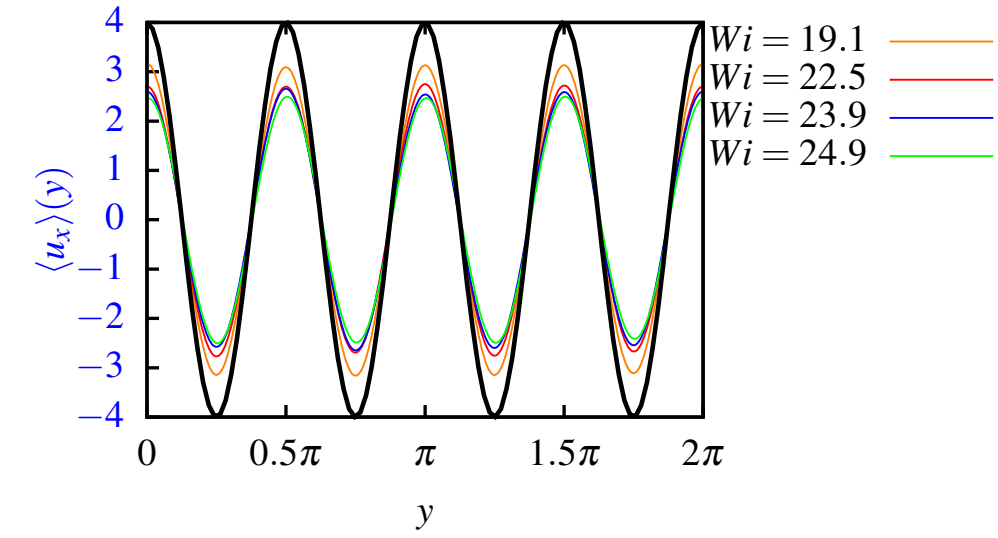

(a)

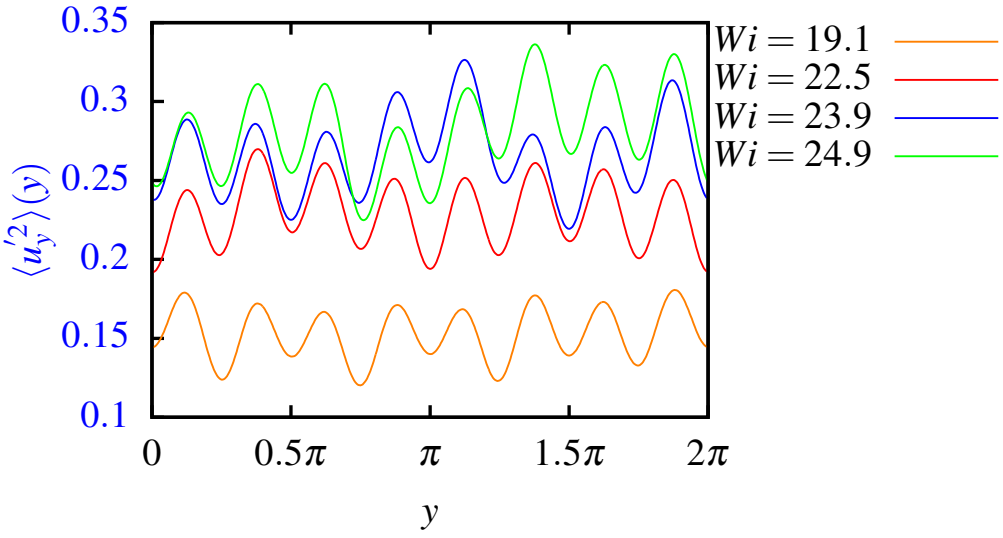

(b)

Figure 3.13: (a) Mean flow profile averaged along x direction and time. (b) Profile of velocity fluctuations along the direction of inhomogeneity of the flow for different Wi. Here, temporal averages were performed over 80 independent realizations corresponding to different instants of time. All the profiles shown have been further averaged over the wavelength defining the periodicity of the mean flow $\ell = LL_0 = \pi/2$. The black solid line represents the mean flow profile $U_0 \cos(y/L)$ with ($U_0 = 4$ and $L = 1/4$) corresponding to the laminar fixed point solution.

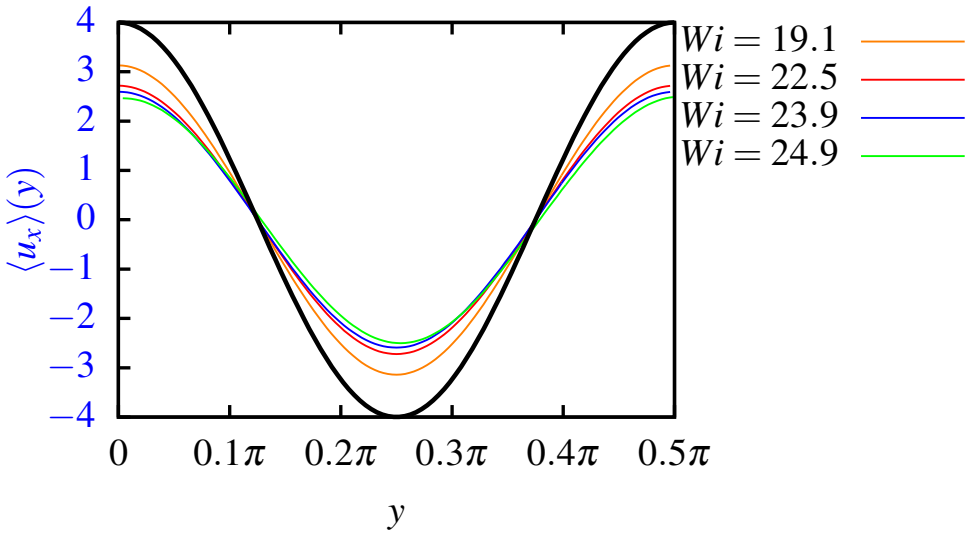

(a)

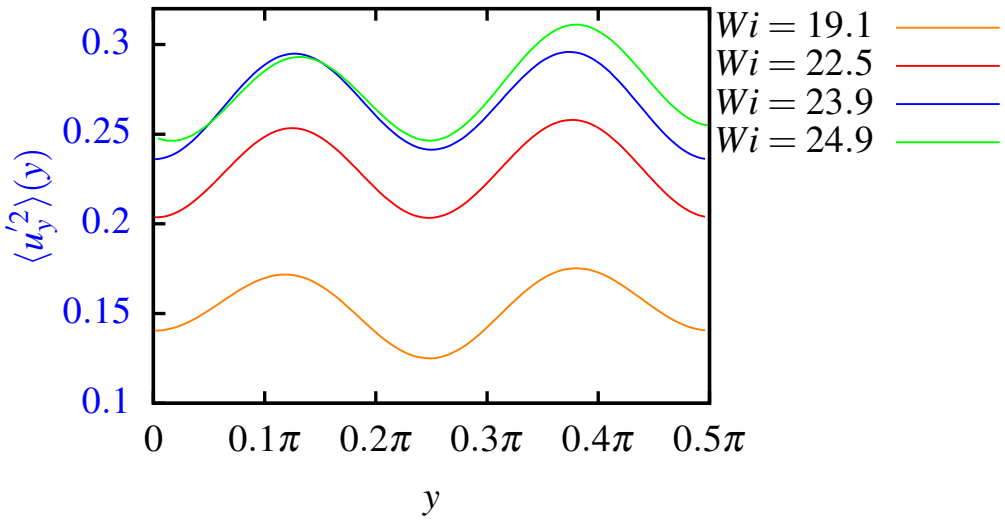

(b)

Figure 3.14: (a) Mean flow profile averaged along x direction and time. (b) Profile of velocity fluctuations along the direction of inhomogeneity of the flows for different Wi. Here, temporal averages were performed over 80 independent realizations corresponding to different instants of time. All the profiles shown were further averaged over the wavelength defining the periodicity of the mean flow $\ell = LL_0 = \pi/2$. The black solid line represents the mean flow profile $U_0 \cos(y/L)$ with ($U_0 = 4$ and $L = 1/4$) corresponding to the laminar fixed point solution.

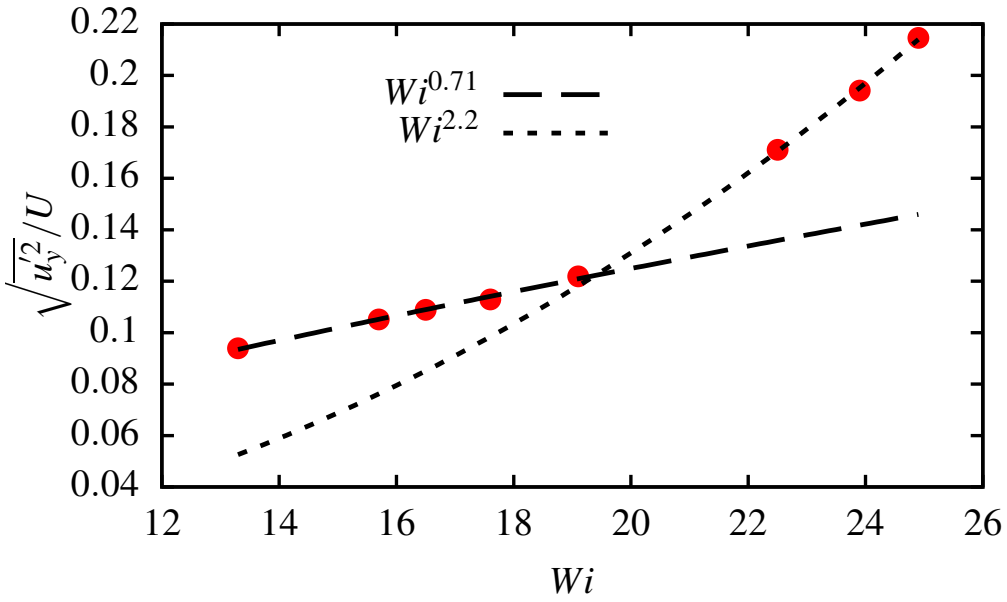

Figure 3.15: Root-mean-square velocity fluctuations divided by the amplitude of the mean flow $\sqrt{\overline{u_y'^2}}/U$ versus Wi. The dashed lines correspond to power-law behaviour, as obtained by a fit, and are shown to highlight the change from the transitional to the developed regime.

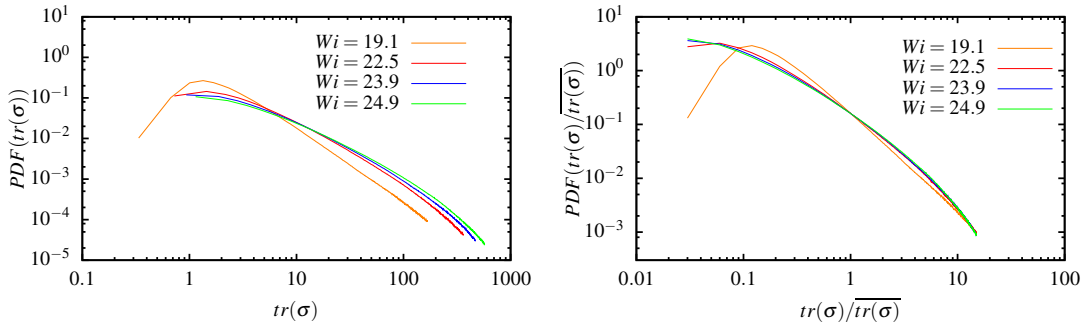

Figure 3.16: (a) The PDF of square polymer elongation $tr(\boldsymbol{\sigma})$, (b) The PDF of square polymer elongation normalized by its mean value $tr(\boldsymbol{\sigma})/\overline{tr(\boldsymbol{\sigma})}$.

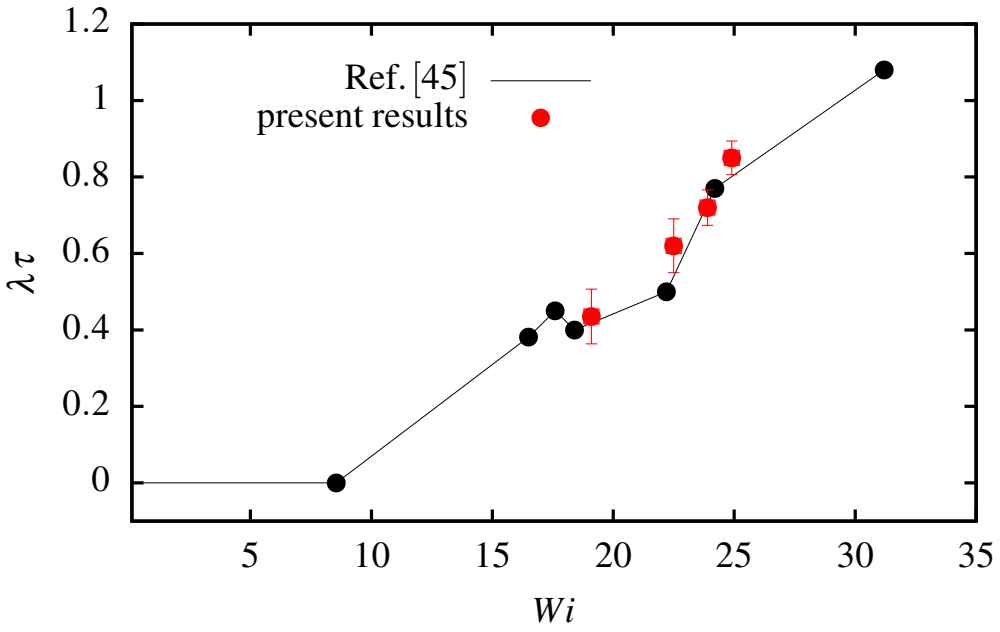

Figure 3.17: Comparison of the maximal Lagrangian Lyapunov exponent from the present DNS results (red dots) with previous results (black dots) [90], obtained in the same setup but varying the flow stability parameters (Re and Wi) in a different way.

velocity at a fluid tracer position was obtained by bilinear interpolation in space of the velocity field known at regularly gridded points. The results demonstrate that the mixing becomes more efficient as Wi increases. We remark that this behaviour is in some way contrary to that observed in the case of visco-elastic flows at high Reynolds numbers, where it has been seen that the injection of polymers reduces the degree of chaoticity [67]. Of course, this cannot be valid in the present situation because $\lambda = 0$ in the absence of a polymer, and therefore, at least in some range, the chaoticity must increase with Wi. Consequently, we expect that the dependence of the FTLE on Wi will have a jump corresponding to the first flow reorganization in the intermediate regime, followed by a slower increase in the fully developed elastic turbulent states. This result is comparable with previous numerical results obtained in the same flow setup but where, unlike the present case, Wi was varied keeping the ratio Wi/Re fixed [90].

Chapter 4

Small-scale inhomogeneities of inertial particles in an elastic turbulent Kolmogorov flow

Contents

4.1 Introduction

One of the most distinguishing characteristics of turbulence is its ability to efficiently mix transported substances. As we discussed earlier in Chapter 2, particles with non-zero size and inertia do not exactly follow the flow. In fact, due to their inertia, such particles behave differently from fluid the particles and become inhomogeneously distributed. This happens because particles heavier than the carrier fluid are expelled from the cores of vortical structures, because of centrifugal forces, while the opposite is observed for particles lighter than the carrier flow. This results in highly non-uniform particle distributions, where particles concentrate in regions of high strain rate and low vorticity. This process is schematically illustrated in Fig. 2.3. Let us remark, here, that Lagrangian tracers (i.e. non-inertial particles for which $St = 0$) evolve according to $\dot{\boldsymbol{x}} = \boldsymbol{u}$ (with $\boldsymbol{\nabla} \cdot \boldsymbol{u} = 0$) only and, consequently, homogeneously sample the flow field over sufficiently long

times. It is worth remarking that this phenomenon is independent of turbulence and has also been observed in laminar flows, both steady and time-dependent/chaotic ones [36, 130].

In this chapter, we will discuss the particle dynamics in elastic turbulence, starting from an analysis of the statistical properties of their spatial distribution in relation with the main dynamical features of the visco-elastic fluid flow. We present the statistical results obtained from the same simulations as illustrated in the earlier chapter (see Chapter 3) for a 2D inhomogeneous visco-elastic Kolmogorov flow model.

4.2 Preferential concentration: Numerical simulations

To explore the dynamics of inertial particles in elastic turbulence, we have performd some direct numerical simulations. Equation (3.1) and Eq. (3.2) have been integrated using a pseudospectral method on a grid of side $L_0 = 2\pi$ with periodic boundary conditions at a resolution of 512^2.

Once the flow is in statistically stationary conditions, it is seeded with an ensemble of inertial particles, initially uniformly distributed in space and having randomly chosen velocities. The particle dynamics, Eq. (2.3), are integrated by means of a standard Lagrangian approach using a second-order Runge-Kutta time-marching scheme; the velocity at the particle position is obtained by bilinear interpolation in space. Periodic boundary conditions are imposed on the positions of the particles. A rather large number of Stokes time (τ_p) values have been examined, allowing exploring almost three decades in St (for each considered flow, i.e. for each Wi). In the results reported in the following sections, the number of particles is $N_p = 10^4$ (tests with $N_p = 10^5$ did not show any appreciable difference in the statistics of the single-particle observables).

Qualitatively, it is evident from Fig. 4.1, where $Wi = 23.9$ and St increases from left to right, that due to their inertia, the particles become non-homogeneously distributed in space. In the presence of inertia, the non-homogeneous character of the particle distribution appears to vary non-monotonically with St, with a maximum for intermediate values of this parameter. This is in agreement with intuitive expectations: for very small St one should recover tracer dynamics, while for very large St the particle dynamics should be essentially insensitive to the flow. Because in the limit ($\tau_p \to \infty$) the particle velocity converges to zero ($\boldsymbol{v} \to 0$), the particles will

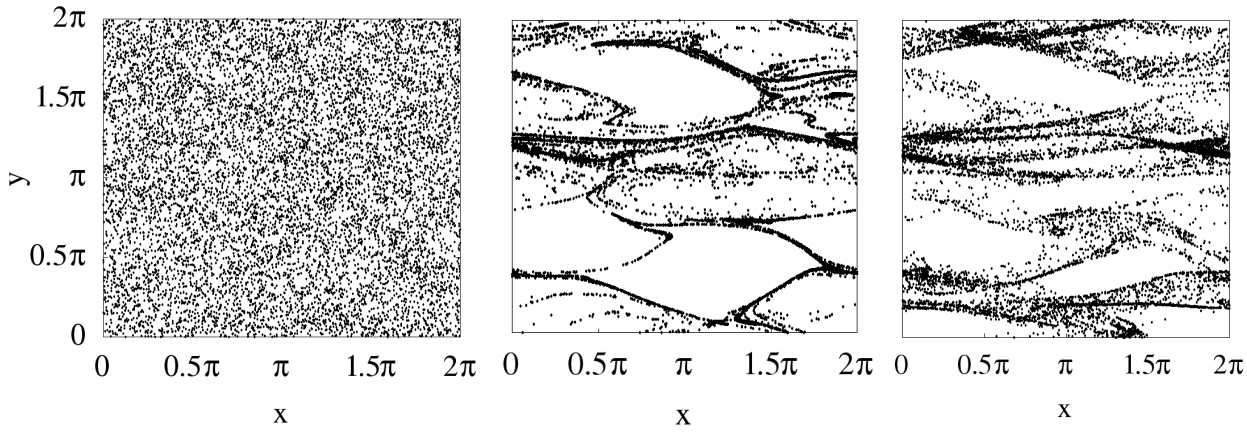

Figure 4.1: Particle distributions (black dots) for $St = 0.016$, $St = 0.657$ and $St = 5.75$ (from left to right) at a fixed instant of time at $Wi = 23.9$ and $Re = 0.664$; the number of particles is $N_p = 10^4$.

filter all the temporal scales of the flow. Ultimately in the large St limit, the particles will behave ballistically, and stay homogeneously distributed in time (if they were distributed homogeneously at the beginning).

We now discuss the particle dynamics, starting from an analysis of the statistical properties of their spatial distribution in relation with the main dynamical features of the visco-elastic fluid flow. We recall here the definition of the Stokes number $St = \tau_p/\tau_{\dot{\gamma}}$ as introduced in Chapter 2 (see Eq. (2.4)). Throughout this study, $\tau_{\dot{\gamma}} \approx 0.1$ (computed numerically using the definition introduced in Eq. (2.5)) and the polymer relaxation time τ is typically larger than both $\tau_{\dot{\gamma}}$ and τ_p. In Fig. 4.2 both the small-scale inhomogeneities and the larger scale modulations of the particle distributions are seen. A striking feature is, however, the accumulation of particles along thin filamentary structures characterized by large polymer elongations, i.e. large values of $tr(\boldsymbol{\sigma})$ (see the upper panel of Fig. 4.2). Such highly elastic filaments, propagating along the mean flow direction, are associated with the stretching of polymers by the largest gradients of the mean velocity field [171]. Similar wavy patterns also characterize the vorticity field $\zeta = \partial_x u_y - \partial_y u_x$ (see the bottom panel of Fig. 4.2), due to the coupling between the polymer dynamics and the velocity dynamics. The strong correlation between the spatial organization of the particle distribution and that of the polymer conformation tensor field is further evidenced by plotting the latter by means of an ellipsoid representation of the local (in space) principal elongations (the central line of Fig. 4.2). Here the axes of the ellipses

are oriented in the directions of the eigenvectors of $\boldsymbol{\sigma}$ and their sizes are proportional to the corresponding eigenvalues.

In order to quantitatively assess this point, we computed the trace of the conformation tensor $\overline{tr(\boldsymbol{\sigma})}$, averaged over the entire spatial domain and a long time history, experienced by the inertial particles as a function of the Stokes number and for different values of Wi. The curves shown in Fig. 4.3 have a non-monotonic behaviour, with a maximum of $\overline{tr(\boldsymbol{\sigma})}$ for $St \approx 1$. Their qualitative features are generic with respect to the value of the Weissenberg number. Indeed, as shown in the inset of Fig. 4.3, after rescaling $\overline{tr(\boldsymbol{\sigma})}$ by the same quantity $\overline{tr(\boldsymbol{\sigma})}_{St=0}$ computed for the tracers in the same flow (for each Wi) we obtain a good collapse of the data, indicating the independence from Wi of this observable. These results demonstrate that when the inertia is increased, yet not too large, meaning not larger than the characteristic time scale in the flow, which is $\tau_{\dot{\gamma}}$, particles have an increasing tendency to concentrate where the polymers are highly stretched. Moreover, as is clear from the inset of the figure, independently of St, the inertial particles have larger values of $tr(\boldsymbol{\sigma})$ than fluid-flow Lagrangian tracers.

In our flow model, the particles are not directly coupled to the polymers, therefore to understand the phenomenology described above, one has to relate the elastic filaments to the velocity field that transports the particles. A hint in this regard comes from inspection of the ellipsoid-glyph visualizations of the polymer conformation tensor (see the central line of Fig. 4.2, where the axes of the ellipses are oriented in the directions of the eigenvectors of $\boldsymbol{\sigma}$ and their sizes are proportional to the corresponding eigenvalues). In these plots, the presence of regions of recirculating motion is evident, with elastic filamentary structures playing the role of flow separatrices (as is also observed in numerical simulations of visco-elastic cellular flows [130]). A more detailed description of the formation of vortices in an elastic turbulence flow, using different forcings, can be found in [130, 171].

Moreover, as discussed earlier in Section 2.4.2, a few quantitative predictions drawn from the particle equations of motion given by Eq. (2.3) capture the main features of the behaviour of heavy inertial particles. At least in the limit of small St (where a field approach to the description of the particle velocity can be considered) the behaviour of the particles can be explained in the terms of Okubo–Weiss parameter Q [128, 129]. We recall here the definition of Q:

$$Q = \frac{1}{2}(\Omega_{ij}\Omega_{ij} - S_{ij}S_{ij}). \tag{4.1}$$

In this equation, S_{ij} and Ω_{ij} respectively indicate the elements of the rate-

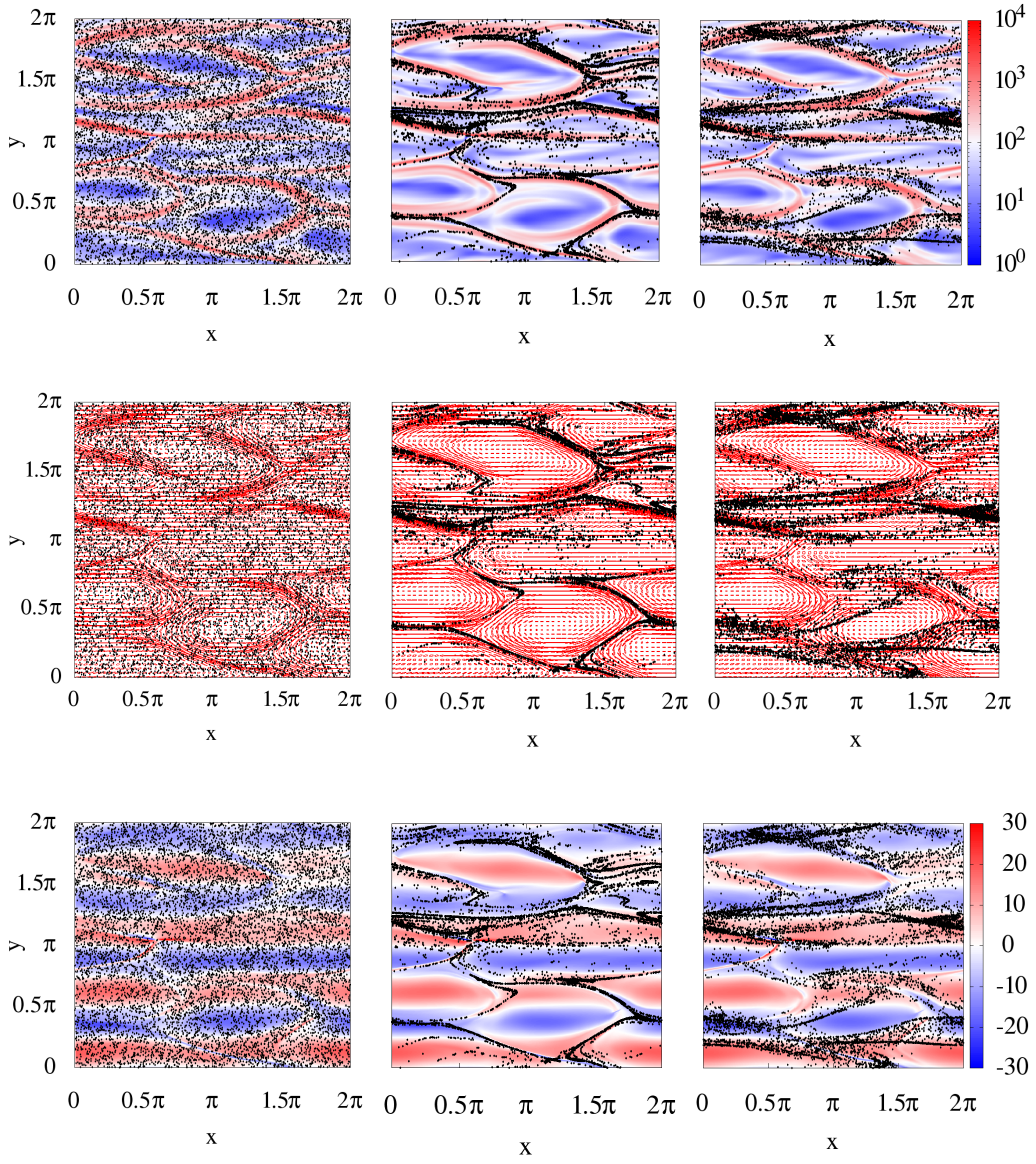

Figure 4.2: Particle distributions (black dots) for $St = 0.016$, $St = 0.657$ and $St = 5.75$ (from left to right) at a fixed instant of time in statistically stationary conditions at $Wi = 23.9$ and $Re = 0.664$; the number of particles is $N_p = 10^4$. The pseudocolour plots in the upper and bottom panels correspond to instantaneous snapshots of $[tr(\boldsymbol{\sigma})](x, y)$ and vorticity $\zeta(x, y) = \partial_x u_y - \partial_y u_x$ at the same time for which the particles are plotted. In the central panel, the particles are plotted together with an ellipsoid-glyph visualization of the polymer conformation tensor $\boldsymbol{\sigma}$.

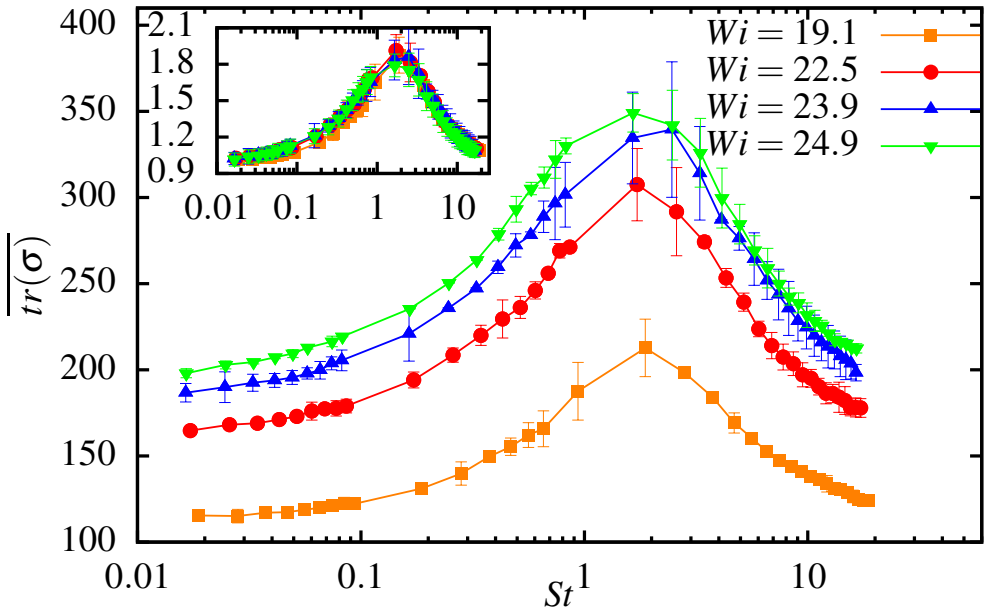

Figure 4.3: Average trace of the conformation tensor $\overline{tr(\boldsymbol{\sigma})}$ experienced by particles as a function of St and for different Weissenberg numbers. Here temporal averages were performed over 50 snapshots of $tr(\boldsymbol{\sigma})$ (and simultaneous particle distributions) corresponding to different instants of time separated by an interval larger than the typical flow time scale. The inset shows the same after rescaling $\overline{tr(\boldsymbol{\sigma})}$ by its value computed using Lagrangian tracers $\overline{tr(\boldsymbol{\sigma})}_{St=0}$.

of-strain ($\boldsymbol{S}$) and rate-of-rotation ($\boldsymbol{\Omega}$) tensors, and summation over repeated indices is assumed. The particles concentrate due to the (weak) compressibility of their velocity, that is, where $\boldsymbol{\nabla}\cdot\boldsymbol{v} < 0$. From Eq. (2.10) it is seen that this condition translates into negative values of Q, meaning that the particles are expected to concentrate preferentially in strain dominated regions (using Eq. (4.1)). Figure 4.4 shows the spatially and temporally averaged Okubo–Weiss parameter measured at particle positions versus St and for different Weissenberg numbers. The results support the above argument and provide a quantitative confirmation of what was observed from Fig. 4.2. Indeed, $\overline{Q}$ is found to be always negative, which suggests that particles are ejected from recirculating regions to become more concentrated in regions dominated by strain, where the polymers are highly elongated. Also in this case, the effect is a maximum (i.e. $\overline{Q}$ is a minimum) for $St \approx 1$. The effect of varying Wi is found to be quite weak. In the left inset of Fig. 4.4 we show the

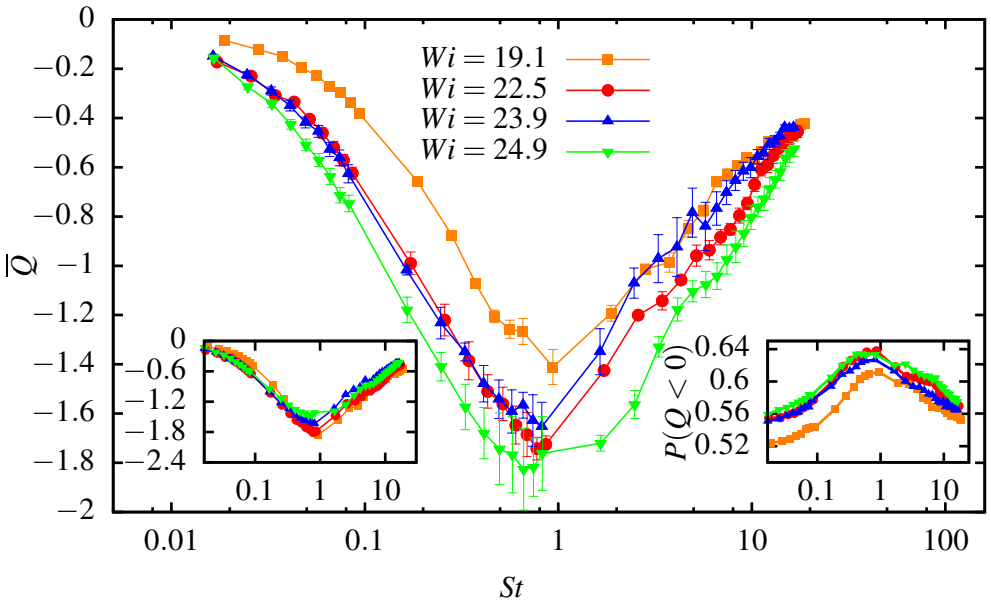

Figure 4.4: Average Okubo–Weiss parameter $\overline{Q}$ of particles as a function of St. Here, temporal averages were performed over 50 snapshots of Q (and simultaneous particle distributions) corresponding to different instants of time separated by an interval larger than the typical flow time scale. Left inset: normalized Okubo–Weiss parameter $\overline{Q}/Q^{rms}_{St=0}$ as a function of St, where $Q^{rms}_{St=0}$ is the root-mean-square value of the Q of the Lagrangian tracers. Right inset: probability that a particle is in strain dominated region $P(Q < 0)$ as a function of the Stokes number.

behaviour, versus St, of the Okubo–Weiss parameter rescaled by its root-mean-square (rms) value computed for the tracers $Q^{rms}_{St=0}$ (since $\overline{Q} = 0$ for Lagrangian tracers and, equivalently, for an Eulerian fluid flow, from numerical simulations). After rescaling, the results are only very weakly dependent on Wi. In the right inset of Fig. 4.4, the plot presents the probability $P(Q < 0)$ that a particle is in a strain dominated region, which is computed as the ratio between the number of particles at positions where $Q < 0$ and the total number of particles, as a function of St. This probability $P(Q < 0)$ generally takes values larger than realized in the limit of very small St. Despite its not being large, such an increase of $P(Q < 0)$ [114, 125] indicates that inertial particles are more concentrated than tracers in regions where $Q < 0$. Finally, we observe that the effect is, again, a maximum for $St \approx 1$ and weakly dependent on Wi.

4.3 The correlation dimension

The previous analysis allowed us to see some relations between the inhomogeneities of the particle distribution and the flow structures. The fine scale properties of particle clustering are, however, a more general consequence of the contraction of volumes in the phase space of the dissipative system of Eq. (2.3) [36]. In both laminar unsteady and turbulent flows, it has been shown that the motion of inertial particles at small scales is highly non-trivial and, at sufficiently large times, occurs on a fractal set [36,37,180]. One should note that this is true both for particles that are heavier and lighter than the fluid [37]. A way to quantitatively characterize the clustering is then to measure the fractal dimension of the projection, in physical space, of the attractor of the dynamics. When this is smaller than the dimension of the full physical space, particle pairs are more likely separated by small distances. Within this framework, we recall that a useful indicator is the correlation dimension D_2 [138], which is defined as

$$D_2 = \lim_{r \to 0} \frac{\mathrm{d} \log C(r)}{\mathrm{d} \log r}, \tag{4.2}$$

with the correlation sum $C(r)$ (for details, see Section 2.4.3).

The behaviour of D_2 as a function of the Stokes number for different values of Wi is presented in Fig. 4.5. It is seen that the correlation dimension decreases from a value, which is realized in the limit of very small St, close to $D_2 = 2$ (corresponding to tracers homogeneously filling the whole spatial domain) to attain a minimum value of $D_2 \approx 1$ for $St \approx 1$. We remark that for very low particle inertia, the decrease of D_2 is quadratic in St (see the inset of Fig. 4.5), as typically happens in correlated flows [100]. For even larger values of the Stokes number, D_2 grows to approach again the space filling value of 2 (expected for particles with large inertia, which are insensitive to the flow) in the limit of very large St. We find that the correlation dimension is weakly dependent on the Weissenberg number, for the values of Wi explored here. The maximum difference, for fixed St, is found to not exceed 0.15. We can therefore conclude that small-scale clustering is a generic and quite effective phenomenon in elastic turbulence flows, producing, at its maximum, particle accumulation on quasi one-dimensional fractal sets. Our results are qualitatively similar to previous ones obtained in simulations of 2D smooth random flows [181].

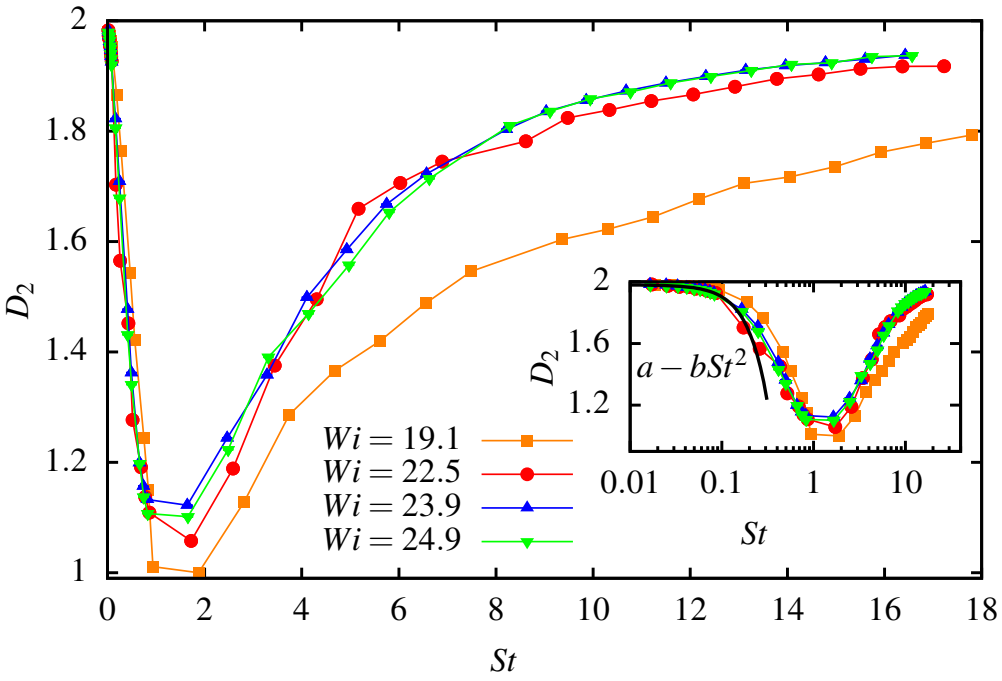

Figure 4.5: Correlation dimension D_2 of particle distributions as a function of St and for different Weissenberg numbers; uncertainties are of the order of the size of the point. Small-scale clustering is maximal for $St \sim 1$, where D_2 has a minimum. We remark that for very small particle inertia, the decrease of D_2 is quadratic in St (see the inset of Fig. 4.5), as typically happens in correlated flows. The relative difference between the values obtained for $Wi = 19.1$ and the corresponding ones for $Wi = 24.9$ is not larger than 0.15. The inset shows the same in log-linear scale; the solid line corresponds to $a - bSt^2$ with $a = 1.98$ and $b = 7.74$ after averaging the values of the fitted parameters obtained for each Wi.

4.4 The Kaplan–Yorke dimension D_{KL}

We further examined the small-scale clustering behaviour by considering the quantification of the fractal dimension of the particle dynamics' attractor, which is measured by the Kaplan–Yorke dimension. In the context of particle laden flows, such a measurement has been considered for smooth chaotic flows [36, 181] and for 3D turbulent flows [39, 115] (details can be found in Chapter 2). The Kaplan–Yorke dimension can be defined as the fractional dimension in which a cluster of initial conditions will neither expand nor contract as it evolves in time. To measure the

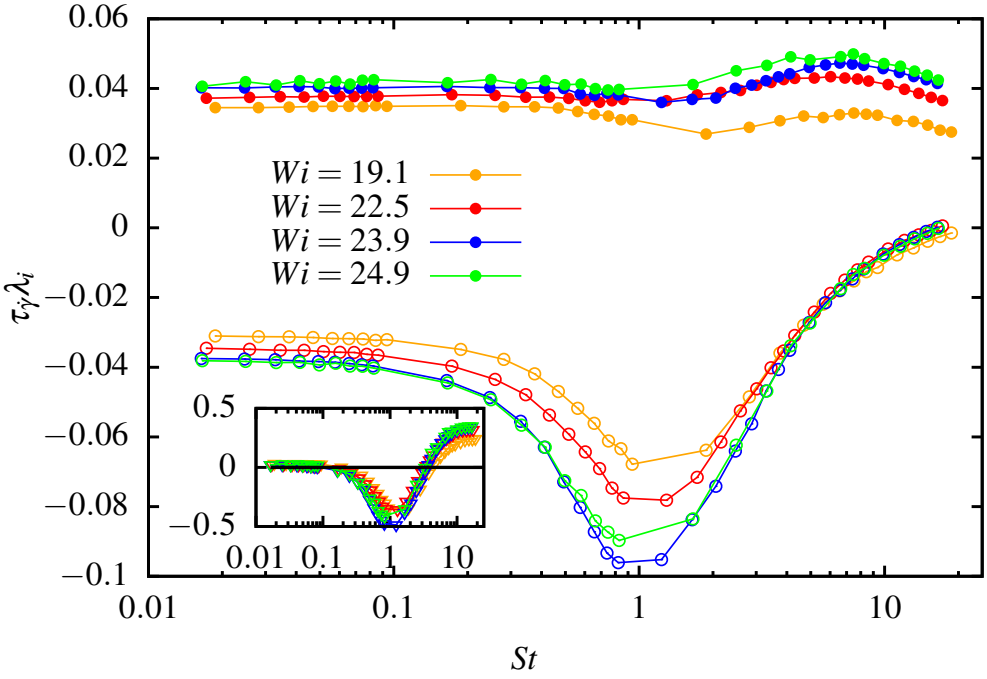

(a)

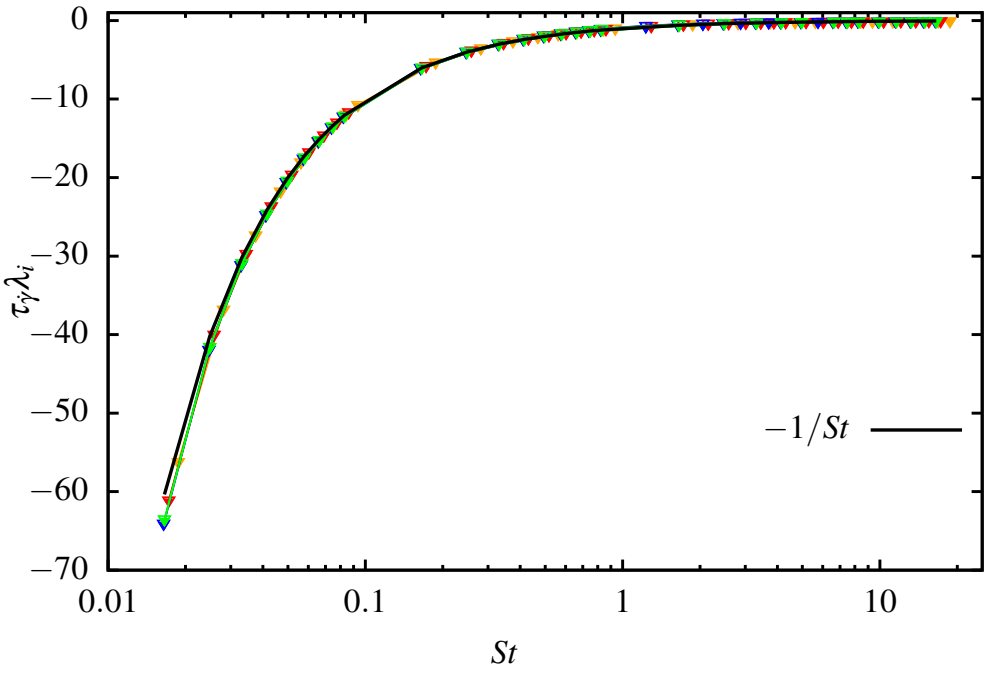

(b)

Figure 4.6: Comparison of the normalized Lyapunov exponents of the inertial particles as a function of St for simulations of 2-dimensional elastic turbulent flow at different Wi. (a) Lyapunov exponents λ_1 (•) and λ_2 (○) for $Wi = 19.1; Wi = 22.5; Wi = 23.9; Wi = 24.9$; Inset: sum of the first two Lyapunov exponents $(\lambda_1 + \lambda_2)$. (b) Lyapunov exponents $\lambda_3(\triangledown)$ and $\lambda_4(\blacktriangledown)$ as a function of St, behaving approximately as $-1/\tau_p$ (solid black line).

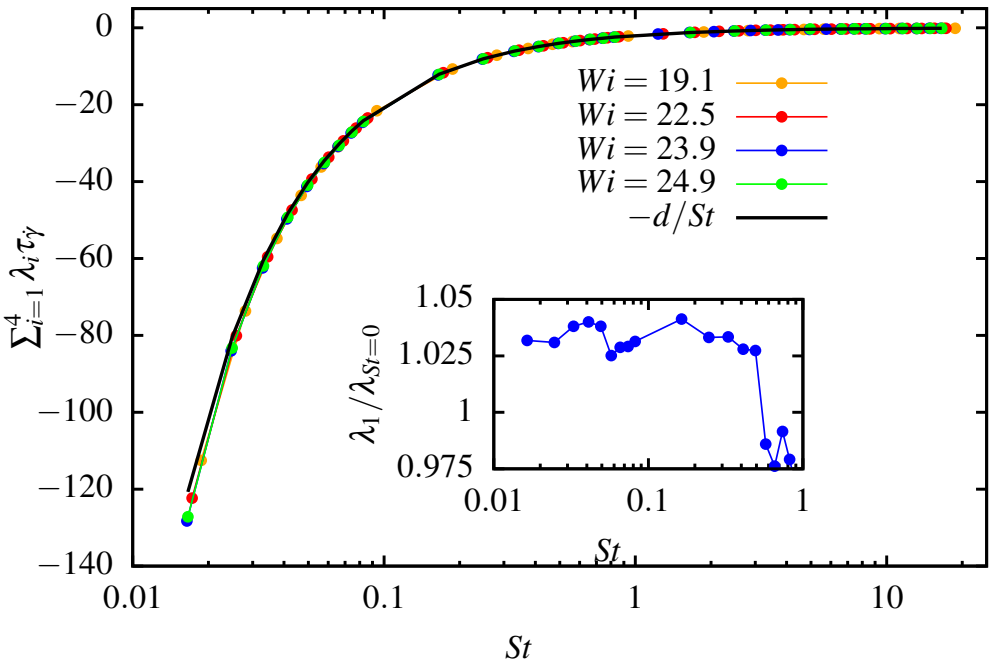

Figure 4.7: The sum of the 2D stretching rates (λ_i) controls the time evolution of phase-space 2D-dimensional volumes, typically behaves as $-d/St$ (see solid black line). In the inset we show the relative growth of the first Lyapunov exponent $\lambda_1/\lambda_{St=0}$ as a function of St, occurring at small St.

Lyapunov spectrum numerically in a d-dimensional flow, which is needed to estimate the Kaplan–Yorke dimension, we follow along each particle trajectory the time evolution of $2 \times d$ infinitesimal displacements in the position–velocity phase space obtained by linearizing the particle dynamics (Eq. (2.3)). The infinitesimal 2d-volume V_{2d}, defined by $2d$ linearly independent tangent vectors, grows in time at an exponential rate $\sum_{i=1}^{2d} \lambda_i = \lim_{t\to\infty}(1/t)\log\left[V_{2d}(t)/V_{2d}(0)\right]$, where λ_i are the Lyapunov exponents. In order to prevent numerical errors from accumulating and the length of the infinitesimal separations from increasing rapidly, their calculation indeed requires the adoption of frequent renormalizations in order to avoid numerical blow-ups. This is done by means of a Gram–Schmidt procedure [147]. A convenient and widely used algorithm for the evaluation of Lyapunov exponents was proposed by Benettin et al. [182], see also the book by Crisanti *et al.* [147] for a precise description of this method.

Fig. 4.6(a) shows the behaviour of the first two Lyapunov exponents (λ_1, λ_2) after normalizing by $\tau_{\dot\gamma}$ as a function of the Stokes number for different values of the Weissenberg number Wi. The other two normalized Lyapunov exponents (λ_3, λ_4) are shown in Fig. 4.6(b). Before discussing the Kaplan–Yorke dimension measured using the Lyapunov spectrum, we would like to provide some of the observations about the λ_i that are supported by our data.

- For the range of Stokes numbers studied here, we observe $\lambda_3 \sim \lambda_4$ scale as $-1/St$, indicating the relaxation of particle velocities to the fluid (see Fig. 4.6(b)). It appears as if the corresponding eigendirections align with the velocity.

- The other two directions (λ_1, λ_2) would account for the time evolution of the volume in physical space (in the small Stokes limit), which means the first two exponents (λ_1 and λ_2) rule the time evolution of infinitesimal elements in the physical space. Our numerical data shows that the sum of $\lambda_1 + \lambda_2$ is not very far from zero in the small St limit, shown in the inset of Fig. 4.6(a).

- As in the small St limit the component $(\lambda_1+\lambda_2)$ of the sum of Lyapunov exponents $(\lambda_1 + \lambda_2 + \lambda_3 + \lambda_4)$ represents the volume in physical space (shown above), it is also reasonable to say that one of the Lyapunov exponents λ_1 is related to one direction in physical space. Roughly speaking, the largest Lyapunov exponent λ_1 estimates the chaotic separation of particle trajectories in physical space.

- As emphasized in the inset of Fig. 4.7, for $St < 0.1$, λ_1 is not very different than the Lyapunov exponent of the fluid tracers ($St = 0$).
- If $St \to 1$, we have a maximum of clustering, and if we consider separation in the whole space it's less chaotic (because of clustering, the particles do not go everywhere), hence for $0.1 < St < 1$, we observe that the Lyapunov exponent of the fluid tracers becomes larger than λ_1.

It is worth commenting that this behaviour of the Lyapunov exponents is just an observation supported by our data, which still awaits a full theoretical understanding. The same kind of behaviour for the Lyapunov exponents of inertial particles has already been seen in 3D homogeneous and isotropic turbulent flows [115].

The fractal dimension of this attractor is estimated by means of the Kaplan–Yorke dimension [145–147]. We recall the definition of D_{KY} introduced in Section 2.4.3: $D_{KY} = K + \frac{\sum_{i=1}^{K} \lambda_i}{|\lambda_{K+1}|}$, where the λ_i are the Lyapunov exponents and K is the largest index such that $\sum_{i=1}^{K} \lambda_i \geq 0$, once the Lyapunov exponents λ_i are ranked in decreasing order. The k-dimensional hyper-volumes should either increase or remain constant, while the $K+1$-dimensional ones should contract to zero (see Section 2.4.3 for a detailed discussion). Note that this formula (Eq. (2.14)) is a simple linear interpolation between K and $K+1$. Our results are analogous to those in [36, 183] and are shown in Fig. 4.8. The minimum at $St \approx 1$ corresponds to maximal clustering. For Stokes numbers $St > 4$, the fractal dimension becomes greater than $d = 2$, indicating that the spatial distribution of the particles is no longer fractal.

Another important observation in these results is that the Kaplan–Yorke dimension D_{KY} at low Stokes numbers behaves as $D_{KY} \sim a - bSt^2$, $a \approx 2$. Such a quadratic behaviour for vanishingly small Stokes number has been obtained theoretically by Balkovsky *et al.* [113] under the approximation of advection by a synthetic compressible flow. The correlation dimension D_2, studied in Section 4.3, has a qualitatively similar behaviour in the Stokes number to that of D_{KY}, but they have, however, a different amplitude ($D_2 \leq D_{KY}$). A plausible explanation for their quantitative difference is that they are different measurements of different fractal sets: D_2 is for a spatial set of particle positions in physical space, the D_{KY} is for the dimension of the particle dynamical system attractor in the phase space. Several theoretical arguments and numerical results claims that the Kaplan–Yorke dimension

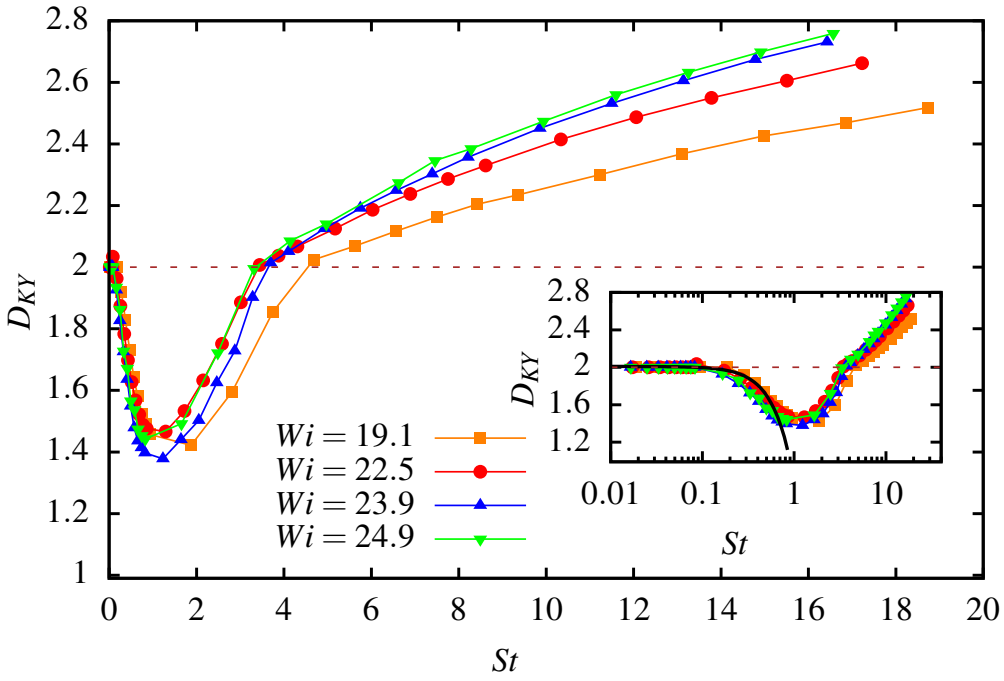

Figure 4.8: Kaplan–Yorke dimension D_{KY} of heavy inertial particles as a function of St and for different Weissenberg numbers; small-scale clustering is a maximum for $St \sim 1$, where D_{KY} has a minimum. The inset shows the same in log-linear scale; the solid line corresponds to $a - bSt^2$ with $a = 2.003$ and $b = 1.728$ after averaging the values of the fitted parameters obtained for each Wi.

is close to other types of fractal dimension, such as the capacity dimension (D_C), the information dimension (D_I), and the correlation dimension (D_2), for typical strange attractors [138, 184], so that there is a hierarchy of fractal dimensions ($D_2 \leq D_I \leq D_C \approx D_{KY}$) [181]. Grassberger and Procaccia [138] have also argued that there is a direct connection in the form of an inequality ($D_2 \leq D_{KY}$) between the correlation dimension and the Kaplan–Yorke dimension. This inequality is consistent with our numerical results.

4.5 The segregation indicator

In Section 4.2 and Section 4.3 we found that in 2D elastic turbulent flows, particles with density larger than that of the advecting fluid cluster and preferentially concentrate in different regions of the flow, due to the different responses of heavy particles to turbulent fluctuations. When the flow is

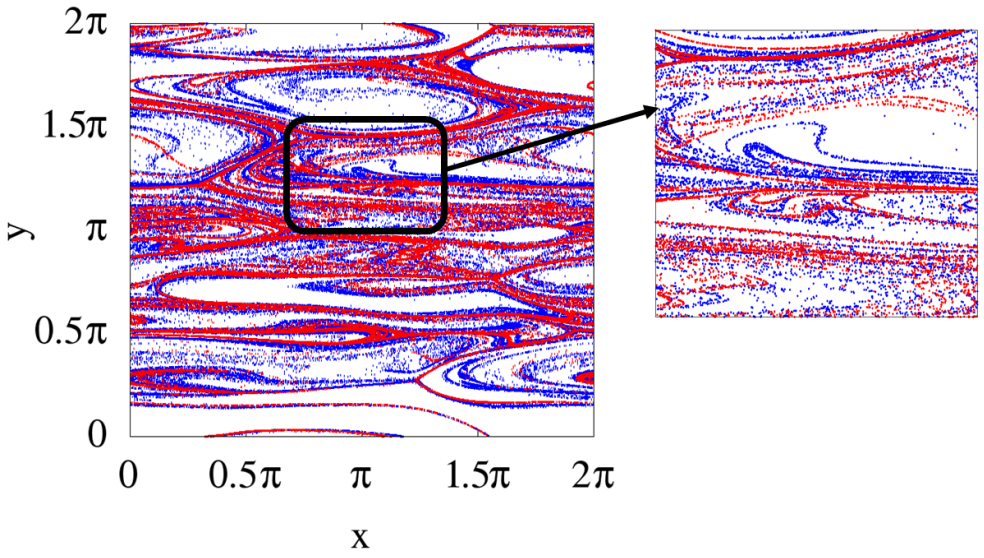

Figure 4.9: Particle distributions (blue dots) for $St = 0.468$ and (red dots) $St = 0.936$ at a fixed instant of time in statistically stationary conditions at $Wi = 19.1$ and $Re = 0.795$; the number of particles is $N_p = 10^4$.

seeded with particles of different inertia, the particles, depending on their inertia, concentrate in different flow structures. This leads to a segregation of the different particle types, which intuitively is characterized by some segregation length scale. An example of heavy inertial particle segregation is shown in Fig. 4.9, where snapshots of particle distributions with different inertias are depicted. From the qualitative point of view, the two particle distributions do not look very different at large scales, but have significant differences at smaller scales (as shown in the zoom of the main plot). Particle segregation in visco-elastic fluids has attracted much attention in the context of biomedical and biotechnology applications, where the separation of organic particles is very important for the early detection of diseases and their diagnosis [185–187]. Also, in other applications like mixing, heat transfer, hydraulic fracturing, droplet generation and sorting, the characterization of inertial particle segregation plays an important role.

The segregation length of the particle distributions depends on both the size and mass densities ($\rho_f \ll \rho_p$ (heavy inertial particles) or $\rho \gg \rho_p$ (light inertial particles)) of the corresponding inertial particles. However, in the present study we consider only heavy inertial particles (i.e. the density ρ_p is fixed), therefore the segregation length will depend only on the particle Stokes number St. There are some classical and natural observables to

quantify the particle segregation, such as, e.g. the minimal distance between different types of particles, the density correlation function, mixed pair correlation function and mixed radial distribution function [100, 188]. The disadvantages of these methods is the absence of robustness, as the results are highly dependent on the particle number densities and the quantitative effect of the coarse-graining scale (to define the Eulerian density fields) on the estimates. Therefore, the description of robust observables to measure segregation is definitely required.

This approach to segregation length is inspired by Kolmogorov's distance between two distributions [189] and is based on particle densities coarse-grained over a scale r, which can be understood as the resolution of a magnifying lens used to look at the distribution of particles. To quantify the segregation of the particles, we partitioned the whole area L_0^2 into $M(r) = (L_0/r)$ boxes. The segregation indicator is defined as follows [37]:

$$S_{St_1,St_2}(r) = \frac{1}{N_{pSt_1} + N_{pSt_2}} \sum_{i=1}^{M(r)} \left| {n_i}^{(St_1)} - {n_i}^{(St_2)} \right|. \tag{4.3}$$

The subscripts St_1 and St_2 represent the particle parameter, i.e. its Stokes number. The total number of particles of type St_j is given by N_{pSt_j}, while $n_i^{(St_j)}$ is the number of particles of a given type j contained in each box i.

In the following discussion, the case of $St_1 = St_2$ should be considered as taking independent realizations of the particle distribution so that S_{St_1,St_1} gives the minimum detectable segregation degree. Otherwise, computed on the same realization, such an indicator would give $S_{St_1,St_1} \equiv 0$. The segregation indicator $S_{St_1,St_2}(r)$ is a meaningful indicator only if it does not depend too severely on the total number of particles N_p, as shown in [37].

In Fig. 4.10 we plot $S_{St_1,St_2}(r)$ for distributions composed of heavy inertial particles with $St_1 = 0.016$ and heavy inertial particles with different St_2. The segregation indicator $S_{St_1,St_2}(r)$ has both upper and lower bounds, and can vary in the range $[0, 1]$. We first discuss the limiting cases.

- For small enough scales, i.e. $r \ll 1/\rho^{1/2}$, where r is the mean distance between particles of any type with the particle number density $\rho = N_p/L_0^2$, $S_{St_1,St_2} = 1$. This relation holds for any realization and means that two particle distributions are not overlapping when looked at with a resolution of r. This limiting case is clearly observed in Fig. 4.10.

- In contrast, when the scale r is of the order the size of the box L_0,

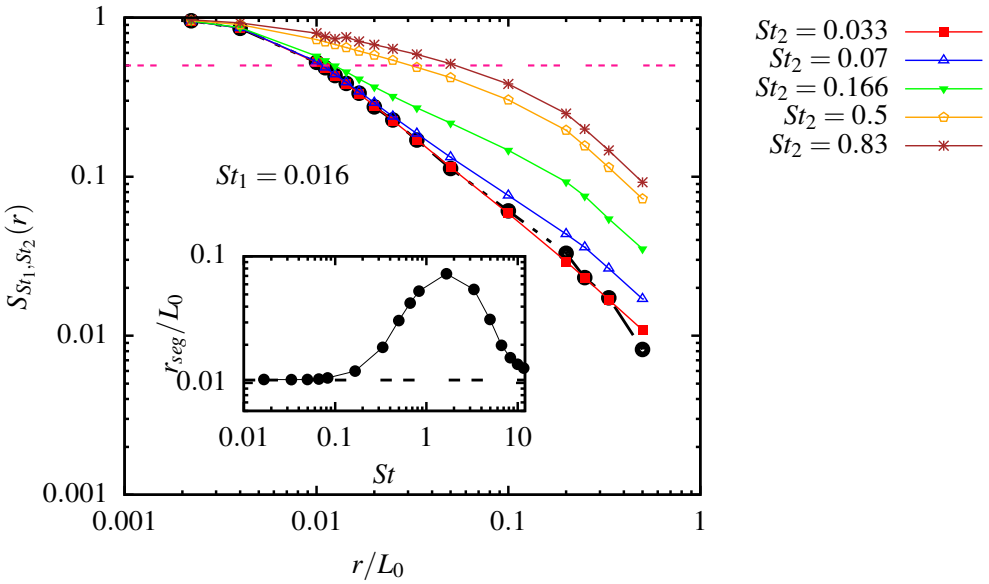

Figure 4.10: Segregation indicator $S_{St_1,St_2}(r)$ for $St_1 = 0.016$ and varying St_2, i.e. heavy inertial particle distribution with a given St_1 versus those having different St_2. From bottom to top: $St_2 = 0.033, 0.07, 0.166, 0.5, 0.83$. The black dashed line represents $S_{St_1,St_2}(r)$ for randomly distributed particles (computed from numerical simulations). Inset: r_{seg}/L_0 versus St_2 with r_{seg} defined as $S_{St_1,St_2}(r_{seg}) = 0.5$. The straight dashed line shows $r_{seg,h} \approx 0.01 L_0$.

the number of particles of two types looks the same, globally, i.e. $\lim_{r \to L_0} S_{St_1,St_2} = 0$.

The advantage offered by the segregation indicator is that it allows us to extract a segregation scale r_{seg}. This is done by fixing an arbitrary threshold value for S; we employed $S_{St_1,St_2}(r_{seg}) = 0.5$ [37]. With this definition we extract the value of r_{seg} for truly segregated pairs of two different classes of heavy inertial particles, shown in the inset of Fig. 4.10. From the main plot of Fig. 4.10 we observe that S_{St_1,St_2} increases with the difference between the two considered Stokes numbers, but $r_{seg} \approx r_{seg,d}$ (see dashed black line) for $St_2 < 0.08$ (see the inset of Fig. 4.10), where $r_{seg,d}$ is the mean inter-particle distance, computed from two different random distributions of the particles. This means that heavy inertial particles with $St_2 < 0.08$ and $St_1 = 0.016$ visit the same locations in the flow, irrespective of their inertia. Furthermore, a noticeable increase of r_{seg} is observed (Fig. 4.10, inset), and the maximal segregation length is obtained for heavy inertial particles of $St = 1$, where

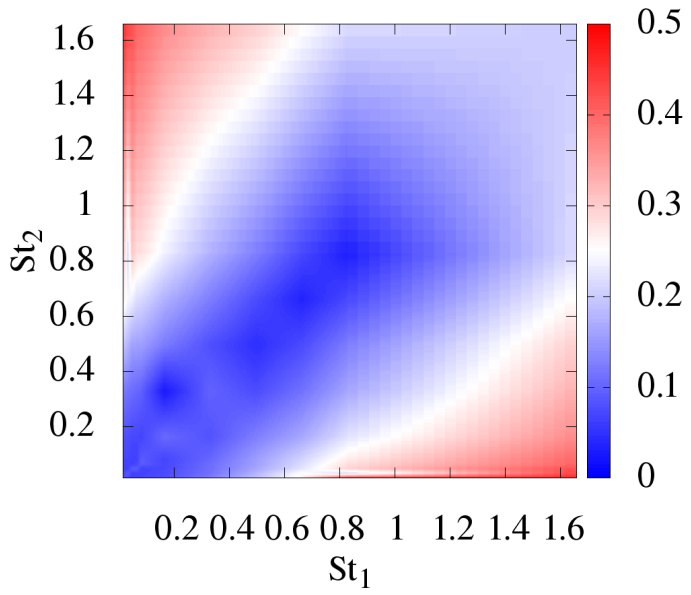

Figure 4.11: Segregation distance, r_{seg} between pairs of heavy inertial particle distributions with different Stokes numbers. The colour scale gives the intensity of r_{seg}. The simulations correspond to $Wi = 24.9$ and $Re = 0.619$.

$r_{seg} \approx 0.7L_0$. This is consistent with our expectations, because up to here, one type of particle (St_1) is quite close to being a Lagrangian tracer and from the previous analysis of D_2 and D_{KY} we know particles are highly concentrated for $St_2 \approx 1$.

We have further extended the study of segregation to several values of St_1. In Fig. 4.11 we show the value of the segregation scale r_{seg} by fixing St_1 for one type of heavy inertial particle and varying St_2 for another type of heavy inertial particle. The emerging picture is as follows. Particle pairs with $St_1 \approx St_2$ close to the diagonal have a segregation length close to the mean inter-particle distance, i.e. $r_{seg} \approx r_{seg,d}$, and this shows that the particles are poorly segregated. But as soon as the difference between the Stokes numbers becomes significant, i.e. outside the diagonal regions, the segregation length increases, i.e. $(r_{seg} > r_{seg,d})$. These results confirm the one shown in Fig. 4.10. The maximum segregation is observed when one of the two (either St_1 or St_2) is very small and the other is of the order $O(1)$, which means that the characteristic time scale of the flow $\tau_{\dot{\gamma}}$ is the best candidate for generating strong correlations between particle positions and flow struc-

ture, and consequently segregation.

4.6 Summary

In this chapter, we have analysed the small-scale properties of particle aggregation in an inhomogeneous 2D elastic turbulent flow. We have provided in detail the statistics of the flow and polymer regions explored by the particles. A strong correlation between the particle distribution and the polymer (square) elongation field was detected, with large particle concentrations occurring along thin highly elastic filamentary structures. Since the interaction between the polymers and the particles is not direct in the adopted model dynamics, but rather mediated by the fluid flow, we found that the well-known mechanism of vortex ejection is here at play and that, for the polymer statistics, corresponds to preferential particle concentration in the region where the polymers are highly stretched.

Also, we have found the presence of structures in the inertial particle distribution, and the structures are related to the presence of the typical timescale of our flow $\tau_{\dot{\gamma}}$. We have found that the geometry of inertial particle clusters in a developed elastic turbulence regime is controlled by the effective dissipative dynamics of the particle motion at small scales. The quantification of small-scale clustering is provided using the well-known correlation dimension D_2 and the Kaplan–Yorke dimension D_{KY}. Further, we introduced an indicator able to quantify the segregation degree and to allow the definition of a segregation length scale r_{seg} between different classes of particles.

The maximum small-scale clustering (in terms of the correlation dimension, Kaplan–Yorke dimension and segregation length) for heavy inertial particles is obtained for a Stokes number of around unity.

Chapter 5

Large-scale inhomogeneities of inertial particles in an elastic turbulent Kolmogorov flow

Contents

5.1 Introduction

In this chapter we investigate the large-scale properties of the spatial distribution of the particles in terms of the averaged profiles. It has been observed that large-scale inhomogeneities cannot be explained directly in terms of the averaged profiles: in fact, they are a manifestation of turbophoresis [151]. In a nutshell, this corresponds to the migration of inertial particles from regions of high eddy diffusivity to regions of low eddy diffusivity that occurs in turbulent flows with a non-homogeneous mean flow. Turbophoresis can be understood by analogy with thermophoresis [190–192]. Thermophoresis is the motion of Brownian particles governed by gradients in temperature [193], well understood within the framework of local thermodynamic equilibrium in statistical mechanics [192].

Turbophoresis has been mainly studied in wall-bounded flows, because of their relevance for industrial and environmental applications related to particle deposition [32, 151, 156]. Interestingly, using the three-dimensional

(3D) Newtonian turbulent Kolmogorov flow it was recently shown that turbophoretic segregation is independent of the presence of walls [34] (this was also confirmed in simulations employing a random inhomogeneous forcing [35]). Also in that case particles accumulate in regions of minimum turbulent diffusivity, but the spatial distribution of the latter with respect to the mean flow differs from the one found in geometrically confined flows [34]. All these works demonstrate that the regions of particle accumulation at large scales depend on the details of the flow.

This chapter mainly focusses on the effect of the spatial non-homogeneity of the elastic turbulent flow on the average local concentration of the particles. For the analysis of the numerical results, we took a statistical approach aimed at characterizing the mean particle concentration profiles, and at assessing their correlation with the mean turbulent-like fluctuations of the flow field, as a function of the particle inertia and for several values of the polymer elasticity.

5.2 Particle distribution and flow structures

To study the large-scale properties of the spatial distribution of the particles and to analyse how this is related to the features of the flow, we introduce the particle number density field $\rho(\boldsymbol{x}, t)$ and focus on the profiles along the direction of inhomogeneity y of both ρ and flow statistics.

The mean density profiles $\rho(y)$ along the direction of inhomogeneity of the flow correspond to averaging the particle number density fields $(\rho(\boldsymbol{x}, t))$ along the mean-flow direction x and time:

$$\langle\rho\rangle(y) = \frac{1}{L_0}\frac{1}{T}\int_0^T \int_0^{L_0} \rho(\boldsymbol{x}, t)\mathrm{d}x\mathrm{d}t. \tag{5.1}$$

Similarly to what is done for ρ, things are computed the same for the other considered quantities. Note that this type of averaging is related to the global one introduced in Chapter 3, see Eq. (3.34) by

$$\overline{(...)} = \frac{1}{L_0}\int_0^{L_0} \langle(...)\rangle dy.$$

Figure 5.1 presents the profiles of ρ (panel (a)) for three different Stokes numbers, as well as those of several flow related quantities (panels (b) and (c)), in a state of elastic turbulence (with $Wi = 23.9$ and $Re = 0.664$). All profiles are normalized by their global average value to stress the deviations from it. We remark that $\langle u_y\rangle(y) = 0$ with very good accuracy in the

numerics, as expected from symmetry considerations. We also note that the results shown were obtained by further averaging them over one forcing wavelength $\ell = LL_0 = \pi/2$. Comparing panels (a) and (b) of Fig. 5.1, we see that, consistently with the previous analysis (see Section 4.2) for the average Okubo–Weiss parameter $\overline{Q}$, the particles are most concentrated where the longitudinally averaged profile of the Okubo–Weiss parameter $\langle Q\rangle(y)$ is a minimum. Note that here $\langle Q\rangle(y)$ is normalized by $Q^{rms}_{St=0}$ due to the fact that $\overline{Q}_{St=0} = 0$. Nevertheless, in such regions of minimal $\langle Q\rangle(y)$, the profile of the trace of the conformation tensor $\langle tr(\boldsymbol{\sigma})\rangle(y)$ is now found to be a minimum too. This apparently contradicts the observation made in Section 4.2 that particles aggregate in regions of highly elongated polymers. This contradiction is resolved by taking into consideration the fact that the profiles result from a spatial averaging procedure. Indeed, all the information about the spatial structure along the longitudinal direction is lost in them, as they are functions of the transversal direction only. This particularly applies to the information about the extent of the vortices along x, from which the particles are expelled, and about the orientation, with respect to x, of the separatrices, by which the particles tend to be attracted and that collocate with high polymer elongation regions. While the profile $\langle Q\rangle(y)$ receives contributions only from the transverse fluctuating component of the velocity field, indeed $\langle Q\rangle(y) = -\partial_y^2\langle u_y'^2\rangle(y)$ (with prime indicating the fluctuation), the trace of the conformation tensor is dominated by the contribution of the mean flow, $\langle u_x\rangle(y)$, to polymer stretching and $\langle tr(\sigma)\rangle(y)/\overline{tr(\sigma)} \simeq \langle\sigma_{11}\rangle(y)/\overline{\sigma_{11}}$.

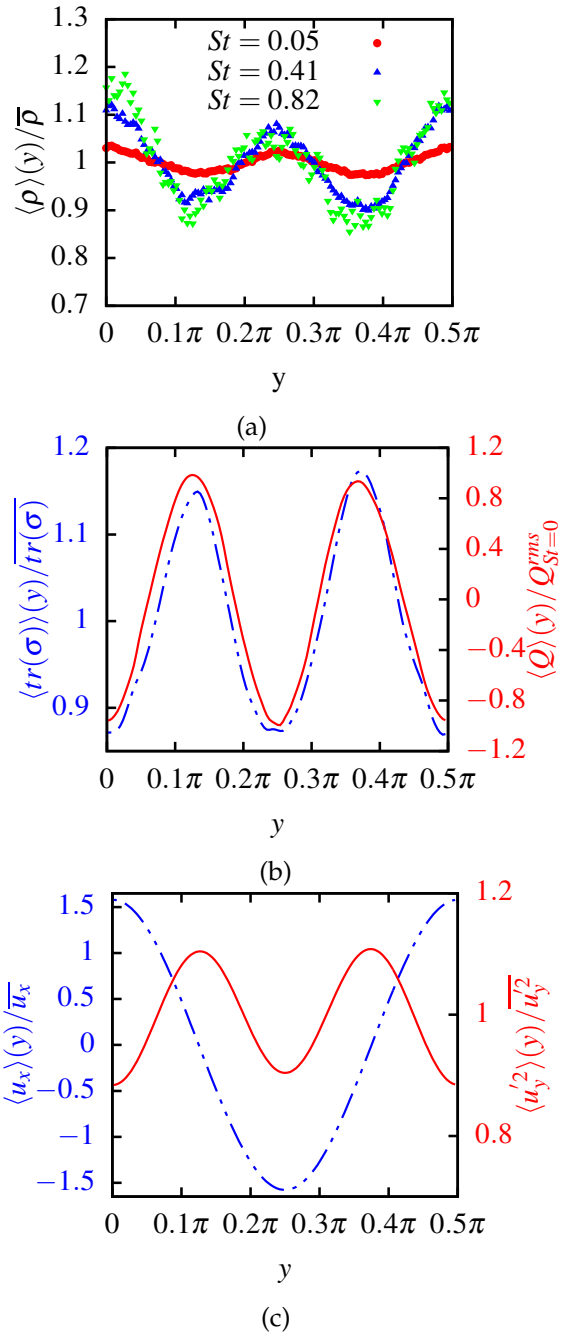

Figure 5.1: (a) Particle number density profiles $\langle\rho\rangle(y)/\overline{\rho}$, normalized by the global mean uniform density ($\overline{\rho} = 1/L_0$), for three different Stokes numbers. (b) Normalized profile of the trace of the conformation tensor $\langle(\boldsymbol{\sigma})\rangle(y)/\overline{tr(\boldsymbol{\sigma})}$ (blue dashed line, left axis) and of Okubo–Weiss parameter $\langle Q\rangle(y)/Q^{rms}_{St=0}$ (red solid line, right axis). (c) Normalized profiles of the longitudinal velocity $\langle u_x\rangle(y)/\overline{u_x}$, where $\overline{u_x} = U$, (dashed blue line, left axis) and of the fluctuations of the shear-normal kinetic energy $\langle u_y'^2\rangle(y)/\overline{u_y'^2}$ (red solid line, right axis) of the fluid flow. The plots in (a–c) refer to statistically stationary conditions for $Wi = 23.9, Re = 0.664$. All the profiles were further averaged over the wavelength defining the periodicity of the mean flow $\ell = LL_0 = \pi/2$.

5.3 Elastically driven turbophoresis

From the above discussion it should be clear that the large-scale inhomogeneities of ρ cannot be explained directly in terms of the averaged profiles of $\boldsymbol{\sigma}$ or $\boldsymbol{u}$. In fact, they are a manifestation of the turbophoresis phenomenon related to the fluctuation profiles of the velocity (a second order statistical quantity).

As in the previous section, we found modulations of the density profiles that vary sinusoidally, with a periodicity twice that of the mean flow. We tried to fit these density profiles with a sinusoidal fitting function Eq. (5.2), which has been recently suggested by De Lillo and coworkers [34], Fig. 5.2 clearly shows that a sinusoidal function can closely fit the averaged density profiles and the periodicity seems to be well captured.

$$f(y) = (1 + a(St)cos(\frac{2y}{L})) \tag{5.2}$$

Here, $a(St)$ is a free parameter, which accounts for the dependence on the particle inertia.

5.3.1 Theoretical modelling of turbophoresis

In order to make our analysis more quantitative and to understand the correlation between the regions of high concentration and the mean flow, let us start by recalling the theoretical predictions for the dynamics of inertial particles in turbulence. The theoretical understanding of turbophoresis relies on statistical approaches. The models available in the literature are typically derived either from the Fokker–Planck equation obeyed by the probability density to find a particle at position $\boldsymbol{x}$ with velocity $\boldsymbol{v}$ at time t (as in [194]), or on the application of a decomposition into mean and fluctuating components, in the spirit of Reynolds averaging, in fluid momentum and particle mass conservation equations (as in [151]). Here we follow the second approach which, in spite of its more heuristic character, is perhaps more physically transparent. After the appropriate correspondence is made, both models provide the same results in what concerns the present discussion. We then write $g(\boldsymbol{x}, t) = \langle g \rangle(y) + g'(\boldsymbol{x}, t)$ for each field quantity of interest $g(\boldsymbol{x}, t)$, where the prime indicates the fluctuation. Defining as $\boldsymbol{J} = \rho \boldsymbol{v}$ the flux associated with the number density of particles, we have

$$\langle J_y \rangle(y) = \langle \rho \rangle(y) \langle v_y \rangle(y) + \langle \rho' v'_y \rangle(y) \tag{5.3}$$

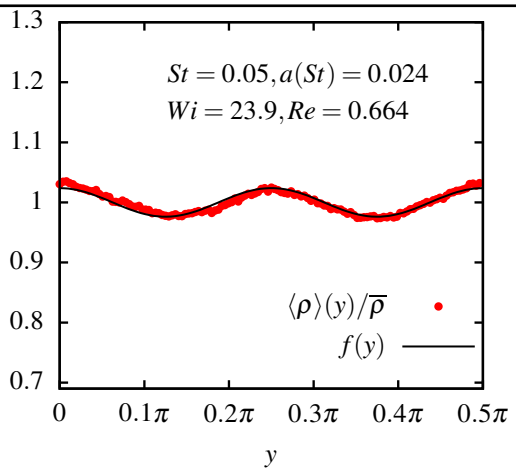

(a)

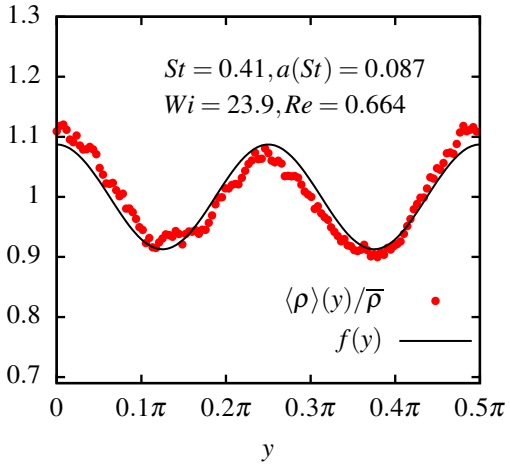

(b)

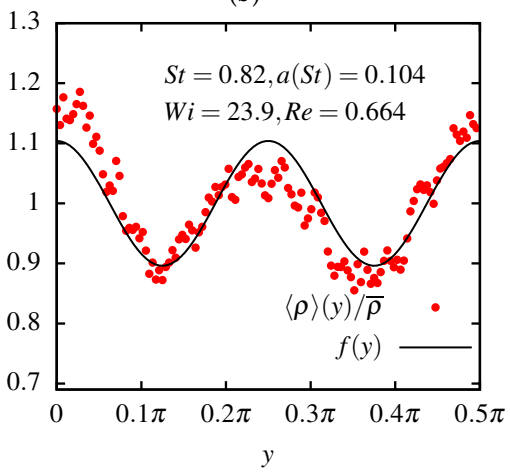

(c)

Figure 5.2: Comparison of normalized particle number density profiles $\langle\rho\rangle(y)/\overline{\rho}$ (red points) with fitting function Eq. (5.2) (black solid line) for $Wi = 23.9, Re = 0.664$ and different values of St (increasing from top to bottom). The values of the a obtained from the best fit are $a = 0.024$ (a), $a = 0.087$ (b), $a = 0.104$ (c). All the particle density profiles were further averaged over the wavelength defining the periodicity of the mean flow $\ell = LL_0 = \pi/2$.

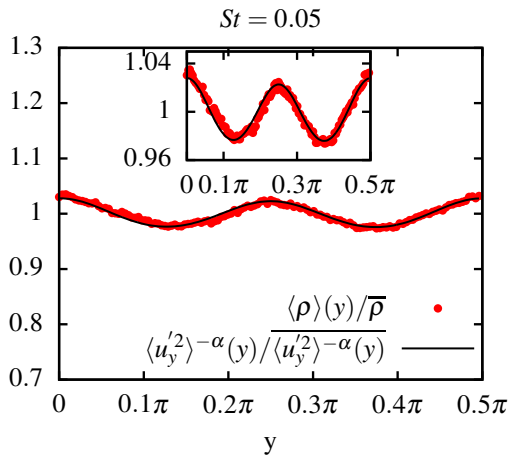

(a)

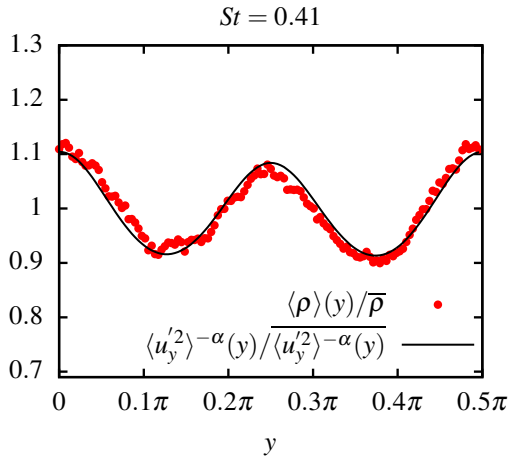

(b)

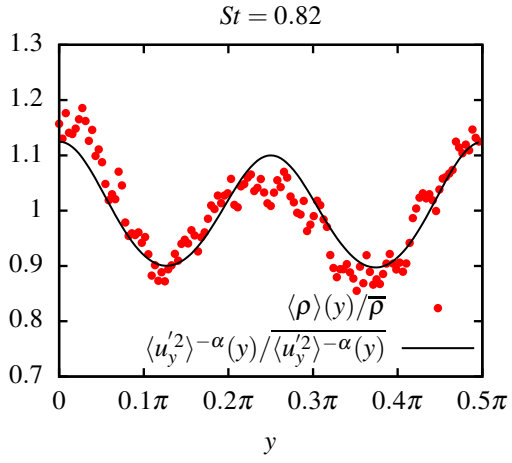

(c)

Figure 5.3: Comparison of normalized particle number density profiles $\langle\rho\rangle(y)/\overline{\rho}$ (red points) with the normalized profiles of transversal velocity fluctuations $\langle u_y'^2\rangle^{-\alpha}(y)/\overline{\langle u_y'^2\rangle^{-\alpha}(y)}$ (black solid line) for $Wi = 23.9, Re = 0.664$ and different values of St (increasing from top to bottom). The values of the exponents obtained from the best fit are $\alpha = 0.229$ (a), $\alpha = 0.839$ (b), $\alpha = 1$ (c). The inset in (a) is a zoom around $\langle\rho\rangle(y)/\overline{\rho} = 1$. All the profiles were further averaged over the wavelength defining the periodicity of the mean flow $\ell = LL_0 = \pi/2$.

for its component in the direction of inhomogeneity y. As is often done [151, 153], we adopt a gradient diffusion model for the second term on the right-hand side of Eq. (5.3):

$$\langle \rho' v'_y \rangle(y) = -D_p \frac{d}{dy} \langle \rho \rangle(y), \tag{5.4}$$

where D_p is the diffusion coefficient of the inertial particles. This is typically assumed to be close to that of fluid tracers (i.e. the eddy diffusion coefficient) D_f, which is completely justified only in the limit of vanishingly small Stokes number. Estimating D_f dimensionally, one has

$$D_p \approx D_f \approx \tau_c \langle u'^2_y \rangle(y), \tag{5.5}$$

where τ_c is a correlation time associated with the fluid flow. We expect it to be proportional to $\tau_{\dot{\gamma}}$ (Eq. (2.5)), so that $\tau_{\dot{\gamma}}/\tau_c = a$ with a some constant of order 1. Still in the limit of $\tau_p \to 0$, using $\boldsymbol{v} \simeq \boldsymbol{u} - \tau_p(\partial_t \boldsymbol{u} + \boldsymbol{u} \cdot \boldsymbol{\nabla} \boldsymbol{u})$, the turbophoretic velocity in Eq. (5.3) can be expressed as

$$\langle v_y \rangle(y) = -\tau_p \frac{d}{dy} \langle u'^2_y \rangle(y). \tag{5.6}$$

Inserting Eqs (5.4—5.6) into Eq. (5.3), for the fluxless steady state (i.e. $\langle J_y \rangle(y) = 0$), we finally obtain

$$\langle \rho \rangle(y) \sim \langle u'^2_y \rangle^{-\alpha}(y), \tag{5.7}$$

giving the relation between the inhomogeneities of the particle distribution and those of the fluid velocity fluctuations. In this expression, the exponent $\alpha = \tau_p/\tau_c = aSt$ controls the amplitude and shape of the spatial modulation of the particle density transversal profile.

The numerical results, shown in Fig. 5.3, are in quite good agreement with the expectation from Eq. (5.7), providing quantitative support to the claim that the large-scale inhomogeneities of the particle distribution are controlled by a turbophoretic mechanism. The small asymmetries observable in $\langle \rho \rangle(y)$ are due to the very slow convergence of the particle statistics. As in Fig. 5.1, the results shown here were obtained by further averaging the profiles over one forcing wavelength. The exponent α, measured by a least squares fitting procedure, is found to increase with the Stokes number and to approach $\alpha \simeq 1$ for $St \approx 1$ or larger (Fig. 5.4). The growth of α with St means that the amplitude of the large-scale modulations of $\langle \rho \rangle(y)$, and hence the importance of turbophoresis, grows with increasing particle

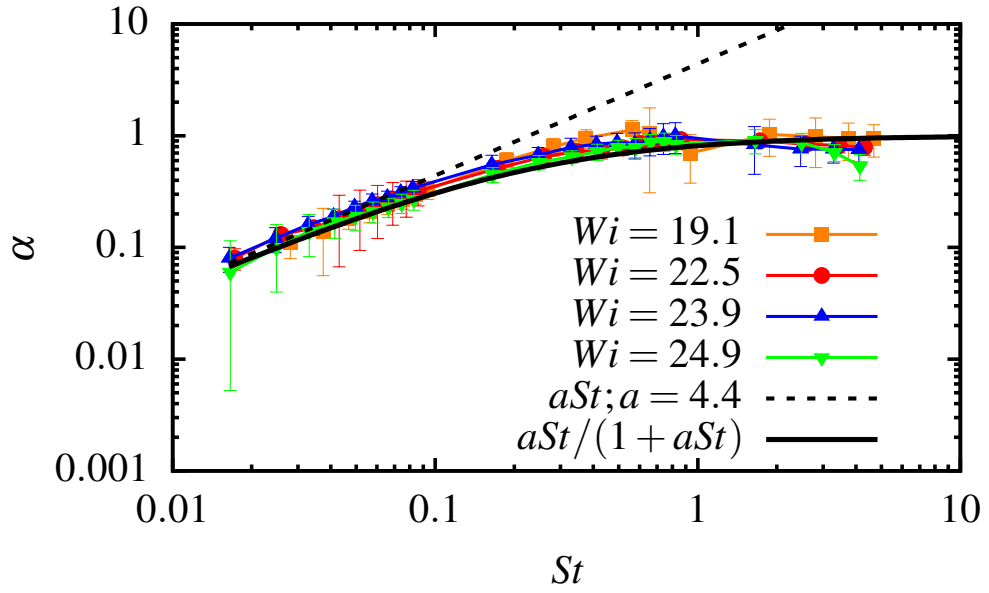

Figure 5.4: Exponent α as a function of St and for different Weissenberg numbers. The black dashed line represents the linear prediction in the limit of small St. The black solid line represents the modified non-linear prediction; $a = 4.4$ is obtained from the best fit.

inertia. For the smallest values of St, α is found to linearly grow with St, with a value of the fitted proportionality constant $a = 4.4$ (see the dashed black line in Fig. 5.4). Hence, in this range of small particle inertia, the numerical results are commensurate with the model prediction $\alpha \sim St$ valid in the limit of vanishingly small St. For larger St, the data are no longer described by this linear relation, with α tending to saturate to 1. To account for this behaviour, we follow [151] and [195], where it was suggested that the shear-normal particle kinetic energy is different from the fluid one, being proportional to it by a constant κ that depends on St. The turbophoretic velocity in Eq. (5.6) should then be modified as follows:

$$\langle v_y \rangle(y) = -\kappa \tau_p \frac{d}{dy} \langle u_y'^2 \rangle(y), \tag{5.8}$$

where $\kappa = 1/(1 + \tau_p/\tau_c)$ [151,194]. Reasoning as before, we obtain a fluxless steady solution like the one in Eq. (5.7) but with

$$\alpha = \frac{aSt}{1 + aSt}. \tag{5.9}$$

Note that, from this, $\alpha \simeq aSt$ for $St \simeq 0$ and $\alpha \to 1$ for very large St. This modified dependence on the Stokes number captures quite well the

behaviour of the exponent α in a considerably broader range of St extending to unity and beyond, as shown in Fig. 5.4 (solid black line, with $a = 4.4$ as for the linear behaviour). For even larger values of St, we were unable to obtain particle statistics that converged satisfactorily. We note that these results depend weakly on Wi. To quantitatively assess the overall intensity of the turbophoresis, as in [34], we measure the rms relative deviation of the mean particle density profile $\langle\rho\rangle(y)$ from the uniform distribution $\overline{\rho} = 1/L_0$, defined as

$$\chi \equiv \frac{\sigma_{\langle\rho\rangle(y)}}{\overline{\rho}} = \left[\frac{1}{L_0}\int_0^{L_0}\left(1 - \frac{\langle\rho\rangle(y)}{\overline{\rho}}\right)^2 dy\right]^{\frac{1}{2}}, \tag{5.10}$$

where $\sigma_{\langle\rho\rangle(y)}$ is the standard deviation of $\langle\rho\rangle(y)$. The global parameter χ as a function of St for different Wi is presented in Fig. 5.5. Consistently with the behaviour of α, we find that χ grows with St and eventually reaches an approximately constant value for $St \geq 1$. In the limit as $St \to \infty$, we would expect χ to be a decreasing function of St, due to the fact that, practically, very heavy particles should not interact with the flow field. However, this point could not be verified within this study, due to the difficulty of attaining density profiles that converged well for large enough Stokes numbers. The approximately constant behaviour of χ for $St \geq 1$ appears nevertheless reasonable from its definition, considering that in the same range of Stokes numbers the exponent α characterizing $\langle\rho\rangle(y)$ is at a plateau value.

Finally, we observe that χ displays some dependence on Wi, which becomes more evident as St increases. Indeed, as seen from Fig. 5.5, χ decreases with increasing Wi, suggesting that the large-scale accumulation of particles (quantified by χ) decreases with increasing polymer elasticity. This trend can be possibly connected to the changes in $\langle u_y'^2\rangle(y)$ at growing Wi, which correspond to an increase of its mean accompanied by a weak reduction of its peak-to-peak excursions. Indeed, if we focus on the region $St = O(1)$ where the effect of varying Wi is most important, and we replace $\langle\rho\rangle(y)$ with $\langle u_y'^2\rangle^{-1}(y)$ (note that $\alpha \simeq 1$ for $St = O(1)$) in the expression for χ, we then should have a decrease of its plateau value with Wi. As shown in the inset of Fig. 5.5, the computation of $\chi_{\langle u_y'^2\rangle^{-1}}$, i.e. the one based on $\langle u_y'^2\rangle^{-1}(y)$, confirms this expectation.

5.4 Summary

In this chapter we have shown the results for the large-scale properties of the particle aggregation obtained from numerical simulations of inertial

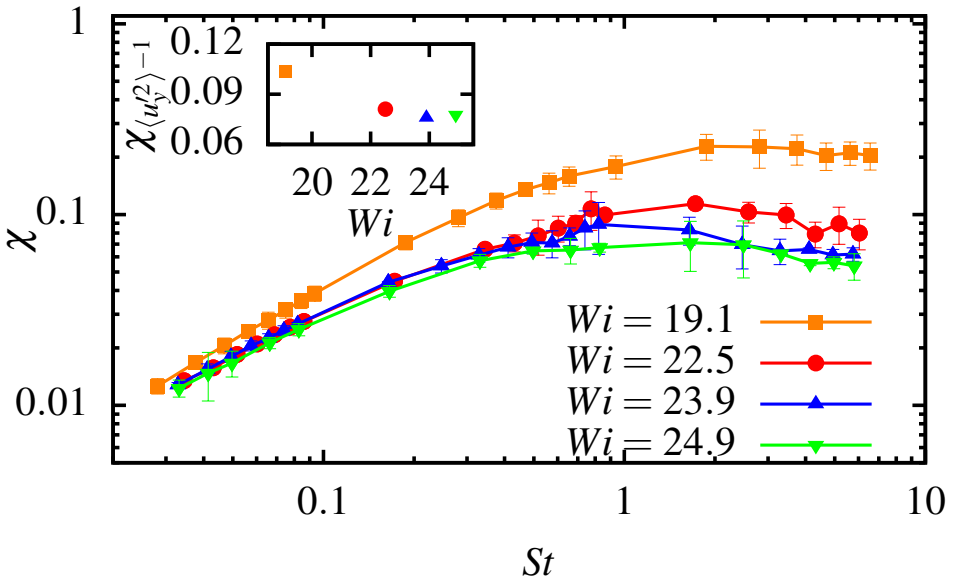

Figure 5.5: Root-mean-square (rms) relative deviation χ of $\langle\rho\rangle$ from the mean uniform distribution $\overline{\rho}$ as a function of St and for different Weissenberg numbers. Here, temporal averages were performed over 80 independent realizations corresponding to different instants of time separated by an interval larger than the typical flow time scale. The inset shows the parameter $\chi_{\langle u_y'^2\rangle^{-1}}$ computed from the rms relative deviation of $\langle u_y'^2\rangle^{-1}$ from the mean uniform value $\overline{\langle u_y'^2\rangle^{-1}}$, i.e. $\sigma_{\langle u_y'^2\rangle^{-1}}/\overline{\langle u_y'^2\rangle^{-1}}$, as a function of Wi.

(heavy) particle dynamics in a two-dimensional inhomogeneous viscoelastic Kolmogorov flow. Our findings reveal that at larger scales, the particle distribution is strongly related to the mean turbulent-like structures of the flow.

It has been found that the large-scale particle distribution has a maximum in correspondence with the minima of both the averaged parameter $\langle Q\rangle(y)$ and $\langle tr(\boldsymbol{\sigma})\rangle(y)$, in sharp contrast with the analogous finding for the location of the maximum particle accumulation at small scale found from instantaneous imaging.

This large-scale modulation of the particle distribution along the shear direction is caused by the periodic distribution of fluctuations of the shear-normal kinetic energy (averaged along the stream direction x and in time t).

Thus, the large-scale inhomogeneity of the spatial distribution of the par-

ticles is interpreted as the result of a turbophoretic mechanism: the accumulation of particles at minima of turbulent diffusivity. Remarkably, this phenomenon can then also occur in elastic turbulence, due to the significance of the fluctuations in the fluid velocity. Moreover, we have provided a theoretical model that allows quantitatively explaining the observed inhomogeneous mean particle distribution at large scales, for a broad range of values of St.

Chapter 6

Conclusions and Perspectives

6.1 Conclusions

The present study has aimed at investigating the yet unexplored situation of the dispersion of inertial particles in visco-elastic fluids under conditions of elastic turbulence [21, 90], *i.e.* of vanishing Reynolds number and high Weissenberg numbers, using numerical and statistical tools.

In order to obtain elastic turbulent flows, we considered a bi-dimensional flow with periodic boundary conditions. The chosen setup, corresponding to an Oldroyd-B fluid forced by a sinusoidal shear (Kolmogorov) flow, has proven useful to reproduce the main phenomenological features of elastic turbulence.

In the context of the dynamics of individual particles, Lagrangian statistics have been identified as the key quantities for understanding the underlying coupling with the carrier flow. A detailed (qualitative and quantitative) analysis of the effect of the particle inertia on the behaviour of the different clustering measures has been addressed, showing that particles with both small and large particle Stokes numbers tend to follow an uniform distribution filling the full 2D space. On the other hand, particles with Stokes numbers around unity tend to preferentially accumulate in certain regions of the flow field. We found a strong correlation between the instantaneous locations of the particles and the polymer elongation field, with large particle concentrations occurring along thin highly stretched polymeric structures. Since the interaction between the polymers and particles is not direct in the adopted models, but rather mediated by the fluid flow, it has been possible to interpret such a phenomenon in terms of the preferential concentration of particles outside elliptical regions (vortices, in short), in strain dominated regions. It ends up being that the strain dominant regions coincide with those wherein the polymers are effectively stretched.
We have further analysed the small scale behaviour of the system, in terms of the fractal dimension of the particle dynamics attractor. Firstly, the geometrical features in physical space of small-scale clustering were addressed,

measuring the correlation dimension of the fractal sets in which the particles accumulate, i.e. the scaling exponent of the probability density to find particle pairs at small distances. The analysis revealed particularly effective clustering for Stokes numbers of order unity, for which the correlation dimension decreases to approximately 1, pointing to the aggregation of particles on almost one-dimensional structures (filaments). We have also used another tool commonly used for dissipative dynamical systems, namely, the Kaplan–Yorke dimension, to perform a detailed characterization of the particle distribution in position–velocity phase space. The detailed analysis has shown that for small values of St, the first two Lyapunov exponents control the exponential growth rate of physical ($2D$) volumes and the last two Lyapunov exponents are close to $\lambda_3 \approx \lambda_4 \sim -1/\tau_p$, thus quantifying the rate of adjustment of the Lagrangian velocity to the Eulerian one. All of these results are found to be in qualitative agreement with the ones observed in smooth random flows, and in 3D turbulent flows [36, 39, 115, 181]. All the considered statistical indicators display only rather weak dependences on the Weissenberg number in the range of parameters we have explored.
At large scales, a turbophoretic mechanism associated with the gradients of the intensity of the turbulence, which can also be expressed in terms of a spatially dependent eddy diffusivity, was found to be responsible for the segregation, as in Newtonian fluids at high Reynolds numbers [32–35]. To describe the kind of large-scale inhomogeneity which characterizes the distributions of the particles we, therefore, focused on the density profiles of the particle distribution along the direction of the inhomogeneity of the flow. Furthermore, in the considered inhomogeneous elastic turbulence setting, the spatial distribution of the particles has maxima that correspond with the minima of the (elastic) turbulence velocity fluctuations. A detailed analysis allowed us to measure the exponent characterizing the relation between the mean particle density profile and the turbulence intensity within the direction transversal to the mean flow. In a way different from the case of the 3D Newtonian turbulent Kolmogorov flow, this exponent was found to depend on the particle inertia, i.e. on the Stokes number. Such a dependence turned out to be non-linear in St and could be explained by adapting previous theoretical approaches [151, 194] to construct a predictive model by means of a Reynolds averaging procedure. A similar non-linear dependence is also seen in the overall intensity of the turbophoresis phenomenon, quantified by using the global parameter χ accounting for the rms deviation of the particle distribution, relative to the uniform one. This quantity shows a decreasing dependence on the Weissenberg number, suggesting a reduc-

tion of the segregation for larger values of Wi. This behaviour is possibly associated with the progressively (with growing Wi) homogeneous character of the transversal fluid velocity fluctuations.

6.2 Perspectives

We have already mentioned some of the drawbacks of the Oldroyd-B model in Chapter 1. One of them has been regarded as particularly unphysical: the lack of a limit to the maximum accessible elongation. Indeed, the Oldroyd-B model is only valid in the limit of small elongations, but one would like to use it even for the dynamical states where extreme stretching ought to take place. To overcome this limitation, it has been proposed to use a non-linear restoring force that imposes a maximal polymer elongation and is able to reproduce some more realistic features of polymer solutions (such as finite extensional viscosity and shear thinning) that the Oldroyd-B model does not take into account. This is called the FENE-P model.
Kolmogorov flow has been shown to be useful for assessing some of the properties of elastic turbulence, and it can be used again in the future, in combination with other rheological models, such as FENE-P, to further investigate the Eulerian and Lagrangian properties of elastic turbulence, and in particular to address still currently open issues concerning scaling intermittent properties of this peculiar flow state. To achieve this, we have, as a first step, started some simulations by implementing the FENE-P model in our two-dimensional pseudo-spectral code. Some interesting perspectives have emerged, which are still under investigation. Simulations have been performed for a wide range of Weissenberg numbers to obtain a database that, it is hoped, will shed light on the dependence of flow instability, turbulent-like structures, and mixing properties on the additional parameter introduced by employing the FENE-P model, which is L_{max}, the maximum extension of the polymer molecule. The main question to be addressed numerically is how does the instability diagram of a polymer solution depend on L_{max}, and how does it differ significantly from that of the Oldroyd-B model (where $L_{max} \to \infty$). The above considerations raise the question of whether the power-law form of the kinetic energy spectrum is universal for the changes in the mechanical properties of the polymer model. In particular, we will focus on the spectra of the polymer energy and on the modification of the dissipation scale through the presence of additional flow parameter L_{max}.

Moreover, it is known that linear elasticity models, such as Oldroyd-B, can underestimate the experimentally measured elastic stresses [196]. Furthermore, the effect of the latter on the particle dynamics might not be unimportant. In particular, rheological models accounting for shear-dependent viscosity effects (such as FENE models) could bring in additional dynamical couplings between the flow and the particles [40]. One could indeed expect that, e.g. in a shear-thinning fluid, the varying effective viscosity would reduce the drag force experienced by the particles in the regions of the flow where the polymers are maximally stretched, and this might in turn affect the particle unmixing properties. This is a subject that deserves future investigation in order to assess to what extent the phenomenology described in this thesis would apply.

In a broader context, apart from adopting the FENE-P model, this study could be extended in other directions as well. In this thesis we have only investigated the case of impurities which are much heavier than the fluid, but it would be interesting to see what happens when the mass density contrast is changed, a condition where the added mass force has a role. In a recent paper, De Lillo, Boffetta and Musacchio [39] investigated the effects of polymer additives on small-scale clustering of heavy and light inertial particles in homogeneous isotropic turbulence. They have shown that depending on the particle and flow parameters (namely the particle relaxation time, fluid particle density ratio and the polymer relaxation time), the clustering of the polymer can either increase or decrease. Through the effects of the polymers on the particles, the Lyapunov exponents for light particles are observed to behave qualitatively differently from those for heavy particles. Hence, it is most probably interesting to understand whether bubbles have a distinct behaviour from that of the significantly heavy inertial particles in fully developed elastic turbulence regime, both at small and large scales, and if so, then the quantification of their segregation properties could be interesting for mixing applications.

Bibliography

[1] A. D. Stroock, S. K. W. Dertinger, A. Ajdari, I. Mezić, H. A. Stone, and G. M. Whitesides, "Chaotic mixer for microchannels," *Science*, vol. 295, no. 5555, pp. 647–651, 2002. (Cited on page 3.)

[2] C. Y. Lee and L. M. Fu, "Recent advances and applications of micromixers," *Sens. Actuators B Chem.*, 2017. (Cited on page 3.)

[3] D. M. Roberge, L. Ducry, N. Bieler, P. Cretton, and B. Zimmermann, "A revolution for the fine chemical and pharmaceutical industries," *Chem. Eng. Technol.*, vol. 28, no. 3, pp. 318–323, 2005. (Cited on page 3.)

[4] J. D. Tice, H. Song, A. D. Lyon, and R. F. Ismagilov, "Formation of droplets and mixing in multiphase microfluidics at low values of the Reynolds and the capillary numbers," *Langmuir*, vol. 19, no. 22, pp. 9127–9133, 2003. (Cited on page 3.)

[5] C. Y. Lee, C. L. Chang, Y. N. Wang, and L. M. Fu, "Microfluidic mixing: a review," *Int. J. Mol. Sci.*, vol. 12, no. 5, pp. 3263–3287, 2011. (Cited on page 3.)

[6] B. Traore, C. Castelain, and T. Burghelea, "Efficient heat transfer in a regime of elastic turbulence," *J. Non-Newtonian Fluid Mech.*, vol. 223, pp. 62–76, 2015. (Cited on pages 3, 4 and 46.)

[7] W. M. Abed, R. D. Whalley, D. J. C. Dennis, and R. J. Poole, "Experimental investigation of the impact of elastic turbulence on heat transfer in a serpentine channel," *J. Non-Newtonian Fluid Mech.*, vol. 231, pp. 68–78, 2016. (Cited on pages 3, 4 and 46.)

[8] D. Y. Li, X. B. Li, H. N. Zhang, F. C. Li, S. Qian, and S. W. Joo, "Efficient heat transfer enhancement by elastic turbulence with polymer solution in a curved microchannel," *Microfluidics and Nanofluidics*, vol. 21, no. 1, p. 10, 2017. (Cited on pages 3 and 18.)

[9] Y. Ye, G. Chiogna, O. A. Cirpka, P. Grathwohl, and M. Rolle, "Experimental investigation of transverse mixing in porous media under helical flow conditions," *Phys. Rev. E*, vol. 94, no. 1, p. 013113, 2016. (Cited on page 3.)

[10] J. Cai, W. Wei, X. Hu, R. Liu, and J. Wang, "Fractal characterization of dynamic fracture network extension in porous media," *Fractals*, vol. 25, no. 02, p. 1750023, 2017. (Cited on page 3.)

[11] T. M. Squires and S. R. Quake, "Microfluidics: Fluid physics at the nanoliter scale," *Rev. Mod. Phys.*, vol. 77, no. 3, p. 977, 2005. (Cited on page 3.)

[12] J. M. Ottino and D. V. Khakhar, "Mixing and segregation of granular materials," *Annu. Rev. Fluid Mech.*, vol. 32, no. 1, pp. 55–91, 2000. (Cited on page 3.)

[13] P. E. Dimotakis, "Turbulent mixing," *Annu. Rev. Fluid Mech.*, vol. 37, no. 1, pp. 329–356, 2005. (Cited on page 3.)

[14] M. J. Madou, *Fundamentals of microfabrication: the science of miniaturization*. CRC press, 2002. (Cited on page 3.)

[15] H. A. Stone, A. D. Stroock, and A. Ajdari, "Engineering flows in small devices: microfluidics toward a lab-on-a-chip," *Annu. Rev. Fluid Mech.*, vol. 36, pp. 381–411, 2004. (Cited on page 3.)

[16] N. T. Nguyen and Z. Wu, "Micromixersâa review," *J. Micromech. Microeng.*, vol. 15, no. 2, p. R1, 2004. (Cited on page 3.)

[17] M. S. N. Oliveira, M. A. Alves, and F. T. Pinho, "Microfluidic flows of viscoelastic fluids," *Transport and Mixing in Laminar Flows: From Microfluidics to Oceanic Currents*, pp. 131–174, 2011. (Cited on page 3.)

[18] T. Burghelea, E. Segre, I. Bar-Joseph, A. Groisman, and V. Steinberg, "Chaotic flow and efficient mixing in a microchannel with a polymer solution," *Phys. Rev. E*, vol. 69, no. 6, p. 066305, 2004. (Cited on pages 3, 18, 20, 22, 46 and 69.)

[19] H. Nguyen and D. V. Boger, "The kinematics and stability of die entry flows," *J. Non-Newtonian Fluid Mech.*, vol. 5, pp. 353–368, 1979. (Cited on page 3.)

[20] J. A. Pathak, D. Ross, and K. B. Migler, "Elastic flow instability, curved streamlines, and mixing in microfluidic flows," *Phys. Fluids*, vol. 16, no. 11, pp. 4028–4034, 2004. (Cited on page 3.)

[21] A. Groisman and V. Steinberg, "Elastic turbulence in a polymer solution flow," *Nature*, vol. 405, no. 6782, p. 53, 2000. (Cited on pages 3, 4, 18, 19, 20, 65 and 107.)

[22] A. Groisman and V. Steinberg, "Efficient mixing at low Reynolds numbers using polymer additives," *Nature*, vol. 410, no. 6831, p. 905, 2001. (Cited on pages 3, 4, 22, 25 and 69.)

[23] T. Burghelea, E. Segre, and V. Steinberg, "Statistics of particle pair separations in the elastic turbulent flow of a dilute polymer solution," *Europhys. Lett.*, vol. 68, no. 4, p. 529, 2004. (Cited on pages 3, 18 and 21.)

[24] H. Y. Gan, Y. C. Lam, and N. T. Nguyen, "Polymer-based device for efficient mixing of viscoelastic fluids," *Appl. Phys. Lett*, vol. 88, no. 22, p. 224103, 2006. (Cited on page 3.)

[25] A. Groisman and V. Steinberg, "Elastic turbulence in curvilinear flows of polymer solutions," *New J. Phys.*, vol. 6, no. 1, p. 29, 2004. (Cited on pages 4 and 19.)

[26] L. Pan, A. Morozov, C. Wagner, and P. E. Arratia, "Nonlinear elastic instability in channel flows at low Reynolds numbers," *Phys. Rev. Lett.*, vol. 110, no. 17, p. 174502, 2013. (Cited on pages 4, 21 and 22.)

[27] A. Souliès, J. Aubril, C. Castelain, and T. Burghelea, "Characterisation of elastic turbulence in a serpentine micro-channel," *Phy. Fluids*, vol. 29, no. 8, p. 083102, 2017. (Cited on pages 4, 21 and 22.)

[28] P. C. Sousa, F. T. Pinho, and M. A. Alves, "Purely-elastic flow instabilities and elastic turbulence in microfluidic cross-slot devices," *Soft matter*, vol. 14, no. 8, pp. 1344–1354, 2018. (Cited on pages 4 and 22.)

[29] R. J. Poole, B. Budhiraja, A. R. Cain, and P. A. Scott, "Emulsification using elastic turbulence," *J. Non-Newtonian Fluid Mech.*, vol. 177, pp. 15–18, 2012. (Cited on pages 4 and 46.)

[30] J. Mitchell, K. Lyons, A. M. Howe, and A. Clarke, "Viscoelastic polymer flows and elastic turbulence in three-dimensional porous structures," *Soft Matter*, vol. 12, no. 2, pp. 460–468, 2016. (Cited on page 4.)

[31] K. D. Squires and J. K. Eaton, "Preferential concentration of particles by turbulence," *Phys. Fluids A*, vol. 3, no. 5, pp. 1169–1178, 1991. (Cited on pages 4 and 35.)

[32] F. Picano, G. Sardina, and C. M. Casciola, "Spatial development of particle-laden turbulent pipe flow," *Phys. Fluids*, vol. 21, no. 9, p. 093305, 2009. (Cited on pages 4, 44, 95 and 108.)

[33] G. Sardina, P. Schlatter, L. Brandt, F. Picano, and C. M. Casciola, "Wall accumulation and spatial localization in particle-laden wall flows," *J. Fluid Mech.*, vol. 699, pp. 50–78, 2012. (Cited on pages 4, 43 and 108.)

[34] F. De Lillo, M. Cencini, S. Musacchio, and G. Boffetta, "Clustering and turbophoresis in a shear flow without walls," *Phys. Fluids*, vol. 28, p. 035104, Mar. 2016. (Cited on pages 4, 44, 67, 96, 99, 104 and 108.)

[35] D. Mitra, N. E. L. Haugen, and I. Rogachevskii, "Turbophoresis in forced inhomogeneous turbulence," *Eur. Phys. J. Plus*, vol. 133, p. 35, 2018. (Cited on pages 4, 44, 96 and 108.)

[36] J. Bec, "Fractal clustering of inertial particles in random flows," *Phys. Fluids*, vol. 15, no. 11, pp. L81–L84, 2003. (Cited on pages 4, 33, 37, 41, 76, 82, 83, 87 and 108.)

[37] E. Calzavarini, M. Kerscher, D. Lohse, and F. Toschi, "Dimensionality and morphology of particle and bubble clusters in turbulent flow," *J. Fluid Mech.*, vol. 607, pp. 13–24, 2008. (Cited on pages 4, 37, 42, 82, 90 and 91.)

[38] F. Toschi and E. Bodenschatz, "Lagrangian properties of particles in turbulence," *Annu. Rev. Fluid Mech.*, vol. 41, pp. 375–404, 2009. (Cited on page 4.)

[39] F. De Lillo, G. Boffetta, and S. Musacchio, "Control of particle clustering in turbulence by polymer additives," *Phys. Rev. E*, vol. 85, no. 3, p. 036308, 2012. (Cited on pages 4, 83, 108 and 110.)

[40] A. Nowbahar, G. Sardina, F. Picano, and L. Brandt, "Turbophoresis attenuation in a turbulent channel flow with polymer additives," *J. Fluid Mech.*, vol. 732, pp. 706–719, Oct. 2013. (Cited on pages 4 and 110.)

[41] K. Gustavsson and B. Mehlig, "Ergodic and non-ergodic clustering of inertial particles," *Europhys. Lett.*, vol. 96, no. 6, p. 60012, 2011. (Cited on page 5.)

[42] M. Wilkinson, B. Mehlig, S. Östlund, and K. P. Duncan, "Unmixing in random flows," *Phys. Fluids*, vol. 19, no. 11, p. 113303, 2007. (Cited on page 5.)

[43] E. Afik and V. Steinberg, "On the role of initial velocities in pair dispersion in a microfluidic chaotic flow," *Nat. Commun.*, vol. 8, p. 468, 2017. (Cited on page 5.)

[44] M. Doi and S. F. Edwards, *The theory of polymer dynamics*, vol. 73. oxford university press, 1988. (Cited on page 7.)

[45] P. G. De Gennes, *Introduction to polymer dynamics*. CUP Archive, 1990. (Cited on page 7.)

[46] C. Bustamante, S. B. Smith, J. Liphardt, and D. Smith, "Single-molecule studies of dna mechanics," *Curr. Opin. Struct. Biol.*, vol. 10, no. 3, pp. 279–285, 2000. (Cited on page 8.)

[47] S. Gerashchenko, C. Chevallard, and V. Steinberg, "Single-polymer dynamics: Coil-stretch transition in a random flow," *Europhys. Lett.*, vol. 71, no. 2, p. 221, 2005. (Cited on pages 8 and 12.)

[48] P. C. Hiemenz and T. P. Lodge, *Polymer chemistry*. CRC press, 2007. (Cited on pages 9 and 10.)

[49] R. B. Bird, R. C. Armstrong, and O. Hassager, "Dynamics of polymeric liquids. vol. 1: Fluid mechanics," 1987. (Cited on pages 9, 14 and 15.)

[50] R. H. Nadolink and W. W. Haigh, "Bibliography on skin friction reduction with polymers and other boundary-layer additives," *Appl. Mech. Rev.*, vol. 48, no. 7, pp. 351–460, 1995. (Cited on page 10.)

[51] B. A. Toms, "Some observations on the flow of linear polymer solutions through straight tubes at large Reynolds numbers," *Proc. of In. Cong. On Rheology, 1948*, vol. 135, 1948. (Cited on page 10.)

[52] P. S. Virk, "Drag reduction fundamentals," *A. I. Ch. E. J.*, vol. 21, no. 4, pp. 625–656, 1975. (Cited on page 10.)

[53] K. R. Sreenivasan and C. M. White, "The onset of drag reduction by dilute polymer additives, and the maximum drag reduction asymptote," *J. Fluid Mech.*, vol. 409, pp. 149–164, 2000. (Cited on page 10.)

[54] C. M. White and M. G. Mungal, "Mechanics and prediction of turbulent drag reduction with polymer additives," *Annu. Rev. Fluid Mech.*, vol. 40, pp. 235–256, 2008. (Cited on page 10.)

[55] T. T. Perkins, S. R. Quake, D. E. Smith, and S. Chu, "Relaxation of a single dna molecule observed by optical microscopy," *Science*, vol. 264, no. 5160, pp. 822–826, 1994. (Cited on page 11.)

[56] B. H. Zimm, "Dynamics of polymer molecules in dilute solution: viscoelasticity, flow birefringence and dielectric loss," *J. Chem. Phys.*, vol. 24, no. 2, pp. 269–278, 1956. (Cited on pages 12 and 14.)

[57] E. J. Hinch, "Mechanical models of dilute polymer solutions for strong flows with large polymer deformations," *Colloques Internationaux du CNRS*, vol. 233, pp. 241–247, 1974. (Cited on page 12.)

[58] P. G. De Gennes, "Coil-stretch transition of dilute flexible polymers under ultrahigh velocity gradients," *J. Chem. Phys.*, vol. 60, no. 12, pp. 5030–5042, 1974. (Cited on page 12.)

[59] D. E. Smith, H. P. Babcock, and S. Chu, "Single-polymer dynamics in steady shear flow," *Science*, vol. 283, no. 5408, pp. 1724–1727, 1999. (Cited on page 12.)

[60] T. T. Perkins, D. E. Smith, and S. Chu, "Single polymer dynamics in an elongational flow," *Science*, vol. 276, no. 5321, pp. 2016–2021, 1997. (Cited on page 12.)

[61] M. Chertkov, "Polymer stretching by turbulence," *Phys. Rev. Lett.*, vol. 84, no. 20, p. 4761, 2000. (Cited on page 12.)

[62] E. Balkovsky, A. Fouxon, and V. Lebedev, "Turbulent dynamics of polymer solutions," *Phys. Rev. Lett.*, vol. 84, no. 20, p. 4765, 2000. (Cited on page 12.)

[63] A. Celani, S. Musacchio, and D. Vincenzi, "Polymer transport in random flow," *J. Stat. Phys.*, vol. 118, no. 3-4, pp. 531–554, 2005. (Cited on page 12.)

[64] A. Celani, A. Puliafito, and K. Turitsyn, "Polymers in linear shear flow: a numerical study," *Europhys. Lett.*, vol. 70, no. 4, p. 464, 2005. (Cited on page 12.)

[65] M. Chertkov, I. Kolokolov, V. Lebedev, and K. Turitsyn, "Polymer statistics in a random flow with mean shear," *J. Fluid Mech.*, vol. 531, pp. 251–260, 2005. (Cited on page 12.)

[66] S. Gerashchenko and V. Steinberg, "Statistics of tumbling of a single polymer molecule in shear flow," *Phys. Rev. Lett.*, vol. 96, no. 3, p. 038304, 2006. (Cited on page 12.)

[67] G. Boffetta, A. Celani, and S. Musacchio, "Two-dimensional turbulence of dilute polymer solutions," *Phys. Rev. Lett.*, vol. 91, no. 3, p. 034501, 2003. (Cited on pages 12 and 73.)

[68] S. Jin and L. R. Collins, "Dynamics of dissolved polymer chains in isotropic turbulence," *New J. Phys.*, vol. 9, no. 10, p. 360, 2007. (Cited on page 12.)

[69] D. Vincenzi, S. Jin, E. Bodenschatz, and L. R. Collins, "Stretching of polymers in isotropic turbulence: a statistical closure," *Phys. Rev. Lett.*, vol. 98, no. 2, p. 024503, 2007. (Cited on page 12.)

[70] S. R. Quake, H. Babcock, and S. Chu, "The dynamics of partially extended single molecules of dna," *Nature*, vol. 388, no. 6638, p. 151, 1997. (Cited on page 14.)

[71] E. J. Hinch, "Mechanical models of dilute polymer solutions in strong flows," *Phys. Fluids*, vol. 20, no. 10, pp. S22–S30, 1977. (Cited on page 15.)

[72] A. Peterlin, "Hydrodynamics of macromolecules in a velocity field with longitudinal gradient," *J. Polym. Sci. B*, vol. 4, no. 4, pp. 287–291, 1966. (Cited on page 17.)

[73] E. De Angelis, C. M. Casciola, R. Benzi, and R. Piva, "Homogeneous isotropic turbulence in dilute polymers," *J. Fluid Mech.*, vol. 531, pp. 1–10, 2005. (Cited on page 17.)

[74] E. De Angelis, C. M. Casciola, V. S. L'vov, R. Piva, and I. Procaccia, "Drag reduction by polymers in turbulent channel flows: Energy redistribution between invariant empirical modes," *Phys. Rev. E*, vol. 67, no. 5, p. 056312, 2003. (Cited on page 17.)

[75] K. D. Housiadas and A. N. Beris, "Direct numerical simulations of viscoelastic turbulent channel flows at high drag reduction," *Korean-Aust. J. Rheol.*, vol. 17, no. 3, pp. 131–140, 2005. (Cited on page 17.)

[76] T. Burghelea, E. Segre, and V. Steinberg, "Elastic turbulence in von karman swirling flow between two disks," *Phys. Fluids*, vol. 19, no. 5, p. 053104, 2007. (Cited on pages 18, 19 and 21.)

[77] B. A. Schiamberg, L. T. Shereda, H. Hu, and R. G. Larson, "Transitional pathway to elastic turbulence in torsional, parallel-plate flow of a polymer solution," *J. Fluid Mech.*, vol. 554, pp. 191–216, 2006. (Cited on page 19.)

[78] P. C. Sousa, F. T. Pinho, M. S. N. Oliveira, and M. A. Alves, "Purely elastic flow instabilities in microscale cross-slot devices," *Soft matter*, vol. 11, no. 45, pp. 8856–8862, 2015. (Cited on pages 21 and 22.)

[79] R. J. Poole, A. Lindner, and M. A. Alves, "Viscoelastic secondary flows in serpentine channels," *J. Non-Newtonian Fluid Mech.*, vol. 201, pp. 10–16, 2013. (Cited on page 22.)

[80] H. Bodiguel, A. Beaumont, Jand Machado, L. Martinie, H. Kellay, and A. Colin, "Flow enhancement due to elastic turbulence in channel flows of shear thinning fluids," *Phys. Rev. Lett.*, vol. 114, no. 2, p. 028302, 2015. (Cited on page 22.)

[81] D. Bonn, F. Ingremeau, Y. Amarouchene, and H. Kellay, "Large velocity fluctuations in small-Reynolds-number pipe flow of polymer solutions," *Phys. Rev. E*, vol. 84, no. 4, p. 045301, 2011. (Cited on page 22.)

[82] Y. Jun and V. Steinberg, "Elastic turbulence in a curvilinear channel flow," *Phys. Rev. E*, vol. 84, no. 5, p. 056325, 2011. (Cited on pages 22 and 68.)

[83] J. Beaumont, N. Louvet, T. Divoux, M. A. Fardin, H. Bodiguel, S. Lerouge, S. Manneville, and A. Colin, "Turbulent flows in highly elastic wormlike micelles," *Soft Matter*, vol. 9, no. 3, pp. 735–749, 2013. (Cited on page 22.)

[84] M. A. Fardin, D. Lopez, J. Croso, G. Grégoire, O. Cardoso, G. H. McKinley, and S. Lerouge, "Elastic turbulence in shear banding wormlike micelles," *Phys. Rev. Lett.*, vol. 104, no. 17, p. 178303, 2010. (Cited on page 22.)

[85] E. Balkovsky, A. Fouxon, and V. Lebedev, "Turbulence of polymer solutions," *Phys. Rev. E*, vol. 64, no. 5, p. 056301, 2001. (Cited on pages 22 and 35.)

[86] A. Fouxon and V. Lebedev, "Spectra of turbulence in dilute polymer solutions," *Phys. Fluids*, vol. 15, no. 7, pp. 2060–2072, 2003. (Cited on pages 22 and 46.)

[87] M. Chertkov, "On how a joint interaction of two innocent partners (smooth advection and linear damping) produces a strong intermittency," *Phys. Fluids*, vol. 10, no. 11, pp. 3017–3019, 1998. (Cited on page 22.)

[88] A. N. Morozov and W. van Saarloos, "An introductory essay on subcritical instabilities and the transition to turbulence in visco-elastic parallel shear flows," *Phys. Rep.*, vol. 447, no. 3-6, pp. 112–143, 2007. (Cited on pages 22 and 46.)

[89] S. Belan, A. Chernykh, and V. Lebedev, "Boundary layer of elastic turbulence," *J. Fluid Mech.*, vol. 855, pp. 910–921, 2018. (Cited on page 22.)

[90] S. Berti, A. Bistagnino, G. Boffetta, A. Celani, and S. Musacchio, "Two-dimensional elastic turbulence," *Phys. Rev. E*, vol. 77, p. 055306(R), 2008. (Cited on pages 23, 24, 25, 47, 48, 50, 57, 62, 65, 73 and 107.)

[91] E. M. Plan, A. Gupta, D. Vincenzi, and J. D. Gibbon, "Lyapunov dimension of elastic turbulence," *J. Fluid Mech.*, vol. 822, p. R4, 2017. (Cited on pages 23, 24, 25, 47 and 48.)

[92] S. Berti and G. Boffetta, "Elastic waves and transition to elastic turbulence in a two-dimensional viscoelastic kolmogorov flow," *Phys. Rev. E*, vol. 82, p. 036314, 2010. (Cited on pages 24, 47, 48, 62, 64 and 65.)

[93] H. Garg, E. Calzavarini, G. Mompean, and S. Berti, "Particle-laden two-dimensional elastic turbulence," *Eur. Phys. J. E*, vol. 41, no. 10, p. 115, 2018. (Cited on page 24.)

[94] B. Thomases, M. Shelley, and J. L. Thiffeault, "A stokesian viscoelastic flow: transition to oscillations and mixing," *Physica D*, vol. 240, no. 20, pp. 1602–1614, 2011. (Cited on pages 24 and 25.)

[95] R. van Buel, C. Schaaf, and H. Stark, "Elastic turbulence in two-dimensional taylor-couette flows," *arXiv preprint arXiv:1806.02715*, 2018. (Cited on pages 24 and 25.)

[96] H. N. Zhang, F. C. Li, Y. Cao, J. C. Yang, X. B. Li, and W. H. Cai, "The vortex structures of elastic turbulence in 3d kolmogorov flow with polymer additives," in *AIP Conference Proceedings*, vol. 1376, pp. 72–74, AIP, 2011. (Cited on page 25.)

[97] N. Liu and B. Khomami, "Elastically induced turbulence in taylor–couette flow: direct numerical simulation and mechanistic insight," *J. Fluid Mech.*, vol. 737, 2013. (Cited on page 25.)

[98] A. Gupta and R. Pandit, "Melting of a nonequilibrium vortex crystal in a fluid film with polymers: Elastic versus fluid turbulence," *Phys. Rev. E*, vol. 95, p. 033119, 2017. (Cited on page 25.)

[99] S. S. Ray and D. Vincenzi, "Elastic turbulence in a shell model of polymer solution," *Europhys. Lett.*, vol. 114, no. 4, p. 44001, 2016. (Cited on page 25.)

[100] G. Falkovich, A. Fouxon, and M. G. Stepanov, "Acceleration of rain initiation by cloud turbulence," *Nature*, vol. 419, no. 6903, p. 151, 2002. (Cited on pages 28, 82 and 90.)

[101] R. A. Shaw, "Particle-turbulence interactions in atmospheric clouds," *Annu. Rev. Fluid Mech.*, vol. 35, no. 1, pp. 183–227, 2003. (Cited on page 28.)

[102] A. Bracco, P. H. Chavanis, A. Provenzale, and E. A. Spiegel, "Particle aggregation in a turbulent keplerian flow," *Phys. Fluids*, vol. 11, no. 8, pp. 2280–2287, 1999. (Cited on page 28.)

[103] J. J. E. Williams and R. I. Crane, "Drop coagulation in cross-over pipe flows of wet steam," *J. Mech. Engng. Sci.*, vol. 21, no. 5, pp. 357–360, 1979. (Cited on page 28.)

[104] A. Karimi, S. Yazdi, and A. M. Ardekani, "Hydrodynamic mechanisms of cell and particle trapping in microfluidics," *Biomicrofluidics*, vol. 7, no. 2, p. 021501, 2013. (Cited on page 28.)

[105] G. G. Stokes, *On the effect of the internal friction of fluids on the motion of pendulums*, vol. 9. Pitt Press Cambridge, 1851. (Cited on page 30.)

[106] A. B. Basset, "On the Motion of a Sphere in a Viscous Liquid," *Philos. Trans. R. Soc. London, Ser. A*, vol. 179, pp. 43–63, 1888. (Cited on page 30.)

[107] J. Boussinesq, *Théorie analytique de la chaleur: mise en harmonie avec la thermodynamique et avec la théorie mécanique de la lumière*, vol. 2. Gauthier-Villars, 1903. (Cited on page 30.)

[108] C. W. Oseen, *About the Stokes formula, and about a related task in hydrodynamics: note 2*. Almqvist / Wiksell, 1911. (Cited on page 30.)

[109] C. M. Tchen, *Mean value and correlation problems connected with the motion of small particles suspended in a turbulent fluid*. M. Nijhoff, 1947. (Cited on page 30.)

[110] M. R. Maxey and J. J. Riley, "Equation of motion for a small rigid sphere in a nonuniform flow," *Phys. Fluids*, vol. 26, no. 4, pp. 883–889, 1983. (Cited on pages 30 and 31.)

[111] R. Gatignol, "The fax 'e n formulas for a rigid particle in an unsteady non-uniform stokes-flow," *J. Mec. Theor. Appl.*, vol. 2, pp. 143–160, 1983. (Cited on page 30.)

[112] K. D. Squires and J. K. Eaton, "Particle response and turbulence modification in isotropic turbulence," *Phys. Fluids A*, vol. 2, no. 7, pp. 1191–1203, 1990. (Cited on pages 31 and 36.)

[113] E. Balkovsky, G. Falkovich, and A. Fouxon, "Intermittent distribution of inertial particles in turbulent flows," *Phys. Rev. Lett.*, vol. 86, no. 13, p. 2790, 2001. (Cited on pages 31 and 87.)

[114] M. Cencini, J. Bec, L. Biferale, G. Boffetta, A. Celani, A. S. Lanotte, S. Musacchio, and F. Toschi, "Dynamics and statistics of heavy particles in turbulent flows," *J. Turbul.*, no. 7, p. N36, 2006. (Cited on pages 31 and 81.)

[115] J. Bec, L. Biferale, G. Boffetta, M. Cencini, S. Musacchio, and F. Toschi, "Lyapunov exponents of heavy particles in turbulence," *Phy. Fluids*, vol. 18, no. 9, p. 091702, 2006. (Cited on pages 31, 83, 87 and 108.)

[116] J. Salazar, J. De Jong, L. Cao, S. H. Woodward, H. Meng, and L. R. Collins, "Experimental and numerical investigation of inertial particle clustering in isotropic turbulence," *J. Fluid Mech.*, vol. 600, pp. 245–256, 2008. (Cited on pages 31, 32 and 35.)

[117] E. Calzavarini, T. H. Van den Berg, F. Toschi, and D. Lohse, "Quantifying microbubble clustering in turbulent flow from single-point measurements," *Phy. fluids*, vol. 20, no. 4, p. 040702, 2008. (Cited on page 31.)

[118] J. K. Eaton and J. R. Fessler, "Preferential concentration of particles by turbulence," *Int. J. Multiphase Flow*, vol. 20, pp. 169 – 209, 1994. (Cited on pages 32 and 37.)

[119] G. A. Voth, A. la Porta, A. M. Crawford, J. Alexander, and E. Bodenschatz, "Measurement of particle accelerations in fully developed turbulence," *J. Fluid Mech.*, vol. 469, pp. 121–160, 2002. (Cited on page 32.)

[120] E. W. Saw, R. A. Shaw, S. Ayyalasomayajula, P. Y. Chuang, and A. Gylfason, "Inertial clustering of particles in high-Reynolds-number turbulence," *Phys. Rev. Lett.*, vol. 100, p. 214501, May 2008. (Cited on pages 32 and 35.)

[121] I. J. Benczik, Z. Toroczkai, and T. Tel, "Selective sensitivity of open chaotic flows on inertial tracer advection: Catching particles with a stick," *Phys. Rev. Lett.*, vol. 89, no. 16, p. 164501, 2002. (Cited on page 33.)

[122] H. Yoshimoto and S. Goto, "Self-similar clustering of inertial particles in homogeneous turbulence," *J. Fluid Mech.*, vol. 577, pp. 275–286, 2007. (Cited on pages 33 and 37.)

[123] B. Mehlig and M. Wilkinson, "Coagulation by random velocity fields as a kramers problem," *Phys. Rev. Lett.*, vol. 92, p. 250602, Jun 2004. (Cited on page 35.)

[124] B. Mehlig, M. Wilkinson, K. Duncan, T. Weber, and M. Ljunggren, "Aggregation of inertial particles in random flows," *Phys. Rev. E*, vol. 72, p. 051104, Nov 2005. (Cited on page 35.)

[125] J. Bec, L. Biferale, M. Cencini, A. Lanotte, S. Musacchio, and F. Toschi, "Heavy particle concentration in turbulence at dissipative and inertial scales," *Phys. Rev. Lett.*, vol. 98, p. 084502, Feb 2007. (Cited on pages 35, 37, 39, 40, 41 and 81.)

[126] S. J. S., A. U. K., and J. S. S., "On the quantification of preferential accumulation," *Int. J. Heat Fluid Flow*, vol. 30, no. 4, pp. 789 – 795, 2009. (Cited on page 35.)

[127] M. R. Maxey, "The gravitational settling of aerosol particles in homogeneous turbulence and random flow fields," *J. Fluid Mech.*, vol. 174, pp. 441–465, 1987. (Cited on page 35.)

[128] A. Okubo, "Horizontal dispersion of floatable particles in the vicinity of velocity singularities such as convergences," *Deep-Sea Res.*, vol. 17, pp. 445–454, 1970. (Cited on pages 36 and 78.)

[129] J. Weiss, "The dynamics of enstrophy transfer in two-dimensional hydrodynamics," *Physica D*, vol. 48, no. 2-3, pp. 273–294, 1991. (Cited on pages 36 and 78.)

[130] A. Gupta and R. Pandit, "Melting of a nonequilibrium vortex crystal in a fluid film with polymers: Elastic versus fluid turbulence," *Phys. Rev. E*, vol. 95, no. 3, p. 033119, 2017. (Cited on pages 37, 76 and 78.)

[131] R. Monchaux, M. Bourgoin, and A. Cartellier, "Analyzing preferential concentration and clustering of inertial particles in turbulence," *Int. J. Multiphase Flow*, vol. 40, pp. 1 – 18, 2012. (Cited on pages 38 and 39.)

[132] R. Monchaux, M. Bourgoin, and A. Cartellier, "Preferential concentration of heavy particles: a voronoï analysis," *Phys. Fluids*, vol. 22, no. 10, p. 103304, 2010. (Cited on pages 38 and 39.)

[133] L. Chen, S. Goto, and J. C. Vassilicos, "Turbulent clustering of stagnation points and inertial particles," *J. Fluid Mech.*, vol. 553, pp. 143–154, 2006. (Cited on page 37.)

[134] S. W. Coleman and J. C. Vassilicos, "A unified sweep-stick mechanism to explain particle clustering in two- and three-dimensional homogeneous, isotropic turbulence," *Phys. Fluids*, vol. 21, no. 11, p. 113301, 2009. (Cited on page 37.)

[135] L. P. Wang and M. R. Maxey, "Settling velocity and concentration distribution of heavy particles in homogeneous isotropic turbulence," *J. Fluid Mech.*, vol. 256, pp. 27–68, 1993. (Cited on page 37.)

[136] J. Bec, L. Biferale, M. Cencini, A. S. Lanotte, and F. Toschi, "Intermittency in the velocity distribution of heavy particles in turbulence," *J. Fluid Mech.*, vol. 646, pp. 527–536, 2010. (Cited on page 37.)

[137] A. Aliseda, A. Cartellier, F. Hainaux, and J. C. Lasheras, "Effect of preferential concentration on the settling velocity of heavy particles in homogeneous isotropic turbulence," *J. Fluid Mech.*, vol. 468, pp. 77–105, 2002. (Cited on page 39.)

[138] P. Grassberger and I. Procaccia, "Characterization of strange attractors," *Phys. Rev. Lett.*, vol. 50, pp. 346–349, Jan 1983. (Cited on pages 39, 82 and 88.)

[139] V. Angelo, C. Fabio, and C. Massimo, *Chaos: From Simple Models To Complex Systems*, vol. 17. World Scientific, 2009. (Cited on pages 39 and 41.)

[140] L. F. Y. C. T. J. N. T. R. Tang, F. Wen, Y. Yang, C. T. Crowe, J. N. Chung, and T. R. Troutt, "Self-organizing particle dispersion mechanism in a plane wake," *Phys. Fluids A*, vol. 4, no. 10, pp. 2244–2251, 1992. (Cited on page 39.)

[141] J. R. Fessler, J. D. Kulick, and J. K. Eaton, "Preferential concentration of heavy particles in a turbulent channel flow," *Phys. Fluids*, vol. 6, no. 11, pp. 3742–3749, 1994. (Cited on page 39.)

[142] J. Bec, M. Cencini, R. Hillerbrand, and K. Turitsyn, "Stochastic suspensions of heavy particles," *Physica D*, vol. 237, no. 14-17, pp. 2037–2050, 2008. (Cited on page 39.)

[143] B. B. Mandelbrot, *The fractal geometry of nature*, vol. 173. WH freeman New York, 1983. (Cited on page 41.)

[144] H. O. Peitgen, H. Jürgens, and D. Saupe, "Chaos and fractals. new frontiers in science," 1991. (Cited on page 41.)

[145] J. L. Kaplan and J. A. Yorke, "Chaotic behavior of multidimensional difference equations," in *Functional Differential equations and approximation of fixed points*, pp. 204–227, Springer, 1979. (Cited on pages 41 and 87.)

[146] J. D. Farmer, E. Ott, and J. A. Yorke, "The dimension of chaotic attractors," *Physica D*, vol. 7, no. 1-3, pp. 153–180, 1983. (Cited on pages 41 and 87.)

[147] A. Crisanti, G. Paladin, and A. Vulpiani, *Products of Random Matrices: in Statistical Physics*, vol. 104. Springer Science & Business Media, 2012. (Cited on pages 41, 86 and 87.)

[148] I. Fouxon, L. Schmidt, P. Ditlevsen, M. van Reeuwijk, and M. Holzner, "Inhomogeneous growth of fluctuations of concentration of inertial particles in channel turbulence," *Phys. Rev. Fluids*, vol. 3, no. 6, p. 064301, 2018. (Cited on pages 42, 43 and 44.)

[149] G. Sardina, F. Picano, P. Schlatter, L. Brandt, and C. M. Casciola, "Large scale accumulation patterns of inertial particles in wall-bounded turbulent flow," *Flow, turbulence and combustion*, vol. 86, no. 3-4, pp. 519–532, 2011. (Cited on page 43.)

[150] S. Balachandar and J. K. Eaton, "Turbulent dispersed multiphase flow," *Annu. Rev. Fluid Mech.*, vol. 42, pp. 111–133, 2010. (Cited on page 43.)

[151] M. Caporaloni, F. Tampieri, F. Trombetti, and O. Vittori, "Transfer of particles in nonisotropic air turbulence," *J. Atmospheric Sci.*, vol. 32, no. 3, pp. 565–568, 1975. (Cited on pages 43, 44, 95, 99, 102, 103 and 108.)

[152] M. W. Reeks, "The transport of discrete particles in inhomogeneous turbulence," *J. Aerosol Sci.*, vol. 14, no. 6, pp. 729–739, 1983. (Cited on page 43.)

[153] A. Guha, "A unified eulerian theory of turbulent deposition to smooth and rough surfaces," *J. Aerosol Sci.*, vol. 28, pp. 1517–1537, 1997. (Cited on pages 43 and 102.)

[154] J. O. Hinze, *Turbulence: An Introduction to Its Mechanism and Theory*. McGraw-Hill series in mechanical engineering, McGraw-Hill, 1959. (Cited on page 43.)

[155] A. Soldati and C. Marchioli, "Physics and modelling of turbulent particle deposition and entrainment: Review of a systematic study," *Int. J. Multiphase Flow*, vol. 35, no. 9, pp. 827–839, 2009. (Cited on page 43.)

[156] J. W. Brooke, K. Kontomaris, T. Hanratty, and J. B. McLaughlin, "Turbulent deposition and trapping of aerosols at a wall," *Phys. Fluids A*, vol. 4, pp. 825–834, 1992. (Cited on pages 44 and 95.)

[157] J. Young and A. Leeming, "A theory of particle deposition in turbulent pipe flow," *J. Fluid Mech.*, vol. 340, pp. 129–159, 1997. (Cited on page 44.)

[158] R. G. Larson, "Instabilities in viscoelastic flows," *Rheol. Acta*, vol. 31, no. 3, pp. 213–263, 1992. (Cited on page 45.)

[159] A. Groisman and V. Steinberg, "Couette-taylor flow in a dilute polymer solution," *Phys. Rev. Lett.*, vol. 77, no. 8, p. 1480, 1996. (Cited on page 45.)

[160] R. G. Larson, E. S. G. Shaqfeh, and S. J. Muller, "A purely elastic instability in taylor–couette flow," *J. Fluid Mech.*, vol. 218, pp. 573–600, 1990. (Cited on page 45.)

[161] G. Boffetta, A. Celani, A. Mazzino, A. Puliafito, and M. Vergassola, "The viscoelastic kolmogorov flow: eddy viscosity and linear stability," *J. Fluid Mech.*, vol. 523, pp. 161–170, 2005. (Cited on pages 45, 47, 48 and 49.)

[162] Y. Jun and V. Steinberg, "Mixing of passive tracers in the decay batchelor regime of a channel flow," *Phys. Fluids*, vol. 22, no. 12, p. 123101, 2010. (Cited on page 46.)

[163] A. N. Morozov and W. van Saarloos, "Subcritical finite-amplitude solutions for plane couette flow of viscoelastic fluids," *Phys. Rev. Lett.*, vol. 95, no. 2, p. 024501, 2005. (Cited on page 46.)

[164] V. I. Arnold and L. D. Meshalkin, "An kolmogorov's seminar on selected problems of analysis (1958/1959)," *Uspekhi Mat. Nauk*, vol. 15, no. 1, pp. 247–250, 1960. (Cited on pages 46 and 47.)

[165] A. M. Obukhov, "Kolmogorov flow and laboratory simulation of it," *Russian Math. Surveys*, vol. 38, no. 4, pp. 113–126, 1983. (Cited on page 47.)

[166] L. D. Meshalkin, "Investigation of the stability of a stationary solution of a system of equations for the plane movement of an incompressible viscous liquid," *J. Appl. Math. Mech.*, vol. 25, pp. 1700–1705, 1962. (Cited on pages 47 and 48.)

[167] R. Sureshkumar and A. N. Beris, "Effect of artificial stress diffusivity on the stability of numerical calculations and the flow dynamics of time-dependent viscoelastic flows," *J. Non-Newtonian Fluid Mech.*, vol. 60, no. 1, pp. 53–80, 1995. (Cited on pages 49 and 51.)

[168] T. Vaithianathan and L. R. Collins, "Numerical approach to simulating turbulent flow of a viscoelastic polymer solution," *J. Comput. Phys.*, vol. 187, no. 1, pp. 1–21, 2003. (Cited on page 50.)

[169] A. N. Beris and R. Sureshkumar, "Simulation of time-dependent viscoelastic channel poiseuille flow at high Reynolds numbers," *Chem. Eng. Sci.*, vol. 51, no. 9, pp. 1451–1471, 1996. (Cited on page 51.)

[170] A. N. Beris and C. D. Dimitropoulos, "Pseudospectral simulation of turbulent viscoelastic channel flow," *Comput. Methods in Appl. Mech. Eng.*, vol. 180, no. 3-4, pp. 365–392, 1999. (Cited on page 51.)

[171] S. Berti and G. Boffetta, "Elastic waves and transition to elastic turbulence in a two-dimensional viscoelastic kolmogorov flow," *Phys. Rev. E*, vol. 82, no. 3, p. 036314, 2010. (Cited on pages 52, 77 and 78.)

[172] A. Gupta and D. Vincenzi, "Effect of polymer-stress diffusion in the numerical simulation of elastic turbulence," *ArXiv e-prints*, Sept. 2018. (Cited on pages 53 and 57.)

[173] A. Fouxon and V. Lebedev, "Spectra of turbulence in dilute polymer solutions," *Phys. Fluids*, vol. 15, no. 7, pp. 2060–2072, 2003. (Cited on page 65.)

[174] E. De Angelis, C. M. Casciola, and R. Piva, "Energy spectra in viscoelastic turbulence," *Physica D*, vol. 241, pp. 297–303, 2012. (Cited on page 65.)

[175] M. Q. Nguyen, A. Delache, S. Simoëns, W. J. T. Bos, and M. El Hajem, "Small scale dynamics of isotropic viscoelastic turbulence," *Phys. Rev. Fluids*, vol. 1, p. 083301, 2016. (Cited on page 65.)

[176] Y. Jun and V. Steinberg, "Polymer concentration and properties of elastic turbulence in a von karman swirling flow," *Phys. Rev. Fluids*, vol. 2, p. 103301, 2017. (Cited on pages 65 and 68.)

[177] P. E. Arratia, G. A. Voth, and J. P. Gollub, "Stretching and mixing of non-newtonian fluids in time-periodic flows," *Phys. Fluids*, vol. 17, no. 5, p. 053102, 2005. (Cited on page 69.)

[178] G. Paladin and A. Vulpiani, "Anomalous scaling laws in multifractal objects," *Phys. Rep.*, vol. 156, no. 4, pp. 147–225, 1987. (Cited on page 69.)

[179] G. Boffetta, M. Cencini, M. Falcioni, and A. Vulpiani, "Predictability: a way to characterize complexity," *Phys. Rep.*, vol. 356, no. 6, pp. 367–474, 2002. (Cited on page 69.)

[180] K. Gustavsson and B. Mehlig, "Statistical models for spatial patterns of heavy particles in turbulence," *Adv. Phys.*, vol. 65, no. 1, pp. 1–57, 2016. (Cited on page 82.)

[181] J. Bec, "Multifractal concentrations of inertial particles in smooth random flows," *J. Fluid Mech.*, vol. 528, pp. 255–277, 2005. (Cited on pages 82, 83, 88 and 108.)

[182] G. Benettin, L. Galgani, A. Giorgilli, and J. M. Strelcyn, "Lyapunov characteristic exponents for smooth dynamical systems and for hamiltonian systems; a method for computing all of them. part 1: Theory," *Meccanica*, vol. 15, no. 1, pp. 9–20, 1980. (Cited on page 86.)

[183] E. Calzavarini, M. Kerscher, D. Lohse, and F. Toschi, "Dimensionality and morphology of particle and bubble clusters in turbulent flow," *J. Fluid Mech.*, vol. 607, pp. 13–24, 2008. (Cited on page 87.)

[184] E. Ott, *Chaos in dynamical systems*. Cambridge university press, 2002. (Cited on page 88.)

[185] L. Y. Yeo, H. C. Chang, P. P. Y. Chan, and J. R. Friend, "Microfluidic devices for bioapplications," *Small*, vol. 7, no. 1, pp. 12–48, 2011. (Cited on page 89.)

[186] M. A. M. Ali, K. K. Ostrikov, F. A. Khalid, B. Y. Majlis, and A. A. Kayani, "Active bioparticle manipulation in microfluidic systems," *RSC Adv.*, vol. 6, no. 114, pp. 113066–113094, 2016. (Cited on page 89.)

[187] X. B. Li, F. C. Li, W. H. Cai, H. N. Zhang, and J. C. Yang, "Very-low-re chaotic motions of viscoelastic fluid and its unique applications in microfluidic devices: a review," *Exp. Therm. Fluid Sci.*, vol. 39, pp. 1–16, 2012. (Cited on page 89.)

[188] Y. Zhou, A. S. Wexler, and L. P. Wang, "Modelling turbulent collision of bidisperse inertial particles," *J. Fluid Mech.*, vol. 433, pp. 77–104, 2001. (Cited on page 90.)

[189] A. N. Kolmogorov, "On the approximation of distributions of sums of independent summands by infinitely divisible distributions," *Sankhya: Indian J. Stat. A*, pp. 159–174, 1963. (Cited on page 90.)

[190] S. Duhr and D. Braun, "Why molecules move along a temperature gradient," *Proc. Natl. Acad. Sci. U.S.A.*, vol. 103, no. 52, pp. 19678–19682, 2006. (Cited on page 95.)

[191] S. Duhr and D. Braun, "Thermophoretic depletion follows boltzmann distribution," *Phys. Rev. Lett.*, vol. 96, no. 16, p. 168301, 2006. (Cited on page 95.)

[192] S. R. De Groot and P. Mazur, *Non-equilibrium thermodynamics*. Courier Corporation, 2013. (Cited on page 95.)

[193] J. C. Maxwell, "Vii. on stresses in rarified gases arising from inequalities of temperature," *Philos. Trans. R. Soc. London*, vol. 170, pp. 231–256, 1879. (Cited on page 95.)

[194] S. Belan, I. Fouxon, and G. Falkovich, "Localization-delocalization transitions in turbophoresis of inertial particles," *Phys. Rev. Lett.*, vol. 112, p. 234502, Jun 2014. (Cited on pages 99, 103 and 108.)

[195] J. O. Hinze, *Turbulence : an introduction to its mechanism and theory*. McGraw-Hill, New York, 1959. (Cited on page 103.)

[196] Y. Liu and V. Steinberg, "Molecular sensor of elastic stress in a random flow," *Europhys. Lett.*, vol. 90, p. 44002, 2010. (Cited on page 110.)